NUMERICAL MODELING OF GAS MIGRATION INTO AND THROUGH FAULTED SAND RESERVOIRS IN PABST FIELD (MAIN PASS EAST BLOCK 259), NORTHERN GULF OF MEXICO

A Dissertation

by

YUQIAN LI

Submitted to the Office of Graduate Studies of
Texas A&M University
in partial fulfillment of the requirements for the degree of

DOCTOR OF PHILOSOPHY

May 2006

Major Subject: Geophysics

NUMERICAL MODELING OF GAS MIGRATION INTO AND THROUGH FAULTED SAND RESERVOIRS IN PABST FIELD (MAIN PASS EAST BLOCK 259), NORTHERN GULF OF MEXICO

A Dissertation

by

YUQIAN LI

Submitted to the Office of Graduate Studies of
Texas A&M University
in partial fulfillment of the requirements for the degree of

DOCTOR OF PHILOSOPHY

Approved by:

Chair of Committee,	Richard L. Carlson
Committee Members,	Joel S. Watkins
	Brann Johnson
	Steven L. Dorobek
	Luc T. Ikelle
	William D. McCain, Jr.
Head of Department,	Richard L. Carlson

May 2006

Major Subject: Geophysics

ABSTRACT

Numerical Modeling of Gas Migration into and through

Faulted Sand Reservoirs in Pabst Field

(Main Pass East Block 259), Northern Gulf of Mexico. (May 2006)

Yuqian Li, B.S., Nanjing University

Chair of Committee: Dr. Richard Carlson

The further exploration and development of Pabst Gas Field with faulted sand reservoirs require an understanding of the properties and roles of faults, particularly Low Throw near Vertical Faults (LTNVFs), in gas migration and accumulation at a reservoir scale. This study presents numerical modeling of gas migration and accumulation processes in Pabst Field. Based on studies of the reservoirs, structure, faults, and fluid properties of the field, reservoir scale modeling was performed to determine the gas supply style and the fault properties by means of hundreds of iterations in which the fault properties and gas supply pattern were modified to match the gas distribution obtained from modeling with the gas distribution inferred from seismic data constrained by well data and production data.

This study finds that in the main three sand reservoirs of Pabst Field the overlying younger sands cut down into the underlying older sands, so that partial connections between the three sands allow gas communication among the sands. Meanwhile, three fault families break up the three sands into numerous compartments. A primary fault and large synthetic and antithetic faults act as gas migration pathways: the synthetic and

antithetic faults are inlets for gas flow and the primary fault is an outlet, and LTNVFs act as barriers to gas flow.

Modeling requires fault properties in the field to change while the field is formed. The porosity and permeability of the faults in Pabst Field are 10% and 0.1 md, respectively, during gas charging of the sand reservoirs. But when there is no gas charging and large gas columns are maintained, the porosity and permeability of the faults decrease to 6% and 0.001 md, respectively. Pabst Field probably has an impulse gas charge history. Fault opening and closing, gas charge and recharge, and replacement of gas by formation water may occur. A combination of stratigraphy, structure, overpressure and gas charge rate control gas migration style, gas charge history, and gas distribution in the field.

The significance of the study is that this improved numerical approach for modeling gas migration into and through specifically faulted sand reservoirs fills the gap between basin modeling and production modeling.

DEDICATION

To My Family

ACKNOWLEDGEMENTS

I am a nontraditional student at Texas A&M University. Before I began pursuing a Ph.D. in Geophysics, I had worked for China National Offshore Oil Corporation for 16 years. It was Dr. Joel Watkins, the first chair of my advisory committee, who gave me the opportunity to continue my studies, to experience several years of Aggie life, and to study numerical simulation of a real gas field: part of the project of the Integrated Reservoir Investigations Group (IRIG). This study was conducted under his instruction and mentorship, from data preparation, goal design, proposal, and experiment to writing and mapping. Without him, I could not have written this dissertation. I would like to thank Dr. Watkins for his foresight and wisdom. It was Dr. Richard Carlson, my second chair of my advisory committee, who instructed me to complete this dissertation. I would like to thank Dr. Carlson for his patience and encouragement. Without him, I could not finish my study. I also would like to thank to my committee members: Dr. Brann Johnson, Dr. Luc Ikelle, Dr. Steven Dorobek, and Dr. William McCain for their sincerity and rigorous scholarship. They gave me not only instruction for the study but also unforgettable lectures. I also would like to thank Dr. Carrie Decker, a researcher of IRIG, and Dr. Berg for their valuable help and enlightenment in the study.

I would like to thank the staff of Texas A&M's Department of Petroleum Engineering, whom I have bothered numerous times for Eclipse® computer runs, for their patience and guidance. I acknowledge Dr. Jianyong Bai, Dr. Tao Wu, Dr. Dongmin Sun, and all the other Chinese graduate students in Department of Geology

and Geophysics for their generous help. I also thank my parents and my family for their support and encouragement.

TABLE OF CONTENTS

CHAPTER Page

LIST OF FIGURES

FIGURE Page

FIGURE Page

FIGURE Page

LIST OF TABLES

TABLE Page

CHAPTER I

INTRODUCTION

Pabst Field is primarily a gas field located on the outer continental shelf, near the Miocene paleo-shelf edge, in Main Pass East 259, northern Gulf of Mexico (Figure 1). Its main reservoirs are three sands with depths ranging from 9,000 ft to 11,000 ft. The structure of the field is a rollover anticline in the hanging wall of a northwest-trending normal fault. Three fault families, consisting of northwest-trending synthetic and antithetic faults and north-trending accommodation or cross faults, complicate the structure. Stratigraphically, younger slope fan channel sands were deposited on underlying older sands and locally cut down into the older sands, which results in intersand communication for fluid flow. The faults and stratigraphy produce a number of complex reservoir compartments. This type of structure is common in the northern Gulf of Mexico (Bradshaw and Watkins, 1996; Rowan et al., 1999).

PROBLEM AND OBJECTIVES

There are few published studies of hydrocarbon migration in faulted reservoirs. It is difficult to describe specific processes of hydrocarbon accumulation in a given compartment using conventional and semi-quantitative approaches (Smith, 1966), because hydrocarbon distribution is determined by many geological factors, including hydrocarbon supply, fluid pressure distribution, reservoir properties, and fault properties.

This dissertation follows the style of AAPG Bulletin.

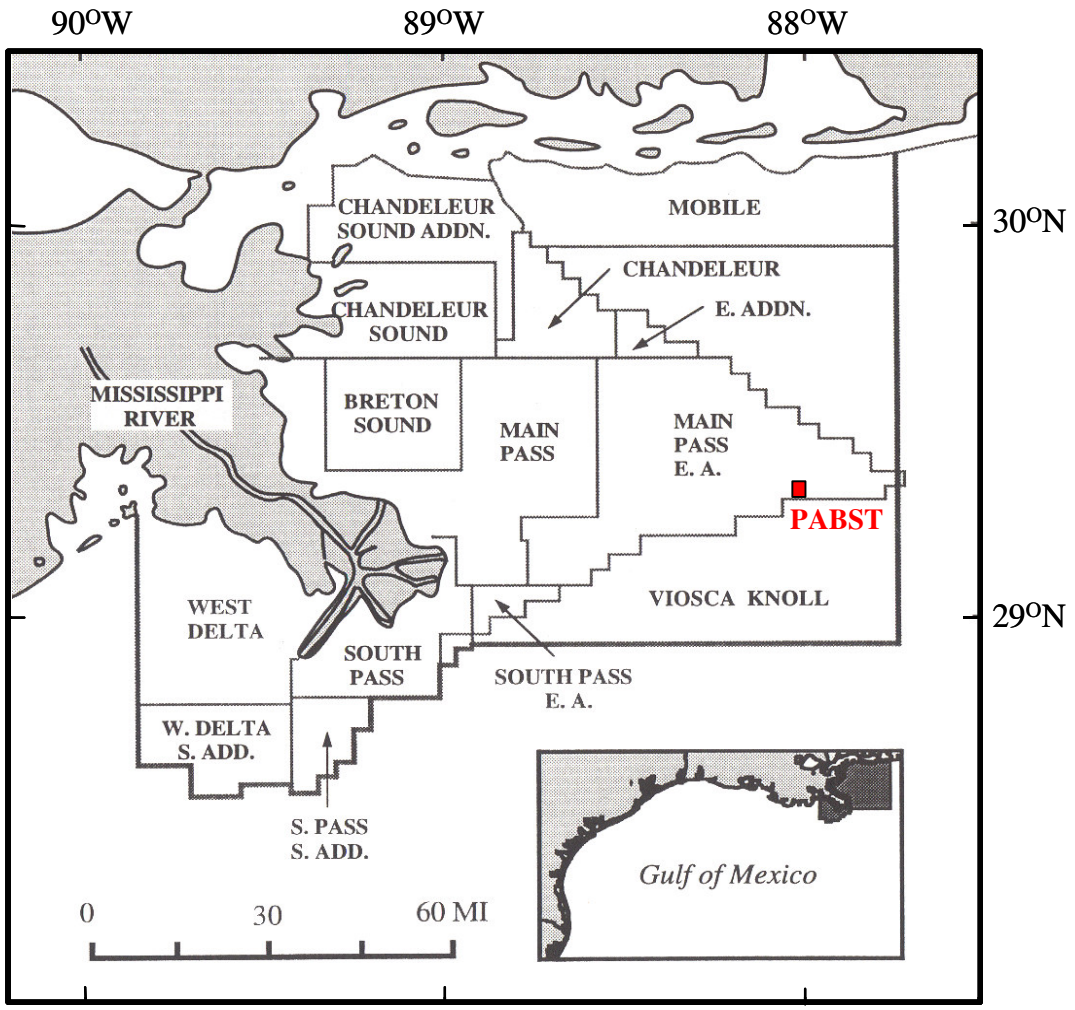

Figure 1. Location of Pabst Field. The field is located at 259 block of Main Pass East Area, northern Gulf of Mexico.

Previous studies indicate that the geochemical characteristics of the hydrocarbons in Pabst Field vary between some compartments (Sassen et al., 2001). Production data also reveal that some faults form barriers to fluid flow (Watkins et al., 1999b). A study integrating multiple disciplines such as geophysics, geology, geochemistry, and petroleum engineering is necessary for understanding hydrocarbon migration and

accumulation in the field. Pabst Field is suitable for this study primarily because it has had a very short hydrocarbon charging duration (Sassen et al., 2001), and consists of multiple, faulted sand reservoirs. Furthermore, the field is well characterized from a geological and engineering perspective, which provides essential data needed for modeling. It is a challenge to investigate such a complex field in order to understand its hydrocarbon charging process. Numerical modeling is an effective approach because it simulates not only the hydrocarbon distribution but also the dynamic processes of hydrocarbon migration into, through, and out of the sand reservoirs. The results of modeling are a synthesis of the multidisciplinary studies.

Hydrocarbon migration modeling at the basin scale has been very widely applied (Lerche, 1990; Hindle, 1997). Numerical modeling for a field on a production time scale is also a common approach in the petroleum industry (Ottesen et al., 1998; Knai and Knipe, 1998). These two types of modeling, however, have not been applied to modeling hydrocarbon migration in multiply faulted compartments. Basin scale modeling does not describe a single compartment in adequate detail; production modeling addresses extraction of in-place hydrocarbons, but not the process of hydrocarbon migration and accumulation.

A common weakness of the basin and production simulation approaches is that they consider faults to be single planes as opposed to zones with distinct petrophysical properties. One such property, capillary displacement pressure, is important because it determines the trapping capacity of the fault. By acting as both impediments and conduits to migration, faults control the flow of hydrocarbons into and across reservoirs.

In this case, the faults are a key factor in our understanding of hydrocarbon accumulation, further exploration, and development of Pabst Field.

Direct measurement of the petrophysical properties of faults is difficult because of the lack of the core data and dip-meter log data across faults. The interpretation of the faults of Pabst Field is based mainly on seismic attributes, such as coherency and dip. Numerical simulation modeling as used here is also an iterative process, which entails "trial-and-error" changes of model parameters, such as hydrocarbon supply pattern and rate as well as fault properties. If the hydrocarbon distribution is known, simulation may verify geometry, position, and properties of faults based on matching the hydrocarbon distribution obtained from simulation with that observed in the field.

To improve our understanding of Pabst Field and similar faulted reservoirs, modeling at reservoir scale is necessary. In view of the fact that Pabst Field is primarily a gas field, this study assumes the field is a pure dry gas field. Therefore, this reservoir- scale model assumes two-phase fluid flow (water and gas).

The objectives in this study are 1) to investigate gas migration pathways and rates by using reservoir-scale modeling; 2) to test and verify fault patterns inferred from seismic data and deduce fault properties through simulating gas migration and accumulation in Pabst Field by matching numerical results with the gas distribution inferred from seismic, well log, and geochemical data. The significance of this approach is that a simulation of hydrocarbon migration in faulted reservoirs fills the gap between basin modeling and production modeling and helps one to understand fault sealing and

leakage. In addition, the simulation helps to predict the gas potential of undrilled compartments in the field.

DATA AND TOOLS

The data for this study include 3-D post-stack time migrated seismic data and wire-line log data from 19 wells (Figure 2). The seismic survey covers Pabst Field and the adjacent region, an area of about 81 square miles, with 4 ms sampling, and a 26 Hz dominant frequency. The time depth of the main reservoirs ranges from 2.7 to 3.2 seconds in two-way traveltime. The well log data include gamma ray (GR, unit: GAPI), spontaneous potential (SP, unit: mv), resistivity (R_t, unit: OHMM), and sonic (AC, unit: μs/ft) logs.

A Sun Unix-based workstation with GeoQuest IESX software was used to interpret structure, reservoir geometry, and fault geometry. Seismic attributes and well data were integrated to interpret the gas distribution. Interpretation of these data provided the geometries of reservoirs and faults for the numerical simulation. Geochemical data, production data, and the fluid and rock properties also are needed for modeling purposes. The Integrated Reservoir Investigation Group (IRIG) has conducted research in this area, and its results are referenced (Watkins et al., 1999a, 2000, 2001b; Bai, 2003).

Applicability and adaptability are two important factors in selecting a numerical reservoir simulator. A commercial model, Eclipse® 100, which is a black oil simulator developed by Schlumberger (Schlumberger, 1982-1999), was chosen for this study. This simulator is extensively used in modeling and research. For example, Kortekaas

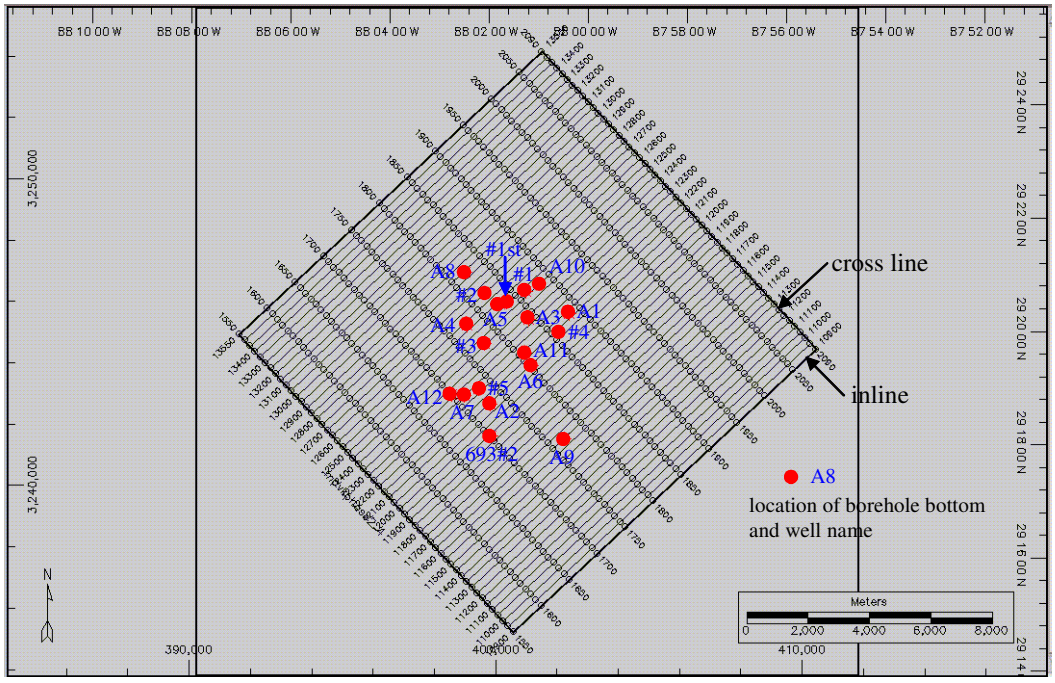

Figure 2. Seismic grid and well locations in study area.

(1985) employed it to simulate oil-water displacement in cross-bedded reservoirs. England and Townsend (1998) used Eclipse® 100 to study the effect of faults on oil-water displacement. However, they dealt with the faults as single planes instead of zones. Bai (2003) used Eclipse® 100 to investigate the nature of hydrocarbon migration and entrapment in faulted reservoirs by means of simple geometry models. The use of Eclipse® 100 to simulate gas migration in and through a faulted reservoir in a given field is a new endeavor.

PROCEDURE

Geology of Pabst Field

Seismic interpretation provides a number of parameters, such as reservoir geometry and burial depth, and fault geometry that the simulator requires. This interpretation includes structure, reservoir, fault, and gas distribution obtained by means of seismic amplitude anomalies. Structure maps, thickness maps of reservoirs, and gas distribution maps were obtained from the interpretation.

Construction of geological models and numerical models

A geological model reflects gas migration pathways, gas charge rate, charge time, and duration of gas supply. Geological models were constructed by integrating results from a study of the geology of Pabst Field. Based on the geological model, I calculated parameters of reservoir petrophysical properties and fault petrophysical properties, as well as fluid properties to construct numerical models. Most formulas and some data are taken from the literature and previous studies by IRIG (Watkins et al., 1999a, 2000, 2001b). Parameters for the modeling are listed in Chapter III.

Simulation of field modeling

In the Eclipse ® model, the geologic structure is divided into cells, and petrophysical properties are assigned to each cell. In the models, sands, shales, and faults are initially saturated with formation water. Dry gas is input through the charge faults to simulate

gas supply. An Eclipse® run produces gas/water saturations, pressure, and flow rate, in each cell at each time step, providing a dynamic model of fluid flow in reservoirs and fault zones. This numerical modeling needs fault architecture, a porosity and permeability model, capillary pressure, and a relative permeability model. A number of numerical models with simple geometries were used to test the effect of gas charge rate, fault thickness, and capillary properties on gas/water saturation. Then more complex models which represent Pabst Field were used to simulate its gas charging process.

Examination of field modeling

Modeling is an iteration process in which pressure and gas distribution of Pabst Field produced by the simulation are compared with the pressure and gas distribution interpreted from seismic data and constrained by well data. Model parameters, such as mainly gas supply style and fault properties, are then adjusted from one modeling run to another, and the process is repeated until a satisfactory match is achieved.

CHAPTER II

PABST FIELD PETROLEUM GEOLOGY

REGIONAL GEOLOGICAL BACKGROUND

Geographically, Pabst Field belongs to the Mississippi Delta Margin region (Figure 3). Like other regions in the Gulf of Mexico, this area underwent a Paleozoic pre-rift phase, a Triassic-Jurassic syn-rift and sea floor spreading phase and the post-rift subsidence since the Cretaceous.

During the Late Triassic, the North American Plate began to crack and drift from African and South American Plates. Rifting in the Gulf of Mexico basin began and continued through Late Triassic, Early and Middle Jurassic, producing non-marine clastic and volcanic rocks that overlie the basement of Paleozoic metamorphic, clastic and intrusive rocks. In the Late Jurassic, rifting led to sea floor spreading and the deposition of carbonate and clastic rocks. Intermittent advance of seawater into the Gulf of Mexico basin from the west resulted in the formation of extensive salt deposits known as the Louann Salt, which greatly has influenced the features of sediments and structures in the basin. During the Cretaceous, the basin entered into a post-rift stage of development. Cooling and subsidence coupled with rising sea level increased the size of the basin to its maximum extent. Deep marine carbonate consisting of chalk and marl were built, and became the main source rocks in the Gulf of Mexico basin. During the Cenozoic, a thick prograding clastic wedge developed along the northwestern and northern margin of the basin (Allen and Allen, 1990).

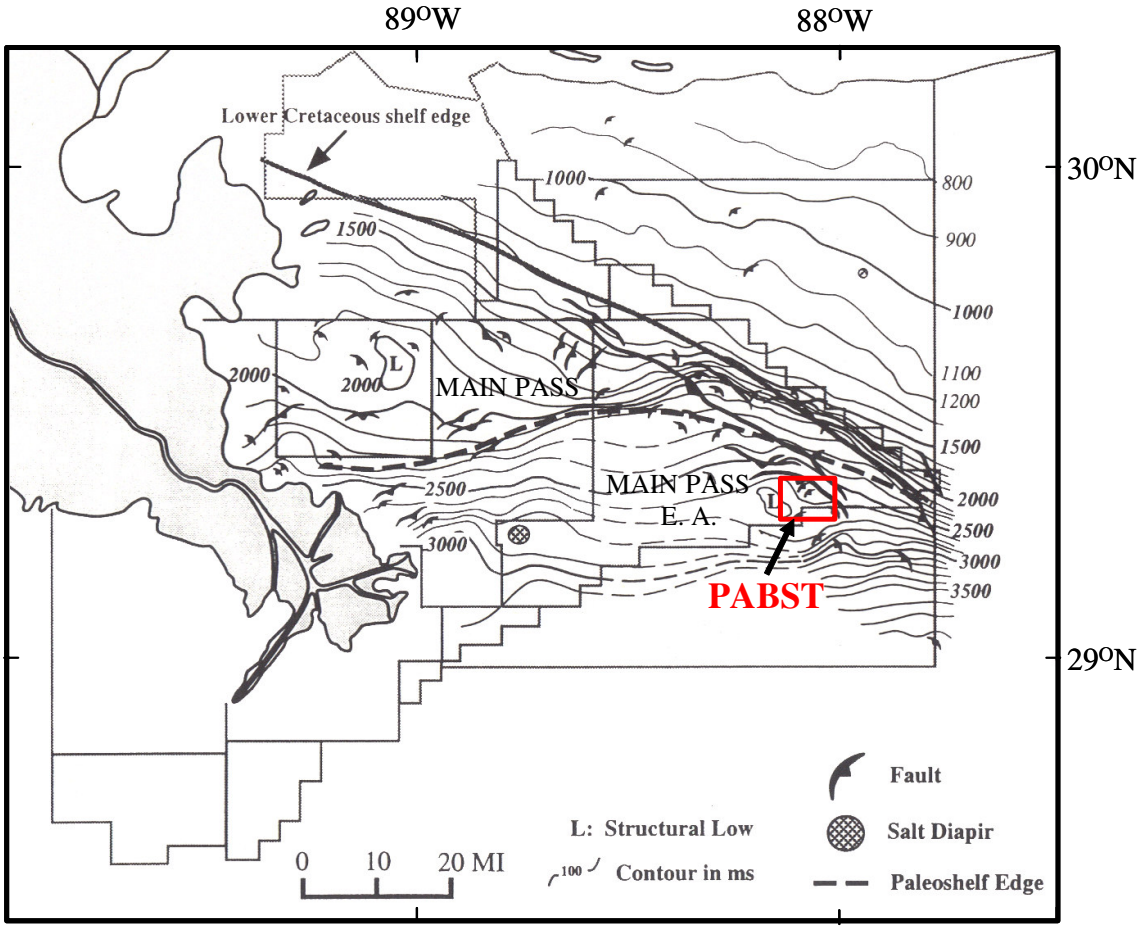

Figure 3. Regional geological background of the Mississippi Delta Margin region at Late Miocene time. The location of Pabst Field is near the edge of the paleo-shelf (modified from Sunwoo, 1999).

From the Late Cretaceous through the Early Tertiary, this region was starved of sediments, resulting in thin Upper Cretaceous and Lower Tertiary carbonate and clastic deposits. In contrast to this period of slow deposition, rapid progradation of the Mississippi Delta sands and shale produced very thick Miocene units, because in the

Early Miocene, the Mississippi river migrated from south-eastern Texas to south-eastern Louisiana (Galloway, 1989; Galloway et al., 2000). The sedimentation rate in the Main Pass area increased from 23 ft/my in the Oligocene to 121 ft/my in the Middle Miocene (Sunwoo, 1999).

Located on the outer continental slope, the Middle and Lower Miocene reservoirs in Pabst Field have two structural characteristics that affect hydrocarbon accumulation: first, the small overburden load due to the lower sedimentation rate in pre-Miocene reduced the development of salt structures. Salt bodies in this area are few and small (Sunwoo, 1999). Secondly, there has been long-term fault growth in this area because the shelf break is at a relatively fixed location, and the hydrocarbon accumulation occurred mainly in traps related to faults. The Miocene reservoirs with high porosity and high permeability were fed along faults by hydrocarbon from Mesozoic source rocks. These reservoirs have become exploration targets due to improved seismic reflection imaging (Fingleton and Zinni, 1999).

RESERVOIRS

The main reservoirs of Pabst Field are three sands referred to here by their depths: 10,000 ft (10,000') sand; 10,150 ft (10,150') sand; and 10,300 ft (10,300') sand (Figures 4, 5, 6). The package of the three sands is wedge-shaped with a maximum thickness of 600 ft. The three sands are separated by two shale intervals that are usually less than 100 ft thick. Well data reveal that the thickness of 10,000' sand ranges from 100 ft to

250 ft; 10,150' sand 50 ft to 250 ft; and 10,300' sand 50ft to 150 ft (Figure 7). Each sand also is interbedded with multiple thin shales a few feet thick.

The three sands display a fan shape in plan view. From a bounding primary growth fault on the northeast, the sand bodies spread to the southwest (Figure 8) and younger sands shift landward successively. Thus, the southern parts of 10,150' sand and 10,300' sand are directly overlain with shales (Figure 4).

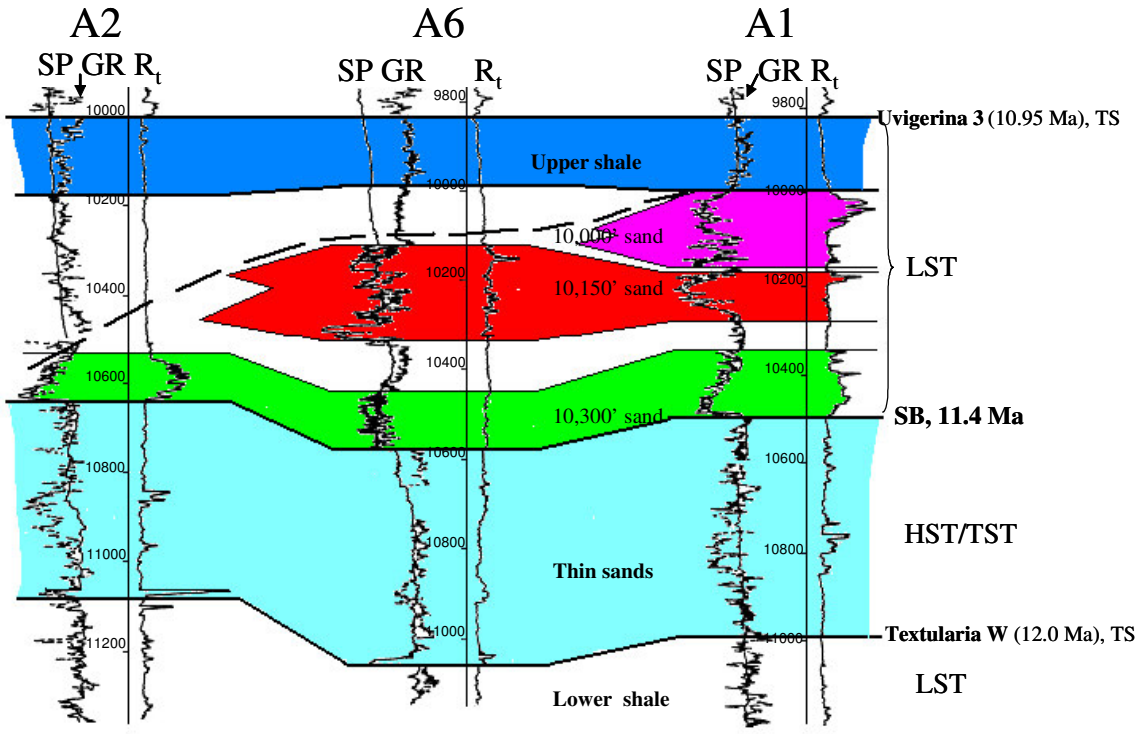

Figure 4. Well log correlation, showing the 10,000', 10,150' and 10,300' sands and the system tracts to which they belong. TS = Transgressive surface. SB = Sequence Boundary. Location is shown in Figure 5.

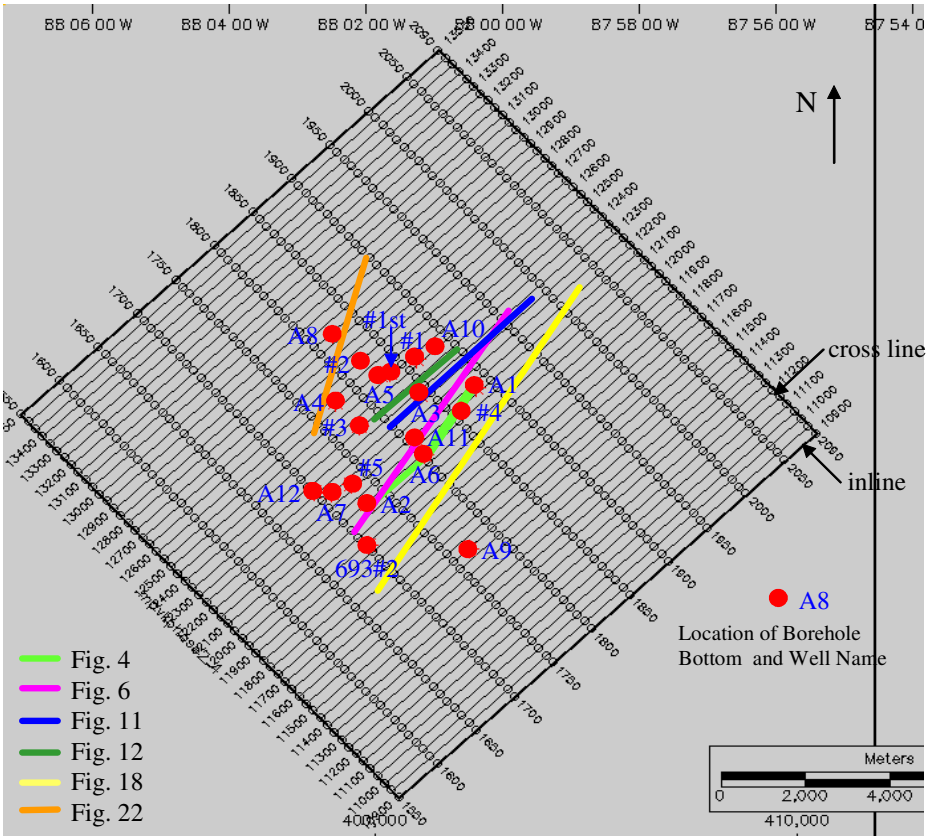

Figure 5. Locations of wells and seismic profiles shown in Figures 4, 6, 11, 12, 18 and 22.

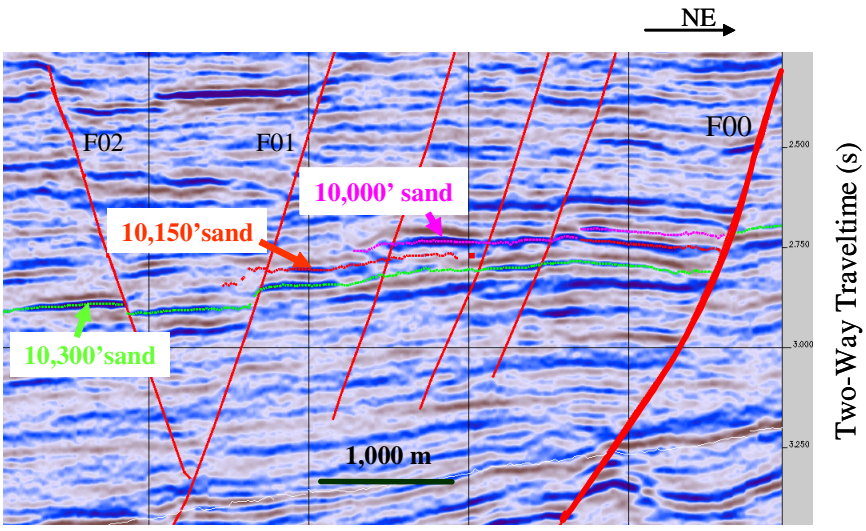

Figure 6. A seismic profile across Pabst Field, showing the rollover structure and the three reservoir sands. Location is shown in figure 5.

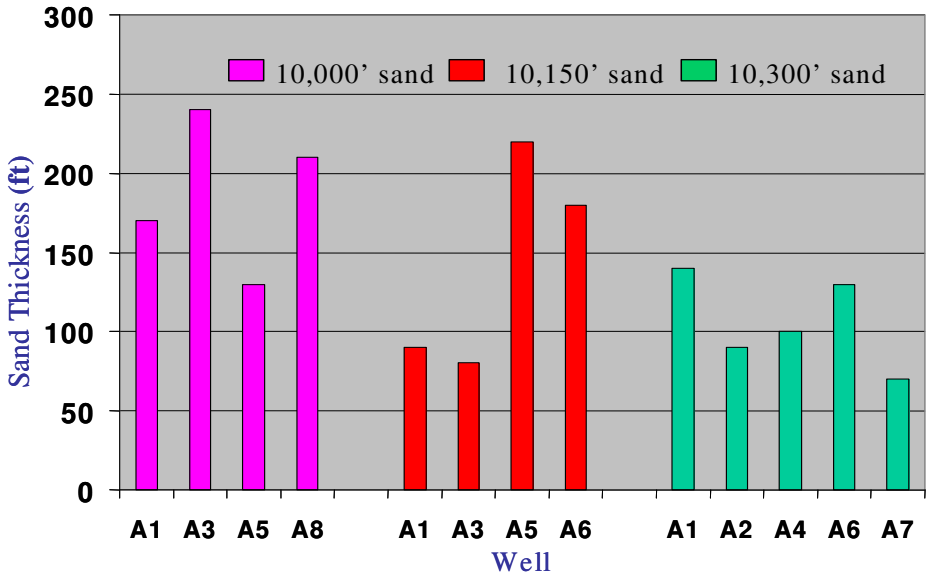

Figure 7. Thicknesses of the three reservoir sands from well log data.

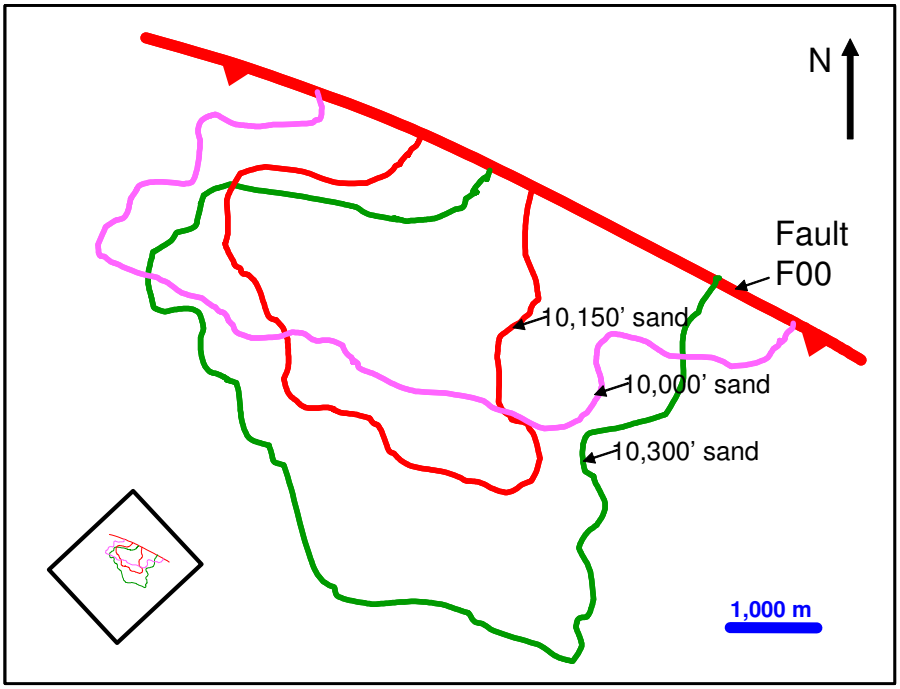

Figure 8. Distribution of reservoir sands in Pabst Field and their relationship to fault F00 in plan view. Note: 10,000' sand is younger than 10,150' sand and the 10,150' sand is younger than the 10,300' sand.

I used sequence stratigraphy analysis to interpret the sedimentary environment of the three sands and sand facies by interpreting well log data, seismic data, and paleo-zonation. A large section, with a thickness up to 1,300 ft, including three sands and their encompassing shale and other sands, is taken into account. From top to bottom, this section consists of the upper shale, the three sands, the thin sands, and the lower shale (Figure 4). The top of the upper shale is associated with the extinction of Uvigerina 3 (10.95 Ma), and the top of the lower shale is associated with extinction of Textularia W (12.0 Ma). Thus, the ages of the three sands are between 10.95 and 12.0 Ma.

The upper shale is pure shale and is about one hundred feet thick. It is characterized by high GR counts and a ramp-shape R_t curve in well log data. This shale unit is found in all wells and is a key marker used in well correlation and seismic interpretation. The lower shale is about 700 feet thick and also is characterized by high GR and low R_t.

Comparison of the section with the "Neocene Biostratigraphic Chart - Gulf of Mexico" (Figure 9, Paleo-Data, Inc. 2003) permits putting it into a sequence stratigraphy framework. Using this correlation, the three sands are dated to be of the late Middle Miocene age. The surfaces of 11.0 Ma and 11.9 Ma age are two transgressive surfaces (TSs), respectively, which incorporate a lowstand systems tract (LST) and a highstand systems tract/transgressive systems tract (HST/TST) from the top to the bottom (Figure 4). The top of the upper shale with high GR and low R_t is a stable and continuous reflector on the seismic profile in the study area. The bottom of 10,300' sand is a distinctive lithological break in the 11.0-11.9 Ma interval. According to the Biostratigraphic chart (Figure 9), the base of the 10,300' sand is interpreted as a

sequence boundary (11.4 Ma). Thus, the three sands and top shale are located in the LST.

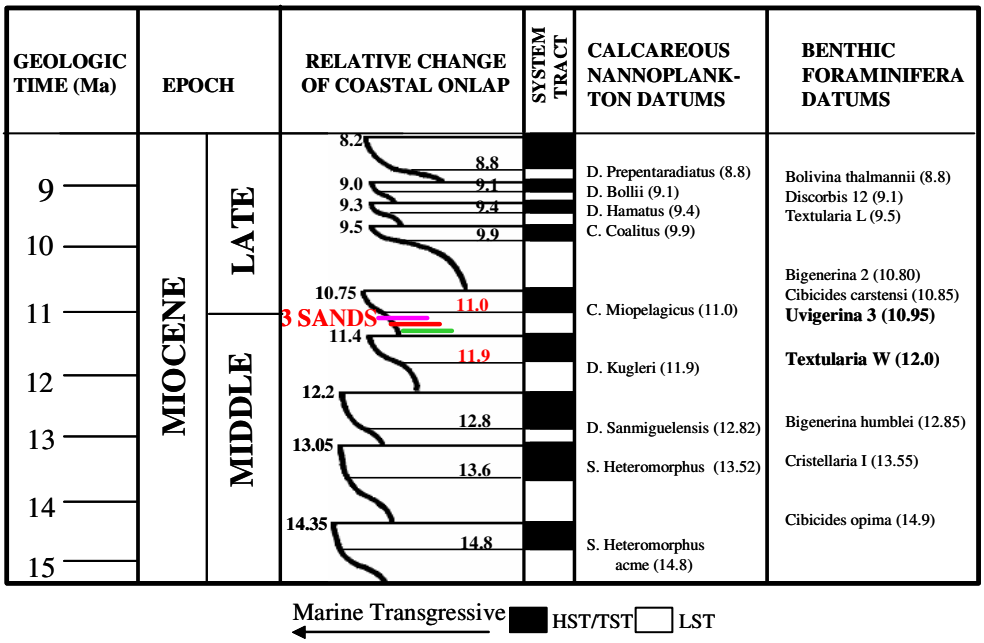

Figure 9. Middle and Upper Miocene stratigraphy and paleohorizons of the Mississippi Delta Margin region. The three sands are in the late Middle Miocene LST (10.95-11.4 Ma) (modified from Sunwoo, 1999 and Paleo-Data, Inc., 2003).

Based on Mitchum et al.'s (1990) well log and seismic models of LST sands, the three sands in Pabst Field are interpreted as a slope fan. SP/GR curves of the typical fan channel are characterized by a sharp base and a fining, upward "Christmas-tree" shape (Figure 10). For example, 10,300' sand in wells A1, A2 and A9 has this characteristic. A consistently rounded pattern of SP/GR indicates coarsening upward in the lower part of the levee and fining up in the upper part, and this pattern is found in 10,000' and

10,300’ sands. Almost all sands have “nervous” log character, suggesting sand-shale interbedding typical of a slope fan. In the seismic data, the reflections of the10,000’ sand and the 10,150’ sand have “V” or “U” shape that represent slope fan channel fill.

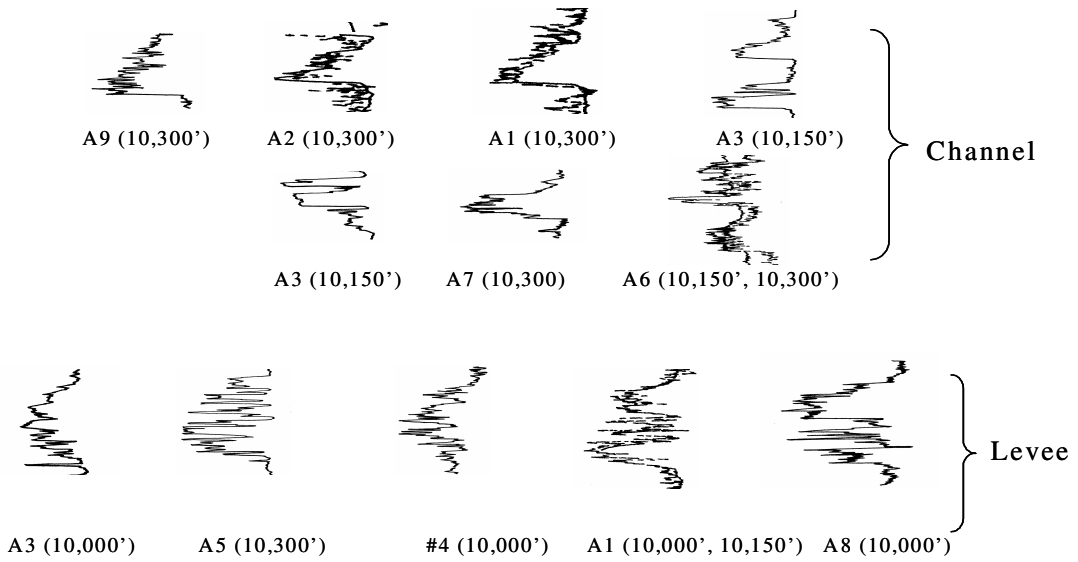

Figure 10. Well log curves of SP/GR, showing sand facies. The Christmas tree pattern and rounded pattern imply channel fill and levee of slope fan, respectively. The term before the parenthesis is the well name and the term within parenthesis is the name of the sand unit. The dash line is SP and the solid line is GR.

Furthermore, the channel fill of the 10,000’ sand cuts into the10,150’ sand, and the channel fill of the 10,150’ sand cuts the 10,300’ sand (Figures 11, 12). Well A10 reveals that the 10,000’ sand has overlain on the 10,150’ sand. The shale units between the 10,000’ sand and the 10,150’ sand, and between the 10,150’ sand and the 10,300’ sand in wells A1 and A5 near the incised area are only 10 ft thick (Figure 13), whereas the

thickness between the 10,000' sand and the 10,150' sand or the 10,150' sand and the 10,300' sand is generally about 100 ft. This demonstrates that the younger sand has nearly cut into older sand at the locations of these two wells. Younger sands cutting into the older sands may reflect slope fan erosion, which is common in LSTs during sea level fall or a still stand of sea level. Seismic data indicate that the three sands are partially merged. Places where the 10,150' sand and the 10,300' sand are in direct contact with the overlying 10,000' sand and 10,150' sand are referred to as "skylight windows".

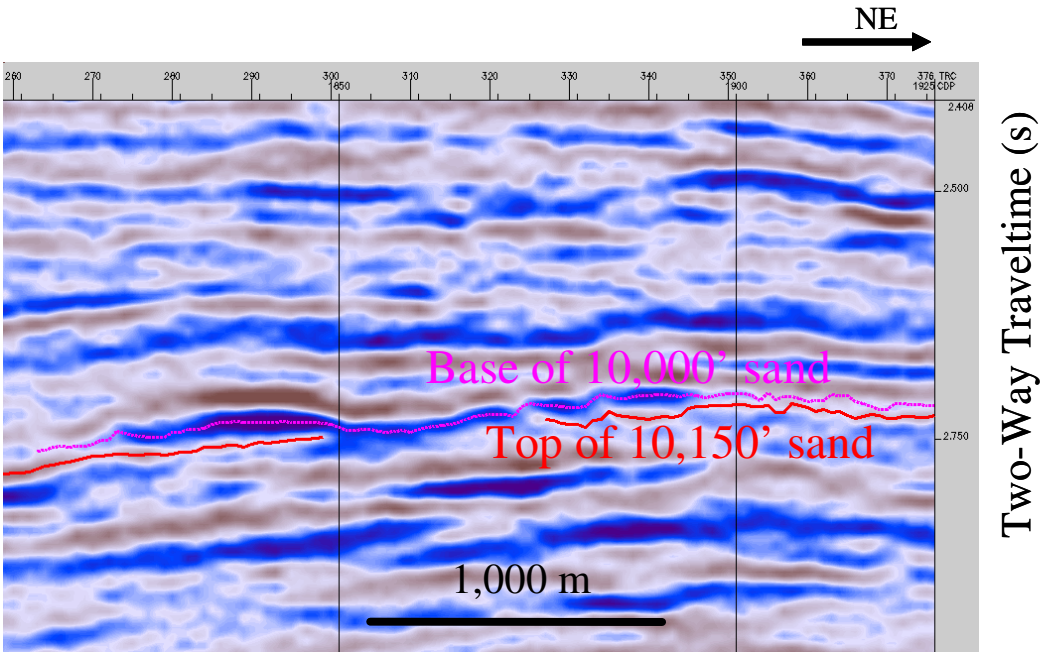

Figure 11. Seismic profile, line 12300, showing the 10,000' sand cutting into the 10,150' sand. A "skylight window" where the sands are in contact is formed. The cross cutting may allow fluid communication between the two sands. Location is shown in Figure 5.

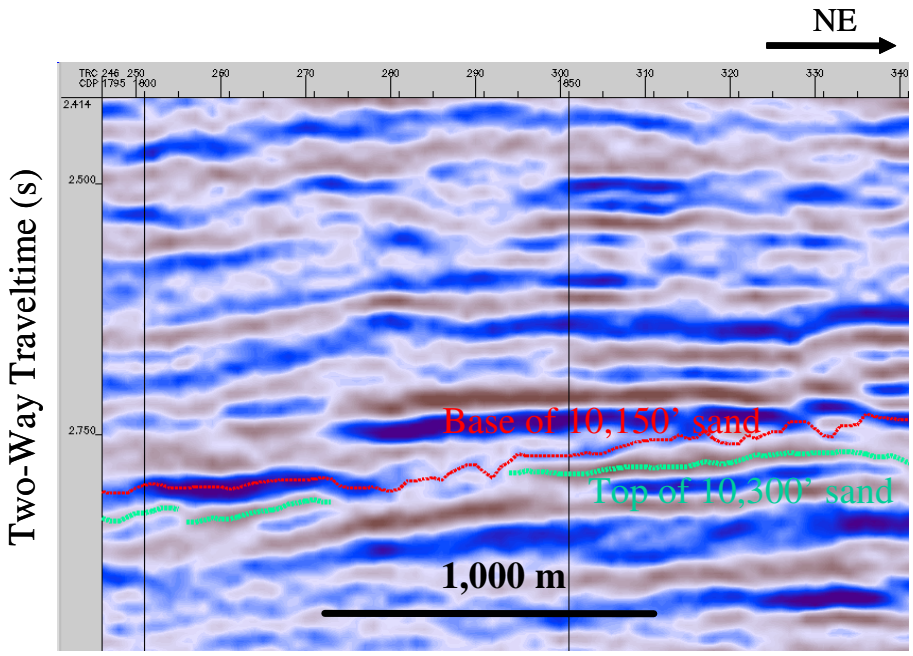

Figure 12. Seismic profile, line 12355, showing the 10,150' sand cutting into the 10,300' sand. A "skylight window" where the sands are in contact is formed. The cross cutting may allow fluid communication between the two sands. Location is shown in Figure 5.

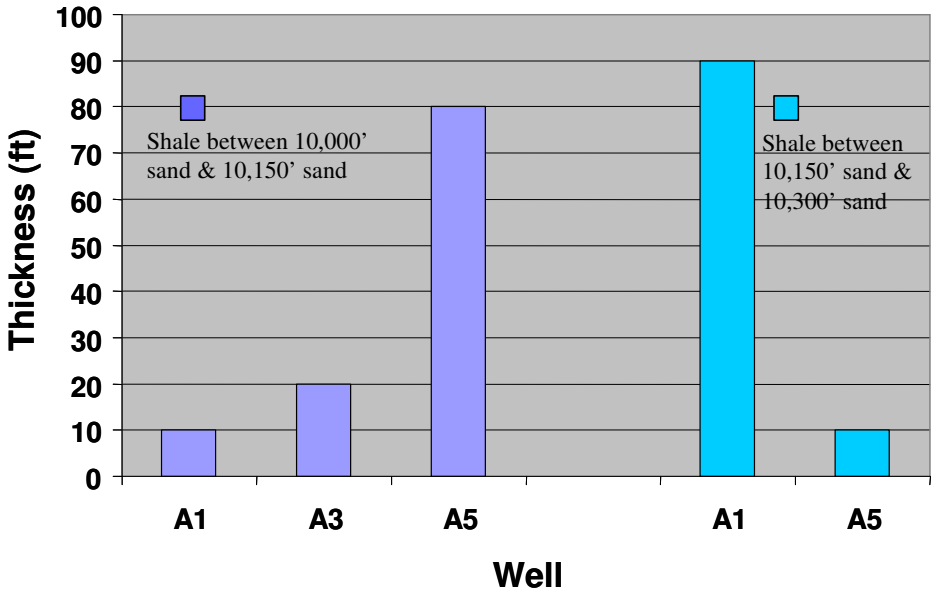

Figure 13. Interbedded shale thickness from well log data.

STRUCTURE, FAULTS, AND COMPARTMENTS

The three sands in Pabst Field form a rollover structure against a primary fault, F00, with a number of fault-related local highs (Figures 14, 15, 16, 17). The total area of the sands is 17 square miles. The existence of "skylight windows" between the sand units is demonstrated by the "holes" in the structure maps derived from the seismic data. The primary fault that has largest throw (maximum throw 675 ft) extends NWW for more than 6 miles. The fault flattens with depth in deep into the Mesozoic section, forming a "listric" shape. The character of fault F00 differs from other faults with approximately constant dip with depth, which may affect gas migration style. The primary fault

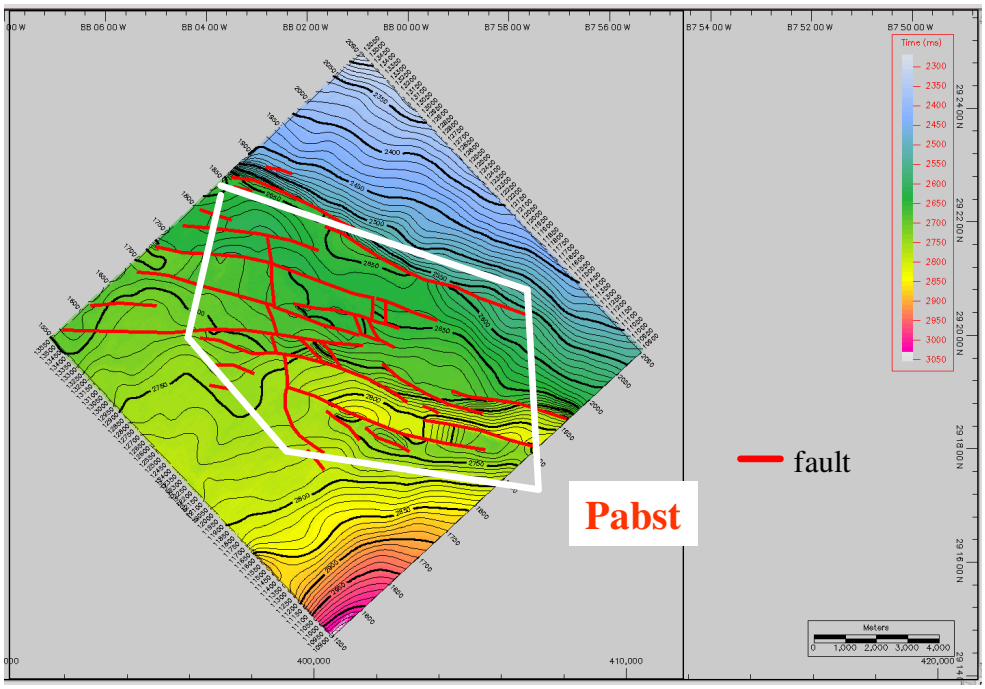

Figure 14. Time structure map of top of Middle Miocene (11 Ma) in study area. It shows a faulted rollover structure of Pabst Field. Contour interval is 10 ms.

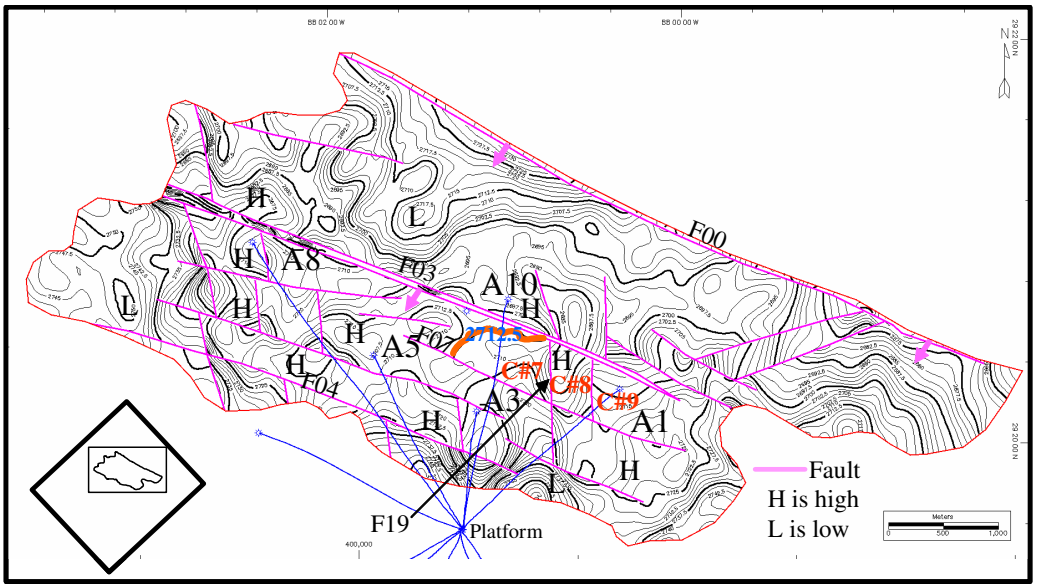

Figure 15. Time structure map of the 10,000' sand. Contour interval is 2.5 ms. F# represents fault name. A# represents well name. C#7 represents compartment #7.

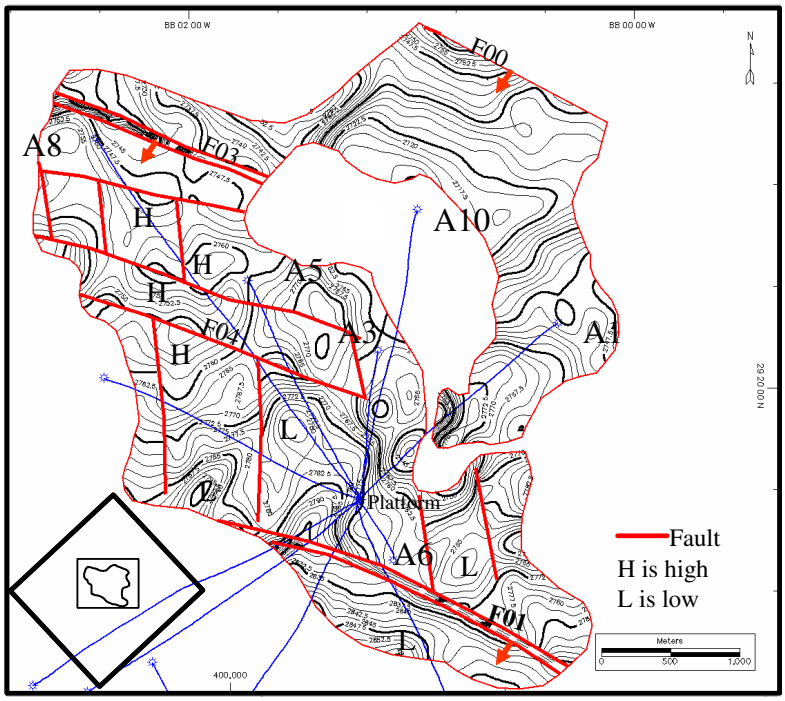

Figure 16. Time structure map of the 10,150' sand. Contour interval is 2.5 ms. F# represents fault name. A# represents well name.

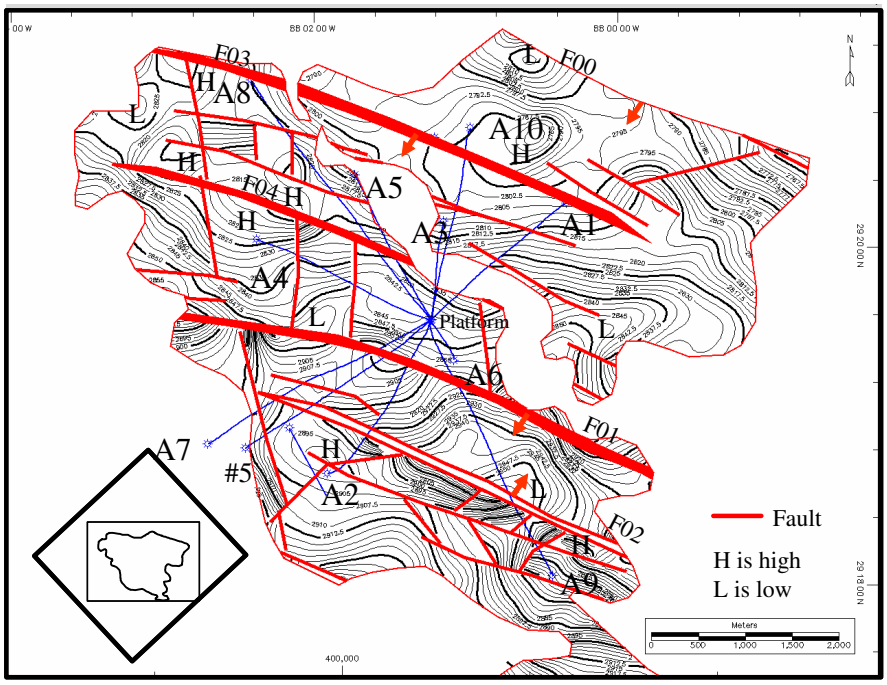

Figure 17. Time structure map of the 10,300' sand. Contour interval is 2.5 ms. F# represents fault name. A# represents well name.

controls the Middle Miocene deposits in which the sediment thickness in the hanging wall is 1.5-2 times thicker than that in the footwall (Figure 18). Two large synthetic faults (F01 and F03) and one large antithetic fault (F02) parallel with the primary fault.

The distribution of fault throw as determined from 3-D seismic data for major faults is shown in Figure 19. Table 1 provides a summary of maximum and average throws for the large faults. The maximum throw near the middle of fault F01 is 300 feet; while the maximum throw of fault F03 is 250 ft and the maximum throw of fault F02 is 550 ft. These large faults control the structure: between fault F00 and fault F01 are several local

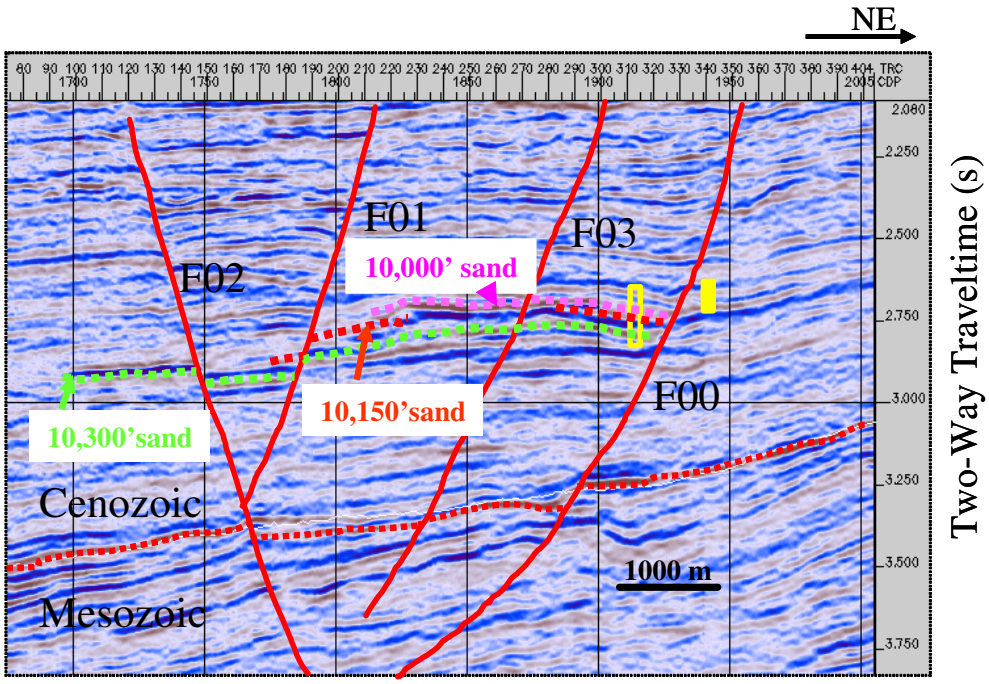

Figure 18. Seismic profile, showing the four major faults in Pabst Field. Fault F00 is a listric primary fault. Faults F01, F03 and F02 are synthetic and antithetic faults with high dip angles. The thickness of the section in the hanging wall strata are 1.5-2 times that of equivalent age strata in footwall (see yellow bars). Location is shown in Figure 5.

Table 1. Fault throws in Pabst Field

Fault Name	Maximum Throw, ft	Average Throw, ft
F00	675	438
F01	300	160
F02	550	325
F03	250	107
F04	50	28
F07	125	50

highs, and there is a graben between the synthetic fault F01 and the antithetic fault F02.

The average displacement is necessary for input into reservoir and fault models.

Smaller displacement faults are incorporated in the model. Faults with low throw and high dip angle were defined by Watkins (Watkins et al., 2001a) as Low Throw near Vertical Faults (LTNVFs). The LTNVFs have been increasingly studied because they significantly affect fluid flow (Knipe et al., 1998; Gibson, 1998). Because of their low throws, the LTNVFs are difficult to recognize and interpret on seismic profiles. Seismic attributes are widely used for the fault interpretation (Bahorich and Farmer, 1995; Kulander, 1999).

In this study small displacement faults are identified using two seismic attributes: coherency and "time" dip of seismic horizon as explained below. Fault geometry is best determined using coherency data cube together with seismic cross section profiles. The later also provides estimates of fault throw.

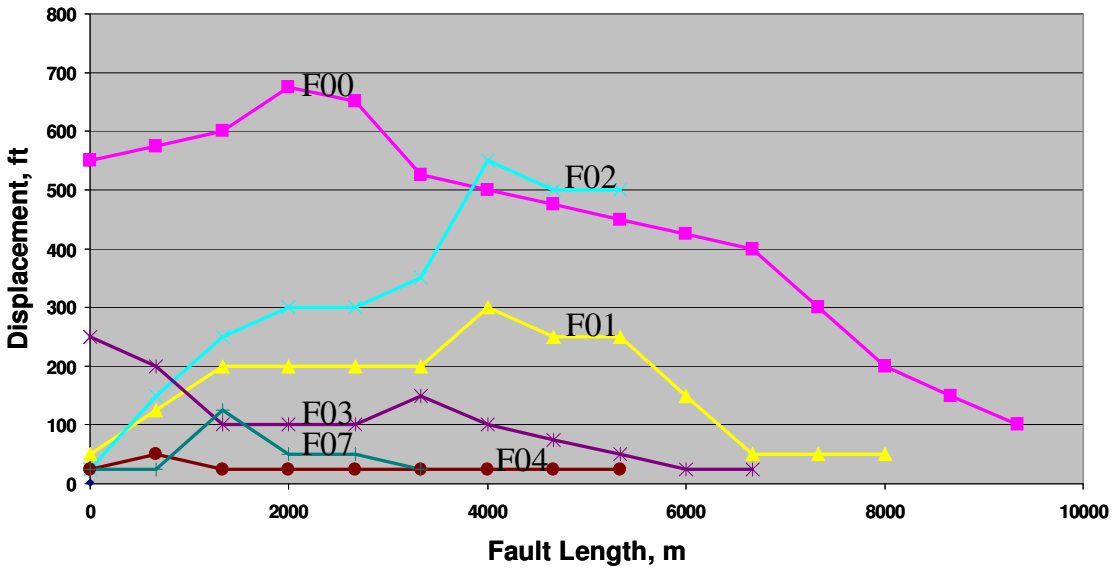

Figure 19. Fault displacement along fault trend, showing variation of fault displacement and fault length.

The seismic coherency provides a measure of statistical similarity or dissimilarity between an interval of a seismic channel record and records of a specified number of neighboring channels. A high coherency implies that records are nearly identical and hence local geology has no or only minor lateral change. A low coherency means significant differences between records and implies measurable lateral change in geology. Faults are one way to cause abrupt lateral change in geology, so faults may be seen as sites of low seismic coherency. In this study coherency is calculated by comparing a given recorded channel with other four neighboring channels. Figure 20 shows an example of a coherency map for a specific time interval. Areas of high coherency are white or light blue, whereas areas of low coherency are dark blue. The linear or curved dark zones are interpreted to be associated with faults.

A "time" dip ("time slope) is calculated for a specific seismic horizon using two-way traveltime to the horizon for three neighboring seismic records (a 3-ponts problem). The "time" dip value is expressed in Second per Foot. Figure 21 shows a "time" dip map of the top of 10,300' sand. The linear or curved zones of high "time" dip are interpreted to show location of faults offsetting this horizon. For example, the small faults (F26 and F13) can be discerned by the linear or curved zones.

I found 32 faults, many of which displace the three sands, but which die out within the upper shale and the lower shale. The interpretation of LTNVFs from coherency is confirmed by seismic cross section profiles perpendicular to fault trends. At least three horizons are cut by the faults (Figure 22). Thus, the throws of LTNVFs are measurable and can be used to constrain the structure model that is input into Eclipse®.

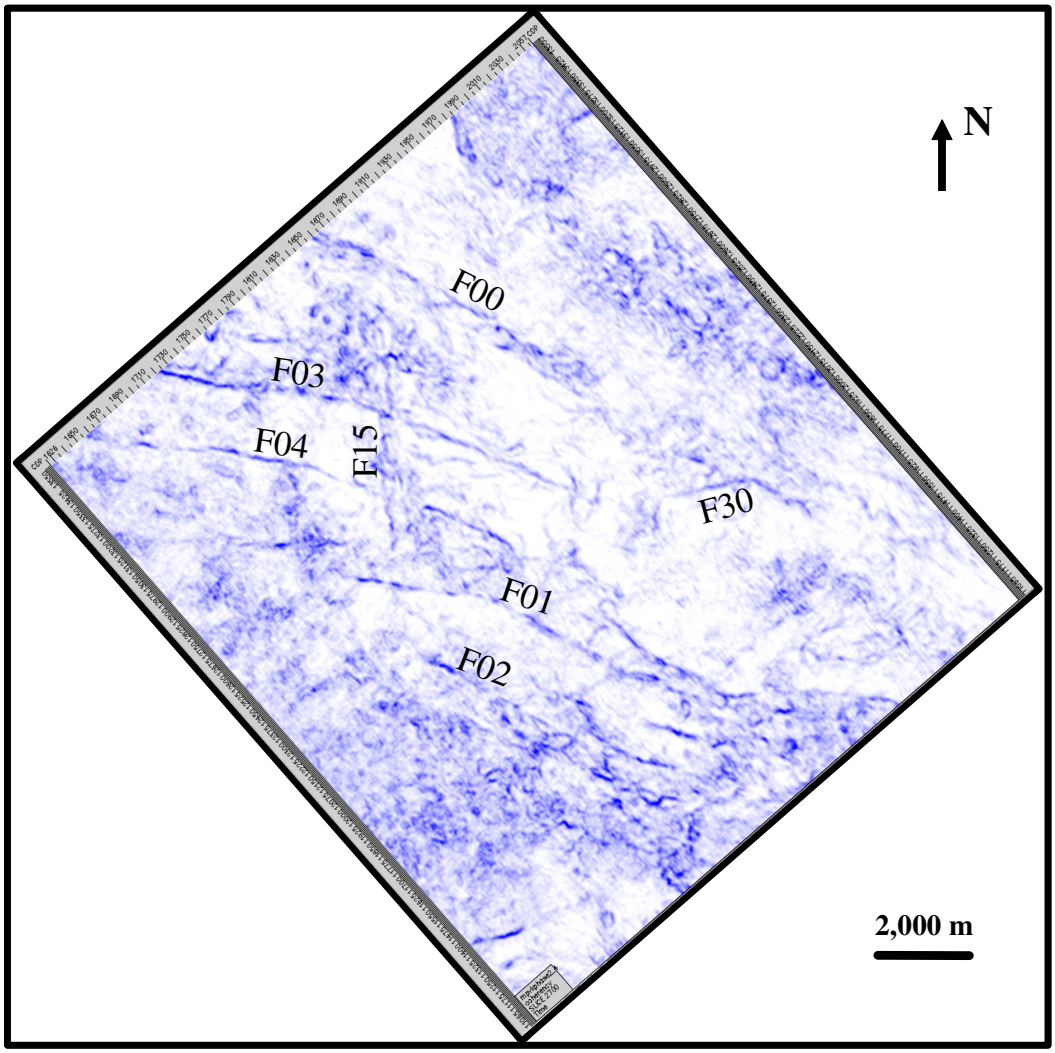

Figure 20. Coherency time slice at t=2700 ms, showing fault boundaries (linear or curved features).

Faults in Pabst Field form three fault families (Figure 23). Family 1 consists of the primary and secondary synthetic, antithetic faults and parallel LTNVFs, with northwest-west trends. Family 2 faults consist of north-south trending LTNVF cross faults, and are bound by Family 1 faults. Family 2 faults may form to accommodate strain associate

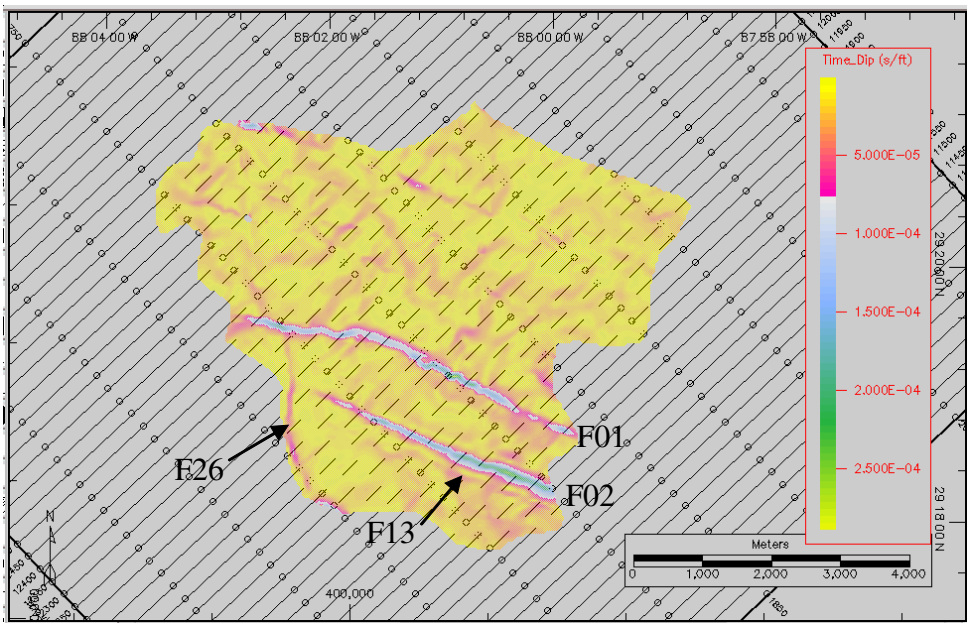

Figure 21. Dip of the horizon of 10,300' sand. The linear features indicated by arrows are interpreted to be the LTNVF boundaries.

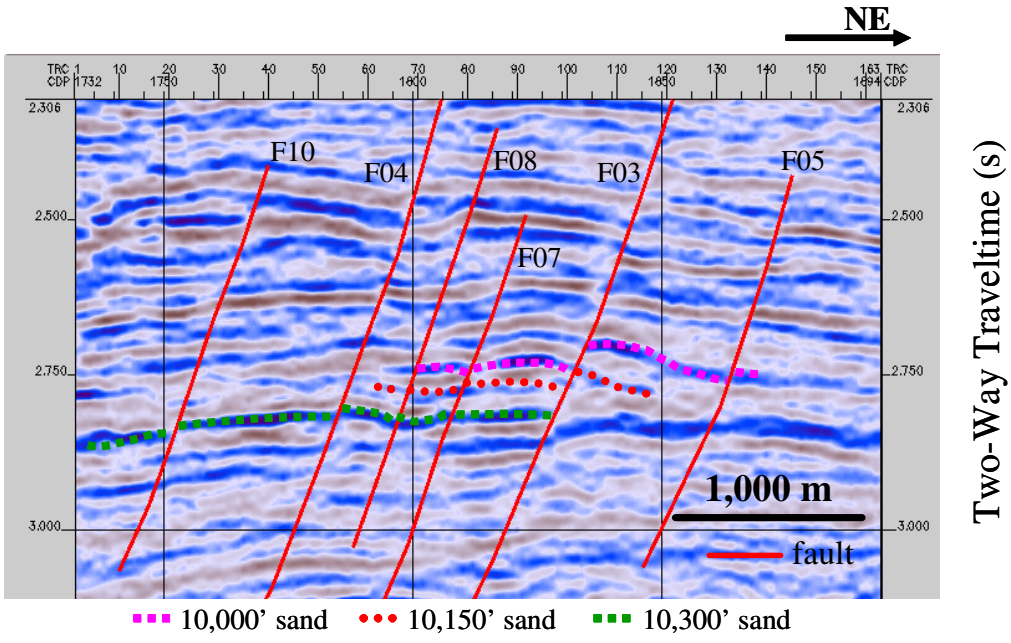

Figure 22. Seismic profile perpendicular to fault trends, showing LTNVFs. Three horizons, at least, are offset by a fault. Location is shown in Figure 5.

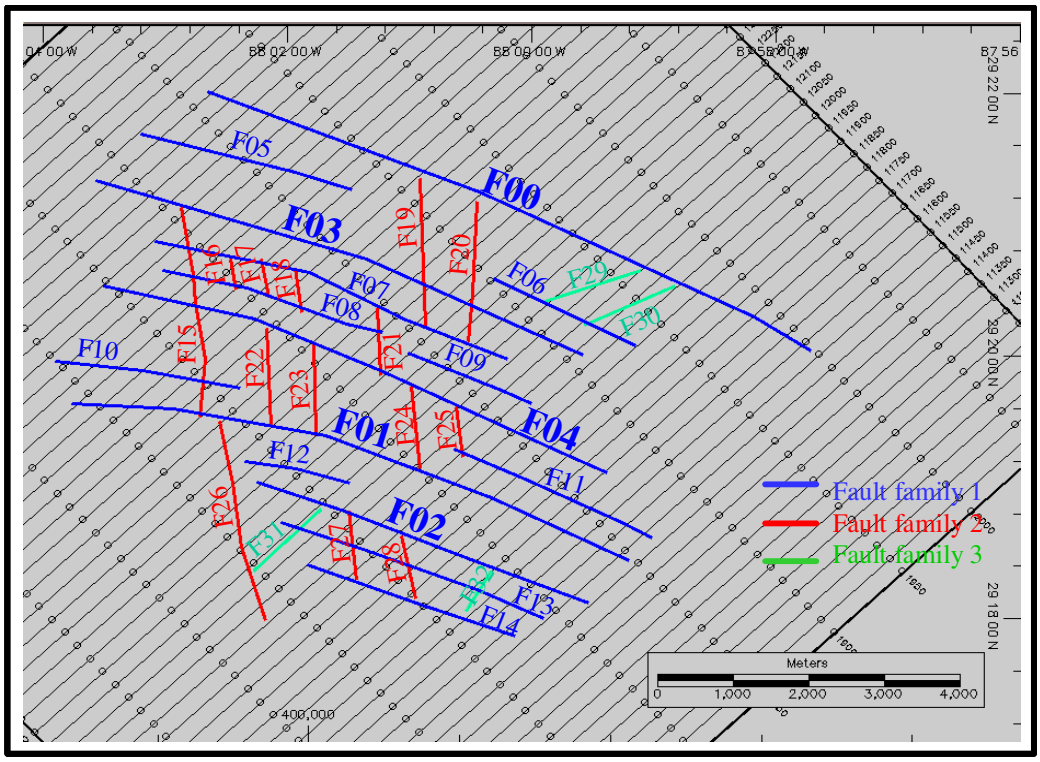

Figure 23. Fault map of Pabst Field, showing three fault families. F# represents fault name.

with lateral variation of displacement on Family1 faults. Family 3 faults consist of a few north-northeast trending LTNVFs.

The throw of the LTNVFs is approximately 25 ft. Thus, their throws are much smaller than the thickness of each of the three sands. The antithetic fault F02 has a maximum throw of 550 ft that decreases westward, and F02 dies out and does not intersects fault F26 (Figures 19, 23). Hence, the 10,300' sand is directly connected at the northwest end of F02, which provides a pathway between f02 and F26 for gas flow.

Reservoir compartments are usually defined by a structural factor, such as faults (Watkins et al., 1999a). Here I emphasize the influences of both stratigraphic and structural factors. From the fault map (Figure 23), the distances between neighboring synthetic and antithetic faults of the fault Family 1 are about one mile. The reservoirs are thus cut by the faults into one-mile strips. Meanwhile, fault Family 2 intersects fault Family 1, which subdivides the reservoirs into a number of blocks bounded by faults.

Because the faults act as baffles for gas flow, the fault blocks become structurally controlled compartments under some conditions, such as when the fluid pressure in the compartment is lower than fault capillary displacement pressure. In the 10,000' sand (Figure 15), faults F07, F03, and F19 bound compartment number 7 (C#7). Fault F19 forms a common boundary with adjacent C#8. The structurally controlled compartments are further complicated by the younger sand cutting into the older sand. The compartment model is shown in Figure 24. The compartments in the three sands are numbered in the figures on pages 78, 79 and 80. It is likely that gas migration in and between these compartments will have complex migration paths.

GAS DISTRIBUTION AND FORMATION PRESSURE

Gas-charged sands are identified from well log and well testing data. The R_t of gas-charged sands (>3 ohmmeter) from R_t log is usually 2 times that of water-charged reservoir zones (1.5 ohmmeter). In a sonic log the sonic velocity of gas-charged sand is lower than the sonic velocity of water-charged sand, while the sonic velocity of water-charged sand is lower than the sonic velocity of surrounding shale. For example, the

velocity of gas-charged sand in well #2 is 9,524 ft/s, but the velocity of water-charged sand is 10,526 ft/s, and the velocity of shale is 10,989 ft/s. The gas in the sand reduces both the velocity and the density of the sand reservoirs. Thus the impedance contrast is enhanced between gas-charged sand and either water-charged sands or shales.

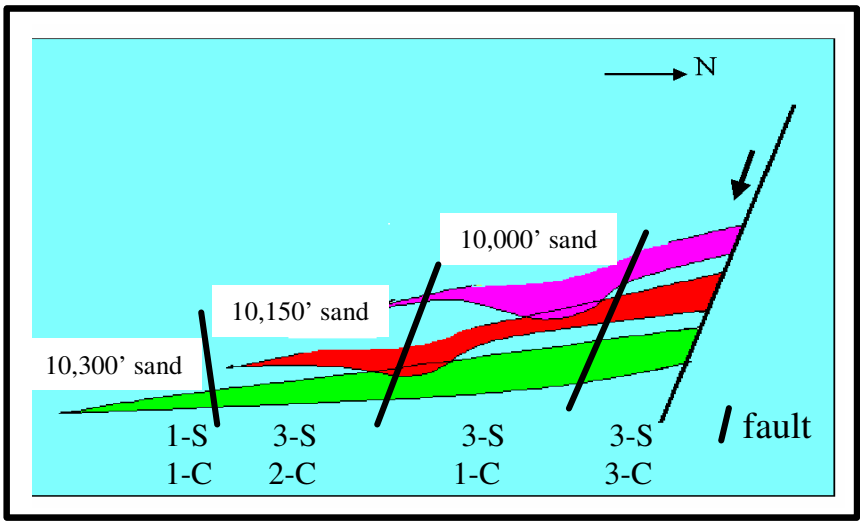

Figure 24. Schematic compartment model of Pabst Field. C=compartment, and S=sand. 3-S, 3-C means that three sands compose three compartments separately. 3-S, 1-C means that three sands compose one compartment caused by sand contacts. (Not to scale.)

The amplitude anomalies become a gas indicator in Pabst field and were used to interpret the gas distribution. Constrained by well data, the amplitude anomalies reveal the location of gas but are not used to estimate the degree of gas saturation (Figures 25, 26, 27). In the 10,000' sand, gas has accumulated mainly in the compartments between fault F03 and fault F04 (Figure 25), and a few gas accumulations are located near the

primary fault F00. In the 10,150' sand, gas accumulation occurs in compartments along fault F03 and fault F04 (Figure 26). In the10,300' sand, there is evidence of gas accumulation in the compartments between fault F04 and fault F01 and on the upthrown side of fault F02. Between fault F01 and F02 is a graben in which the 10,300' sand is characterized by a medium amplitude anomaly that indicates an uncertain gas distribution (Figure 27).

Well-testing data indicate that Pabst Field has normal formation pressure. For example, the formation pressure of the 10,300' sand in well A4, at a depth of 10,408 ft, is 4,796 psia (pounds per square inch). However, the rate of production pressure drop in well A2 differs from the rate of production pressure drop in well A9. This difference is probably caused by compartmentalization.

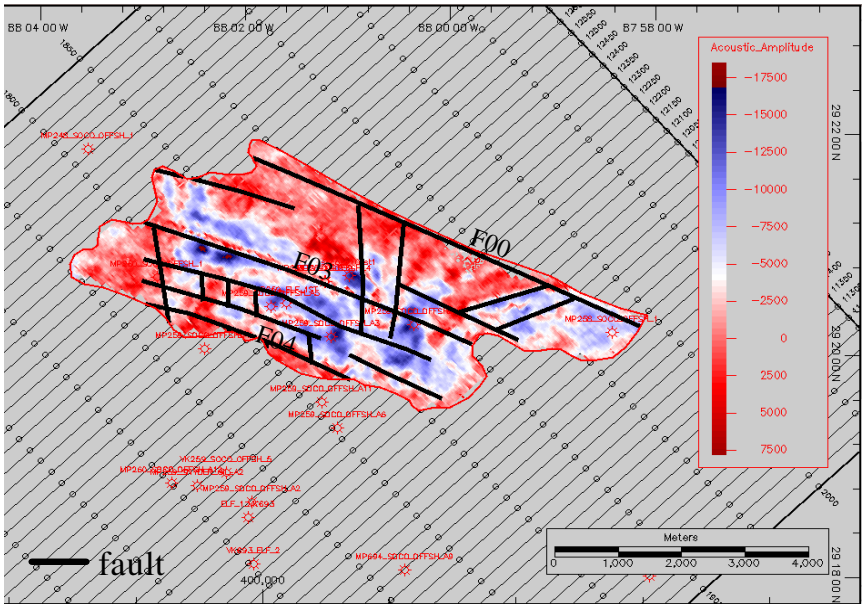

Figure 25. Amplitude anomaly of 10,000' sand, showing gas distribution (the amplitude anomaly is from -12,500 to - 16,500).

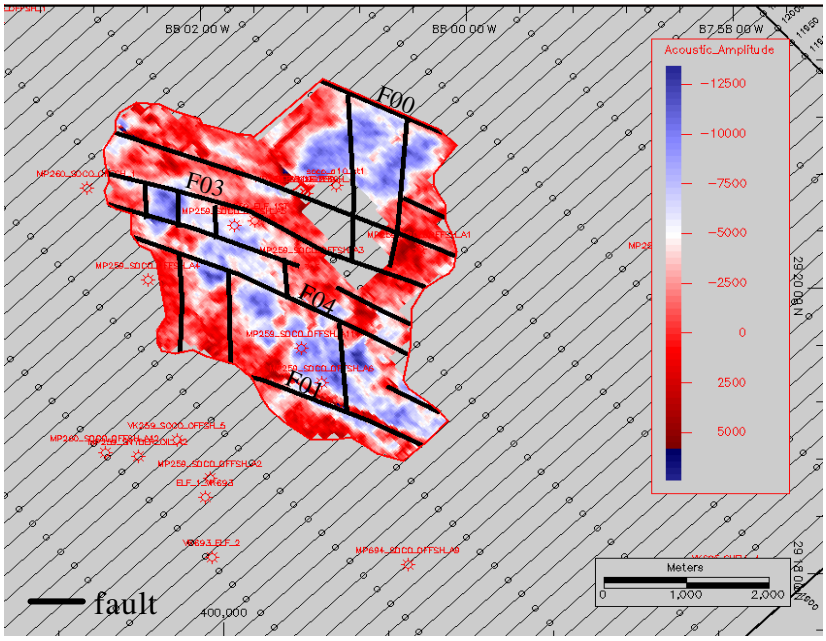

Figure 26. Amplitude anomaly of 10,150' sand, showing gas distribution (the amplitude anomaly is from -12,500 to -14,000).

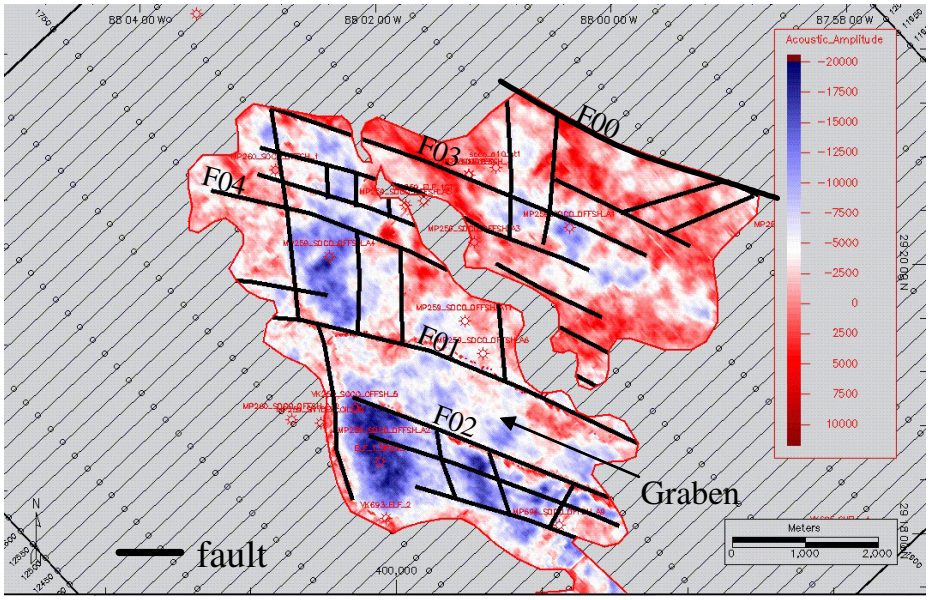

Figure 27. Amplitude anomaly of 10,300' sand, showing gas distribution (the amplitude anomaly is from -12,500 to -20,000).

CHARACTERISTICS OF GAS

Pabst Field is first gas field in Main Pass area that contains gas and minor condensate, and differs from nearby oil fields that contain medium matured oil. The amount of methane in gas is high, 95.6 % (dry gas), and δ^{13} C values of methane (29.1% PDB, C13/C12, Pee Dee Belemnite), ethane (25.6% PDB), and propane (24.4% PDB) are high, implying that the gas is highly matured (Sassen et al., 2001). The carbon isotope content of the condensate varies from compartment to compartment, which indicates that hydrocarbon migration and accumulation are affected by stratigraphy and structure. Sassen et al. (2001) suggested that Pabst Field was first gas field in the Main Pass area and was formed fairly recently (<1 Ma) or still archiving being charged from the Upper Cretaceous source rock in multiple charges.

CHAPTER III

NUMERICAL MODELS

To build a simulation model for reservoir-scale modeling, a number of parameters are required. These include geometries and properties of reservoir sand bodies, shale sealing horizons, and faults, as well as fluid properties (Table 2). The geometry, thickness, and depth of the sands and shales, as well as the fault pattern derived from structure maps and isopach maps were calibrated using well data. Gas supply style, including the gas charge pattern, charge rate, and duration also is required. These parameters come from geological model (including stratigraphy and faults), capillary pressure model, porosity and permeability model, relative permeability model, and fluid properties. Based on these parameters, an initial Eclipse® model was constructed. In the Eclipse® model the history of gas/water saturation, pressure, and gas flow for each cell are calculated, simulating the dynamic process of fluid flow in reservoirs and fault zones. The Eclipse® model was refined subsequently using results of the early simulations.

GEOLOGICAL MODEL

A geological model includes the gas migration pathway, charge rate, charge time, and duration of gas supply. Reservoirs in Pabst Field are interbedded sands within Miocene shales that are not source rocks. Geochemical data demonstrate that gas in the field comes from older and deeper source rocks (Sassen et al., 2001). As kerogen or oil is converted into highly-matured gas, the gas expands, which can cause overpressure if

Table 2. Parameters input into the models.

name	code	unit	formula	value
capillary pressure	P_c	psia	(4)	
reservoir porosity	Φ	fraction		0.25
reservoir permeability	k	md		75
shale porosity	Φ	fraction		0.15
shale permeability	k	md		0.00001
fault thickness	T_f	ft	(1)	
fault porosity	Φ_f	fraction	(2)	
fault permeability	k_f	md	(2)	
fault geometrical factor	F_g	fraction	(7)	
gas relative permeability	k_{rg}	fraction	(10a)	
water relative permeability	k_{rw}	fraction	(10b)	
gas saturation	s_g	fraction		0
water saturation	s_w	fraction		1
irreducible water saturation	s_{iw}	fraction		0.22
reservoir temperature	^oF	degree		202.6
formation pressure gradient	$P_{gradient}$	psia/ft		0.46
gas density	ρ_g	lb/cuft		0.044
gas specific gravity	γ_g	fraction		0.59
gas formation volume factor	B_g	fraction	(17)	
gas viscosity	μ_g	cp	(22)	
water density	ρ_w	lb/cuft		68.6708
water formation volume	B_w	fraction		Table 4
water viscosity	μ_w	cp		0.7588
rock (sand, fault, and shale) compressibility	c_f	$psia^{-1}$		$3.3x10^{-6}$

local rock permeability is too low to permit excess pressure to dissipate sufficiently quickly (Osborne and Swarbrick, 1997). It is the overpressure that forces the gas to migrate vertically along micro-fractures and faults into overlying strata. The amount of

the overpressure is proportional to the amount of gas (Berg and Gangi, 1999). The pressure gradient is also determined by the properties of faults and reservoirs. As overpressured gas moves into low permeability reservoirs and faults, which results in development of large pressure gradient. As the gas migrates up and charges reservoirs or disperses in upper strata, the overpressure drops so that gas migration may pause because of lack of the driving force. Continued gas generation in the source rock renews the driving pressure needed for gas to migrate up and charge reservoirs in another episode. The pattern of gas migration is "gas generation → overpressure → gas migration→ gas charge and dispersion → pressure drop→ migration stops". This process can be repeated multiple times, charging reservoirs in multiple pulses. In addition, overpressure is necessary for gas to overcome the fault capillary pressure so that the gas can flow across the fault. The process has been observed in other fields as well (Schowalter, 1979; Harris et al., 1999). It has been suggested that Pabst Field was charged by overpressured gas along faults in multiple pulses (Watkins et al., 1999a, Sassen et al., 2001). The charge faults, the charge rate, the charge time, and duration were tested by modeling as described in the following chapters.

FAULT ARCHITECTURE AND PETROPHYSICAL PROPERTIES

In studies of fault architecture and its effect on fluid flow (Knipe et al., 1998), it has been realized that a fault is a complex zone rather than a simple single plane. Previous modeling by IRIG investigated primarily the effect of the petrophysical properties of faults on fluid flow along and across fault zones (Watkins et al., 1999a). Faulting within

the reservoir produces significant deformation of reservoir sand. The rotation, cataclasis, and displacement of grains in a fault as well as the addition of clay components to fault zones reduce the porosity and permeability in the fault zone (Yielding et al., 1992).

Faults in a subsurface basin rarely are observed directly. Studies of fault architecture and petrophysical properties are accomplished by means of surface outcrop and drilling and logging data (Antonellini and Aydin, 1994; Berg and Avery, 1995; Matthai et al., 1998; Fisher and Knipe, 1998 and Johnson et al., 1999).

Caine et al. (1996) classified fault architecture into four types, based on the percentages of core zone (gouge and cataclasite) and damage zone (fractures and veins). Percentage core zone is defined as core width/ total fault zone width (total width = core width + damage zone width). Percentage damage zone is defined by damage zone width/total fault zone width. Faults with a high percent core zone act as barriers to flow, whereas faults with a high percent damage zone acts as conduits (Figure 28). A fault with a narrow fault-zone width and a low percentage of damage zones tends to act as barriers (Figure 29). Berg and Avery (1995) suggested a faulted reservoir in the Gulf of Mexico basin as a reservoir separated from a second reservoir by a shear zone that is equivalent to Caine et al.'s core zone. Their results indicate that the petrophysical properties of faults are very different from those of reservoirs.

In this study, a fault is represented by a shear zone of finite width consisting of deformed protolith. Some researchers suggested a "damage zone" occurs adjacent the

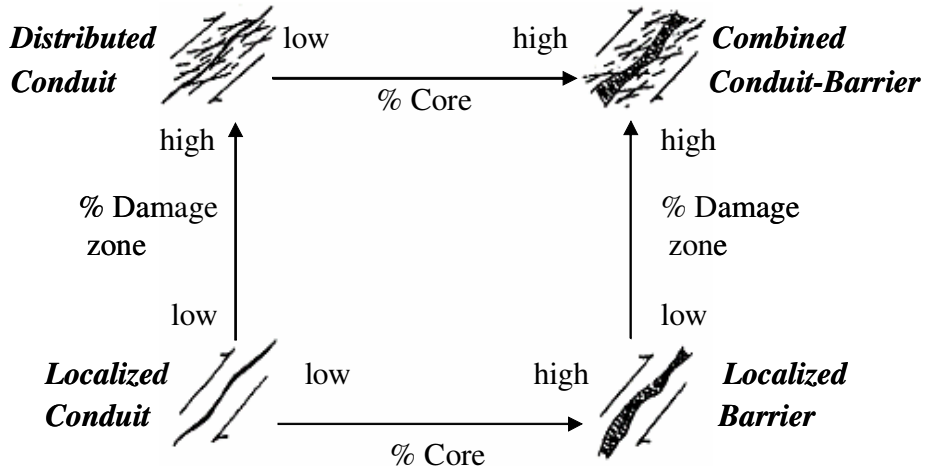

Figure 28. Classification of fault zones and fault-related fluid flow. Percent core is defined as fault core width/ total fault zone width. Percent damage zone is defined as damage zone width/total fault zone width. The total width = core width + damage zone width. Faults with a high percent core zone act as barriers, whereas faults with high percent damage zone act as conduits (Modified from Caine et al., 1999).

shear zone. In this modeling, however, a damage zoned is assumed to not exist. The permeability of the shear zone rock is assumed to be lower than sand protolith because of shear-induce texture changes and incorporation of clay from interbedded shales. Field evidence from Pabst Field indicates that faults act as both barriers and conduit to cross-fault flow based on fluid flow pressure during the gas production. In the model, shear zone permeability is assumed to be isotropic. One of the objectives of the modeling is to estimated shear zone permeability of faults in Pabst Field.

The thickness of shear zone is an important model parameter. Ibanez (2000) described the architecture and permeability of fault shear zones developed in Cambrian sandstone in central Texas. Based on his observations, Ibanez suggested a revised

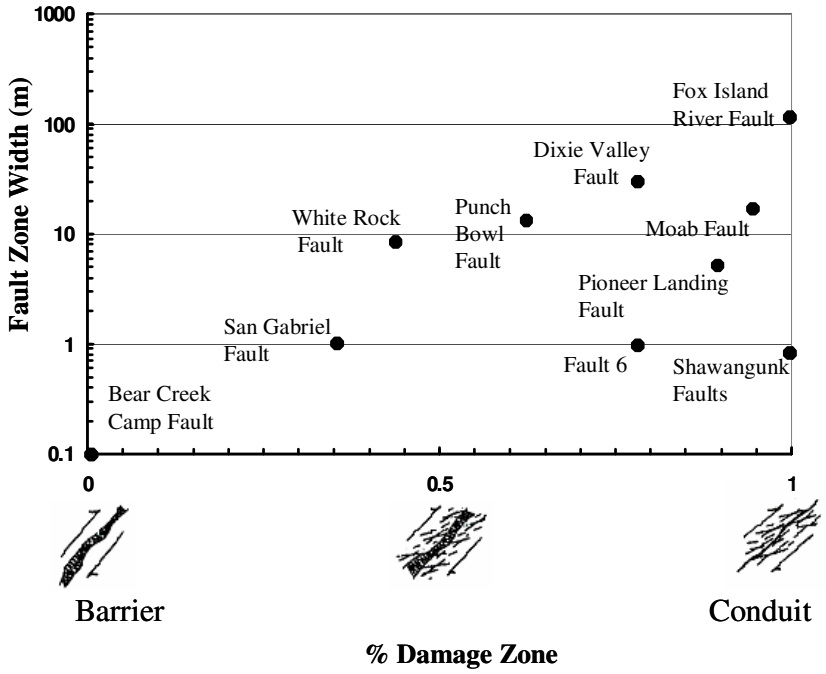

Figure 29. Fault zone architecture and permeability structure plot. Faults with narrow fault zone widths and low percent damage zone tend to act as barriers. (Modified from Caine et al., 1999).

relationship between throw and fault thickness (thickness of shear zone) as:

$$D_f = 23.4\ T_f^{0.90} \quad (1)$$

where, D_f is stratigraphic throw, ft and T_f is fault thickness, ft.

Both fault throw and thickness are required to model the reservoirs. For this study, fault throws were measured from seismic cross section profiles, and fault thicknesses were estimated by using formula (1). The thickness of the shear zone of the faults in Pabst Field ranges from 2-20 ft (0.6-6 m).

A relationship between fault porosity and permeability is needed to estimate capillary pressure, which determines the trapping capacity of faults. These data are not available for Pabst Field. To construct an empirical relationship between fault porosity and permeability, I collected porosity and permeability data from studies done by Berg and Avery (1995), Hintz (2001), and Kim et al. (2001) in the Gulf of Mexico Basin (Table 3). I did a linear regression to obtain a statistical relationship between fault porosity and permeability:

$$k_f = 10^8 \phi_f^{8.59} \quad (2)$$

where, k_f is fault permeability and ϕ_f is fault porosity.

Table 3. Porosity vs. permeability data from fault zones.

sample #	φ, fraction	k, md	sample #	φ, fraction	k, md	sample #	φ, fraction	k, md
1	0.083	0.02	9	0.099	0.08	17	0.104	0.3
2	0.12	3	10	0.12	0.15	18	0.107	0.9
3	0.13	22	11	0.108	0.18	19	0.143	61.6
4	0.13	0.12	12	0.124	0.19	20	0.135	3.474
5	0.14	17	13	0.116	0.09	21	0.125	20.56
6	0.15	3	14	0.1	0.19	22	0.097	1.66
7	0.15	11	15	0.073	0.09			
8	0.17	37	16	0.124	0.9			

Coates' equation has been used to describe the relationship between porosity and permeability in reservoirs (Ahmed et al. 1989).

$$k = 10^4 \left(\frac{1 - S_{iw}}{S_{iw}} \right)^2 \phi^4 \qquad (3)$$

where, k is permeability, S_{iw} is irreducible water saturation, and ϕ is porosity. S_{iw} is taken to be 0.22.

Comparison of the curves from Coates' equation and equation (2) indicates that, for ϕ_f<0.1, the permeability calculated from (2) is much lower than the permeability estimated from (3). Fault permeability decreases dramatically with decreasing porosity (Figure 30). The lower fault permeability may reflect the influence of smaller grain size

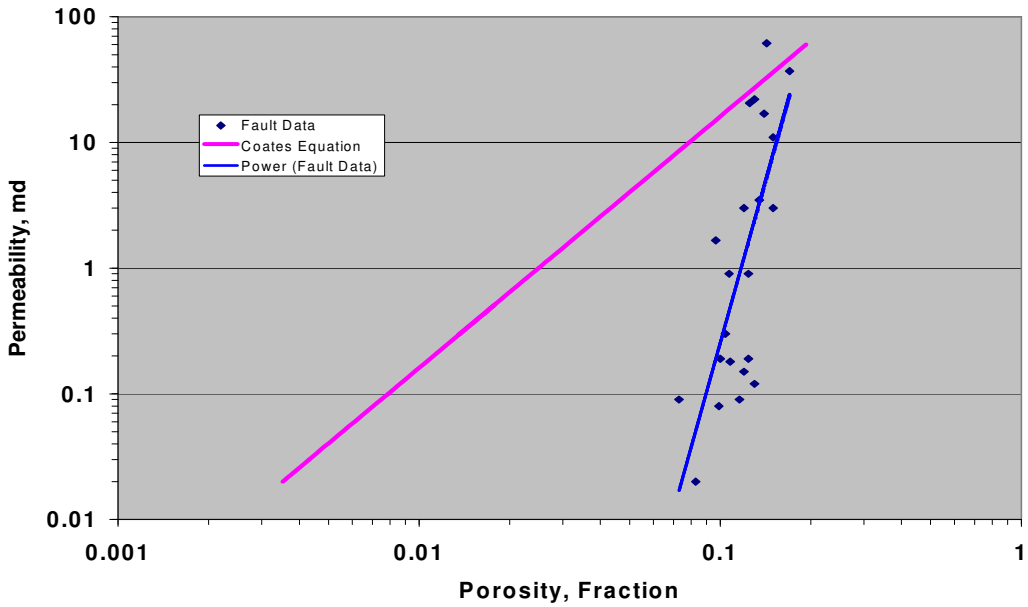

Figure 30. Porosity vs. permeability of faults. Compared with Coates equation for reservoirs (pink curve), the fault data show a narrow porosity range that reflects more complex pore structure of faults than that of reservoirs.

and more complex pore structure of faults than the surrounding reservoirs. In general, a fault has a much lower permeability than a reservoir, if faults have the same porosity as reservoirs. For this study, the formula (2) is more realistic than (3) for estimating fault permeability from porosity. Therefore, I used formula (2) instead of (3) to estimate fault permeability from porosity even though the data set used to establish formula (2) is small (22 data points), and the correlation is comparatively low (R^2=0.53).

ESTIMATION OF TRAPPING CAPACITY OF FAULTS

Fault trapping capacity, which is the ability to trap gas or oil, is estimated from capillary pressures of both reservoir and fault. The capillary pressure, P_c is defined as the pressure difference between gas (the non-wetting phase) and water (the wetting phase) as a function of the gas saturation S_g. Capillary pressures are measured in the laboratory by injecting non-wetting mercury into a dried, air-wet rock sample. The relationship between P_c and S_g is required by the simulator. Berg (1975) suggested a simple relationship between capillary pressure P_c and the capillary pressure for mercury and air, P_{cma}.

$$P_c = 0.08 P_{cma} \tag{4}$$

where

$$P_{cma} = 10^{\left[\log P_d - F_g / \ln(S_g)\right]} \tag{5}$$

and

$$P_d = \frac{\phi \left(3.8068 F_g^{-1.334}\right)^{\frac{1}{2}}}{k^{\frac{1}{2}}} \quad (6)$$

(Thomeer, 1960, 1983)

Here P_d is extrapolated displacement pressure for an initial entry of mercury into the largest pore throat in a rock sample. F_g is a geometrical factor. F_g is used to describes the apex curvature of the injection curve and indicates the pore-throat size distribution. A larger F_g suggests a more complex pore-throat. The difference in petrophysical properties between faults and their protolith is caused by their pore structure. Faults have more complex pore structure than their protolith.

Hawkins et al. (1993) proposed the following equations to calculate F_g from porosity, permeability and P_{cma} for sand reservoirs:

$$F_g = 0.4342\left[\ln\left(5.21\frac{k^{0.1254}}{\phi}\right)\right]^2 \quad (7)$$

$$P_d = 937.8/\left(k^{0.3406}\phi\right) \quad (8)$$

$$P_{cma} = 10^{\left(-F_g/\ln(1-S_w)+\log P_d\right)} \quad (9)$$

Hintz (2001) compared several methods (Pittman, 1992; Hawkins et al., 1993 and Thomeer, 1983) and concluded that the estimated capillary pressure generated by using Hawkins' method is closer to the measured capillary pressures in faults. Thus, I combine formulas (4), (7), (8), and (9) to calculate the relationship between P_c and S_g (Figure 31). The formulas above indicate that the capillary pressure is associated with

both the permeability and porosity. In modeling, if one changes the fault permeability, then the fault capillary pressure also is changed, because they are interrelated.

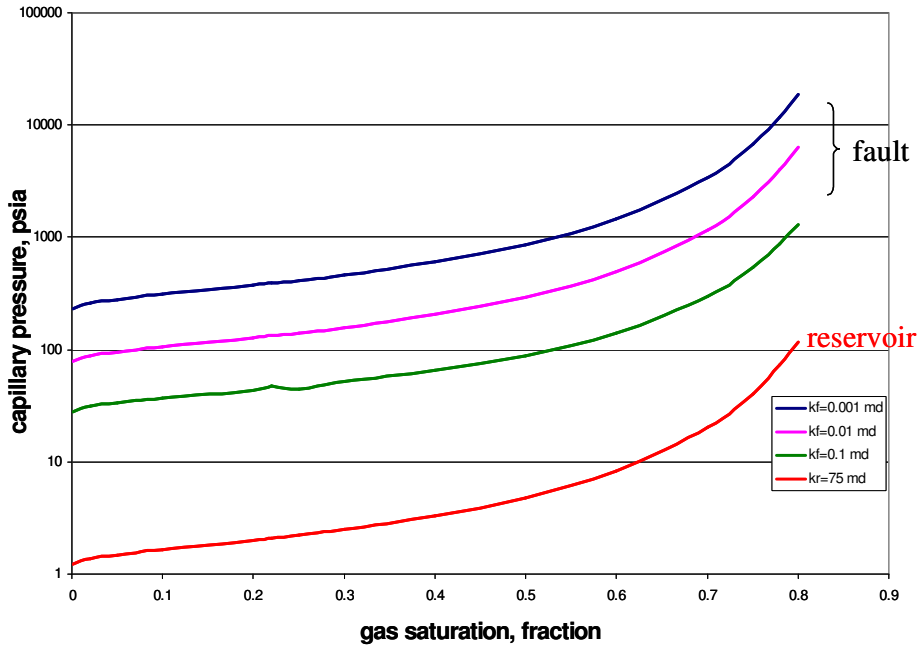

Figure 31. Capillary pressure curves for faults and reservoirs. The curves for faults are derived from formulas (4), (7), (8), and (9). The curve for the reservoirs is derived from formulas (7), (8), and (9).

RELATIVE PERMEABILITY MODEL

The numerical simulation deals with two-phase fluid flow in which relative permeability is described by the following formulas (Standing, 1978):

$$k_{rg} = k_{rg}^{0} S_g^{\,2} \left[1 - \left(\frac{1 - S_g - S_{iw}}{1 - S_{iw}} \right) \right]^{\left(1 + \frac{2}{\lambda}\right)} \qquad (10a)$$

$$k_{rw} = k_{rw}^{0}\left[\frac{1-S_g-S_{iw}}{1-S_{iw}}\right]^{\left(3+\frac{2}{\lambda}\right)} \tag{10b}$$

where, k_{rg} is gas (non-wetted phase) fractional relative permeability. k_{rw} is water (wetted phase) relative permeability. k^{o}_{rw} is effective water phase relative permeability. k^{o}_{rg} is effective gas phase relative permeability (Figure 32). S_{iw} is the irreducible water saturation that is taken to be 0.22, and λ is a function of F_g found by combining

$$\log P_c = \log P_d - \frac{\log\left(\frac{1-S_g-S_{iw}}{1-S_{iw}}\right)}{\lambda} \tag{11}$$

(Brooks & Corey, 1966)

and

$$\log P_c = \log P_d - \frac{F_g}{\ln S_g} \tag{12}$$

(Thomeer, 1960, 1983) to obtain

$$\lambda = \frac{1}{F_g}\left[\ln S_g \log\left(\frac{1-S_g-S_{iw}}{1-S_{iw}}\right)\right] \tag{13}$$

SIMULATION OF GAS SUPPLY ALONG FAULTS

The geological model in this simulation consists of the main reservoirs and the interbedded shales. In the initial stage of the simulation, the reservoirs are saturated with

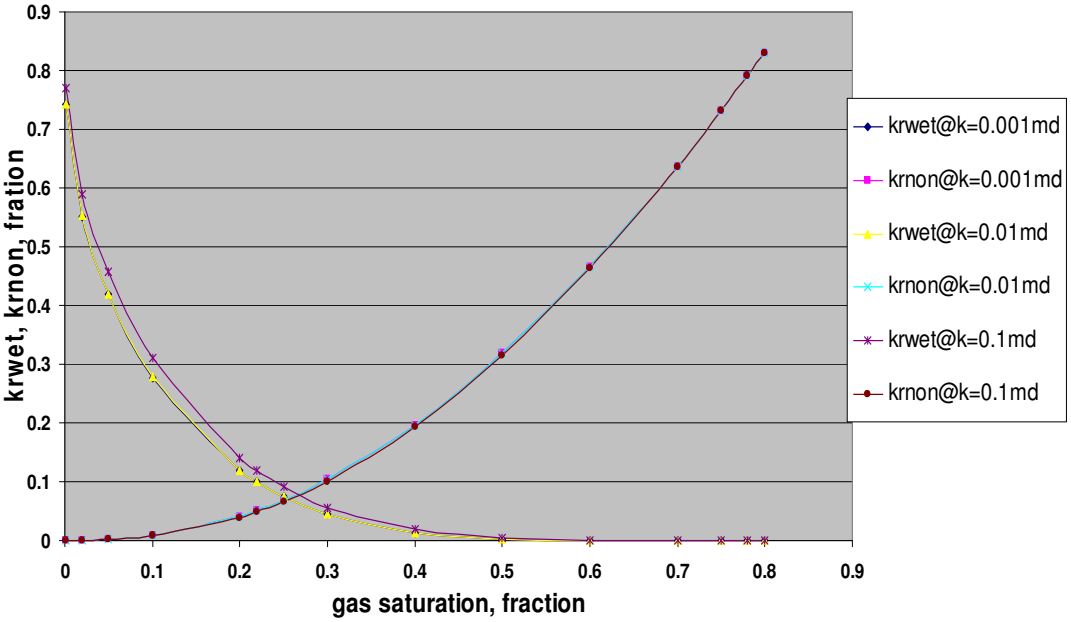

Figure 32. Relative permeability curves for faults. The curves were derived from equations (10a) and (10b).

formation water. Overpressure gas (dry gas) is injected by injection wells (referred as inputs) from the lowest portion of the faults to simulate gas supply. Other production wells (referred as outputs) in the upper portion of the fault or other faults in the model produce liquids to generate differential pressure, *dP* (*dP*= $P_{input} - P_{output}$), and outlets for the fluid flow.

RESERVOIR TEMPERATURE, FLUID PROPERTIES, AND ROCK COMPRESSIBILITY

Reservoir temperature

The bottom-hole-temperature (BHT) from three wells gives an average thermal gradient in Pabst Field of 1.96 ˚F /100ft (Table 4). The average depth of the Field is 10,324 ft. Thus, the reservoir temperature of the field is taken to be 202.6 ˚F.

Table 4. Formation temperature and thermal gradient of Pabst Field.

well	BHT(˚F)	depth (ft)	kb (ft)	gradient (˚F/100ft)
A5	202	10642	126	1.92
A3	207	10638	126	1.97
A4	210	10630	120	2.00
average				1.96

Gas density

Gas density is calculated from the following formulas (McCain, 1973):

$$\rho_g = M_a P_{sc} / R T_{sc} \quad (14)$$

$$M_a = \Sigma y_i M_i \quad (15)$$

where, ρ_g is the gas density, M_a is gas apparent molecular weight, y_i is the mole fraction of i^{th} component of the gas (data are from Sassen (2001)) and M_i is the molecular weight.

P_{sc} is pressure under the surface conditions, 14.7psia. R is a constant of value 10.73. T_{sc} is temperature under surface conditions, 520 ^{o}R.

The calculated gas density under the standard condition is 0.044 lb/cu ft.

Gas specific gravity

The gas specific gravity is given by

$$\gamma_g = M_a/29 \tag{16}$$

(McCain, 1973)

where, γ_g is gas specific gravity, fraction, Ma is taken to be16.97 lbm / lbm mol based on Sassen et al.'s (2001) data (lbm is pound mass and lbm mol is pound mol).

The gas specific gravity is taken to be 0.59.

Gas PVT data

Gas formation volume factor and gas viscosity are calculated from McCain's (1991) formula:

$$B_g = 0.00502(zT/P) \tag{17}$$

where, B_g is formation volume factor; z is gas compressibility factor; PV/mRT, P is pressure, psia; V is volume, ft^3; m is mass, lbm mol; and T is temperature, ^{o}F.

$$z=1+(A_1+A_2/T_{pr}+A_3/T_{pr}^3+A_4T_{pr}^4+A_5T_{pr}^5)\rho_{pr}+(A_6+A_7/T_{pr}+A_8/T_{pr}^2)\rho_{pr}^2-A_9(A_7/T_{pr}+A_8/T_{pr}^2)\rho_{pr}^5+A_{10}(1+A_{11}\rho_{pr}^2)(\rho_{pr}^2/T_{pr}^3)exp(-A_{11}\rho_{pr}^2) \tag{18}$$

where, A_1=0.3265, A_2= -1.0700, A_3= -0.5339, A_4=0.01569, A_5= -0.05165, A_6=0.5475, A_7= -0.7361, A_8=0.1844, A_9=0.1056, A_{10}=0.6134, A_{11}=0.7210.

$$\rho_{pr}=0.27[P_{pr}/(zT_{pr})] \quad (19)$$

$$T_{pr}=T/T_{pc} \quad (20a)$$

$$P_{pr}=P/P_{pc} \quad (20b)$$

$$T_{pc}=169.2+349.5\gamma_g-74.0\gamma_g^2 \quad (21a)$$

$$P_{pc}=765.8-131.0\gamma_g-3.6\gamma_g^2 \quad (21b)$$

where: ρ_{pr} is pseudoreduced density; T_{pr} is pseudoreduced temperature; P_{pr} is pseudo-reduced pressure; T_{pc} is pseudocritical temperature, °R; and P_{pc} is pseudocritical pressure, psia.

The gas viscosity is given by

$$\mu_g=A\exp(B\rho_g^{\,C})(10)^{-4} \quad (22)$$

where, μ_g is gas viscosity, cp; $A=(9.379+0.01607M_a)T^{1.5}/(209.2+19.26M_a+T)$;

$B=3.448+(986.4/T+0.01009M_a$; and $C=2.447-0.2224B$.

Water PVT data and water density

The water formation volume factor B_w, water compressibility c_w, $psia^{-1}$,and water viscosity μ_w, cp, are taken to have default value from Schlumberger (1998) listed in Table 5. The water density is taken to be the default value of 68.6708 lb/cuft from Schlumberger (1998)

Table 5. Formation water PVT data.

pressure, psia	B_w	c_w	μ_w
4000	1.029	3.03×10^{-6}	0.7588

Rock compressibility

For sandstone with 25% porosity, rock compressibility, c_f, is 3.3×10^{-6} psia $^{-1}$ (Hall, 1953). This value is assumed for the entire model, including shales, sands, and faults.

CHAPTER IV

TEST MODELS

Simplified geological models are required in numerical modeling in order to obtain reasonable computer run times. To examine the effects of the simplification on the gas migration and accumulation as well as sensitivity to other factors such as gas charge rate, I constructed a serious of one-dimensional and one and half-dimensional Test Models (TMs) that have simple geometry (Table 6). These models also help to understand fluid flow in reservoirs and faults and provide results that can be used to construct more complex models of Pabst Field. Hicks et al. (1998) simulated secondary gas migration along faults and into reservoirs in their models using simple geometry. Bai (2003) used simple geometric models for investigating hydrocarbon migration in faulted reservoirs.

Table 6. Test models and their roles

Model name	Code	f(x)	Test
1	TM1	$S_g(dV)$	Effect of grid size (dV) on gas saturation (S_g)
2	TM2	$S_g(T_f)$	Effect of fault thickness (T_f) on gas saturation (S_g)
3	TM3	$dP(R_c)$	Relation between charge rate (Rc) and differential pressure (dP)
4	TM4	$S_g(dP)$	Effect of differential pressure (dP) on gas saturation (S_g)
5	TM5	$dP(k_f)$	Gas supply style: effect of fault permeability (k_f) on deferential pressure (dP)

TEST MODEL 1 (GRID)

In grid model of Pabst Field, fault zones are represented by a single cell width, which ranges from 2 ft to 20 ft, as calculated by using equation (1) in Chapter III, whereas the

cell width of the adjacent reservoir in the grid model is about 600 ft (refer to "Principal Model (PM) Construction" in Chapter V, page 65). This means that the reservoir cell width is 30-300 times the fault cell width. If the large reservoir cell is divided, as usual, into several smaller cells to create a gradual change in thickness from reservoir cell to fault cell, the total number of cells of the grid model is necessarily larger. The increased number of cells in the model results in a dramatic increase of the computation time. Using cell size as a variable, two one-dimensional test models, TM1a and TM1b were constructed to examine the effect of cell-size gradation on calculated gas saturation S_g in reservoirs.

TM1a and TM1b consist of a left reservoir and a right reservoir with a vertical fault between them (Figure 33). TM1a and TM1b are assigned the same petrophysical properties and fluid properties used in modeling Pabst Field. Gas is injected into the left end and fluid is produced at the right end under a fixed differential pressure ($dP = P_{input} - P_{output}$).

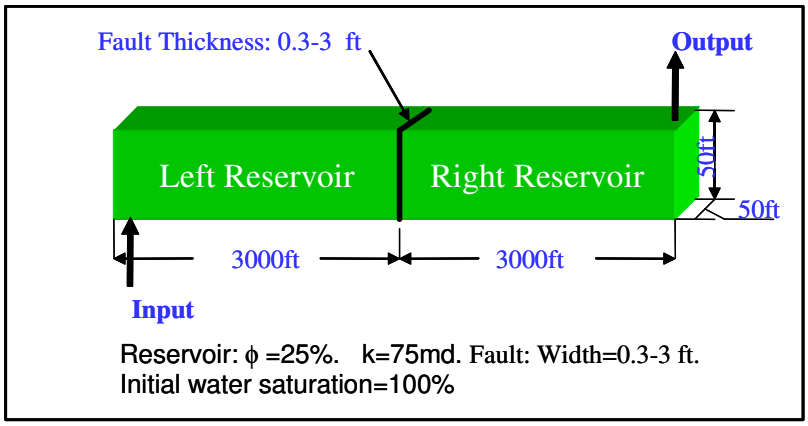

Figure 33. Geometry of TMs, testing effects of grid, fault thickness, and gas charge rate on gas migration and accumulation.

In TM1a, the thickness of the fault cell is 0.3 ft, and the cells in the both reservoirs have a uniform 90 ft. In TM1b, the thickness of the fault cell is 0.3 ft, but the thickness of the adjacent reservoir cells progressively increases from 5 to 90 ft with distance from the fault. To describe the effect of the cell size on gas saturation S_g, the relative difference of S_g of TM1 (RDS_gTM1) is defined by:

$$RDS_gTM1 = (S_{g1a} - S_{g1b})/S_{g1b} \tag{23}$$

where, S_{g1a} is average gas saturation in TM1a, S_{g1b} is average gas saturation in TM1b.

RDS_gTM1 is calculated for the left reservoir and the right reservoir, respectively. At an input rate of 6.5 MCFPD (dP=30 psia, constant), after 5 ky, RDS_gTM1 in the left reservoir is 1.9% and RDS_gTM1 in the right reservoir is 0.15%. After 30 ky, RDS_gTM1 in the left reservoir falls to 0.4% and RDS_gTM1 in the right reservoir falls to 0.23% (Figure 34). TM1 indicates that the effection of the abrupt change of cell size on gas saturation S_g is small for long geological times, which is most interest here.

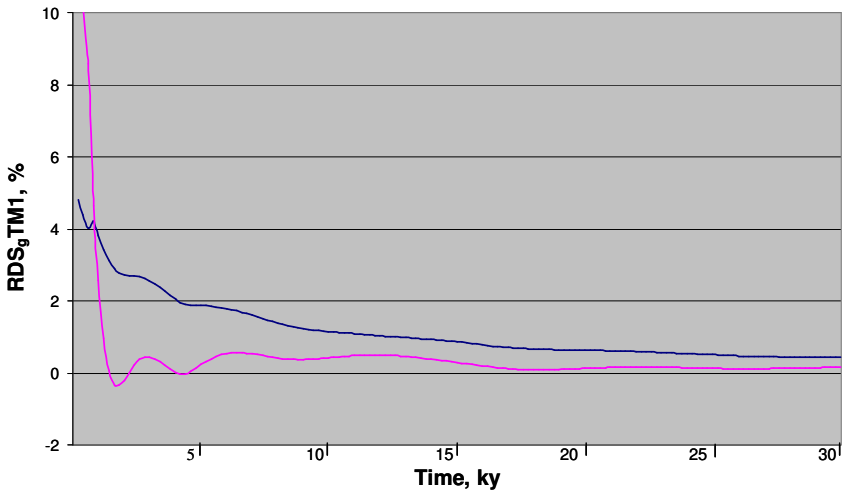

Figure 34. RDS_gTM1 vs. time. The black curve represents the RDS_gTM1 for the left reservoir and pink curve for the right reservoir. RDS_gTM1 for both reservoirs decreases and approaches a steady state with increasing time.

TEST MODEL 2 (FAULT THICKNESS)

In the model, faults are only a single cell thick and the fault thickness (T_f) is constant. There are two reasons for this. One is that constant T_f simplifies the grid model. Another is that the numerical models include only the portions of the fault segments that connect with the reservoirs. The fault segments above and below the reservoirs are outside the models. The distance from top to bottom of the sands is about 600 ft. Thus, only about 600 ft of any fault (some faults extend up to the sea floor and down into Mesozoic strata, more than 10,000 ft.) are included in the models. T_f itself may not vary too much in this interval. Moreover, T_f varies with fault throw, but faults that have same throw may have different thicknesses. T_f estimated from the throw (formula (1)) may be not accurate enough. Therefore, there are two possible causes of variation in T_f. One is that T_f varies along the fault itself; another is that faults with the same throw may have different T_f. Thus, I designed Test Model 2 (TM2) with same geometry, petrophysical properties, and fluid properties as the TM1 to estimate the effect of T_f on S_g in the left reservoir and the right reservoir. The variable of TM2 is T_f. Instead of 0.3 ft T_f in the TM2a, other TMs (TM2b, TM2c TM2d and TM2e) are given T_f ranging from 0.75 ft (2.5 times of TM2a) to 3 ft (10 times of TM2a). The relative difference of S_g of TM2 (RDS_gTM2) is defined by

$$RDS_gTM2=(S_g(T_f)-S_g(c_1))/S_g(c_1) \tag{24}$$

where, $S_g(T_f)$ is average gas saturation in reservoirs, and T_f has values of 0.75, 1.5, 2.25, 3 ft. $S_g(c_1)$ is average gas saturation reservoir at $T_f = c_1$, and c_1=0.3 ft.

RDS$_g$TM2 was calculated for the left reservoir and the right reservoir, respectively. As shown in Figure 35, *RDS$_g$TM2* of the left reservoir and the right reservoir are 1.1% and 1.4% respectively when T_f=0.75 ft. The models were run for 30 ky at an input rate of 6.5 CFPD (cubic feet per day). *RDS$_g$TM2* in left reservoir is 4.0% and *RDS$_g$TM2* in right reservoir is 4.2% as T_f=3.0 ft, that is 10 times 0.3 ft (T_f) in TM2a. *RDS$_g$TM2* increases with increasing fault thickness (T_f). It is understandable that with increasing T_f, the average permeability of the whole model will decrease because the faults have much lower permeability than the reservoirs. This results in a decrease in input rate.

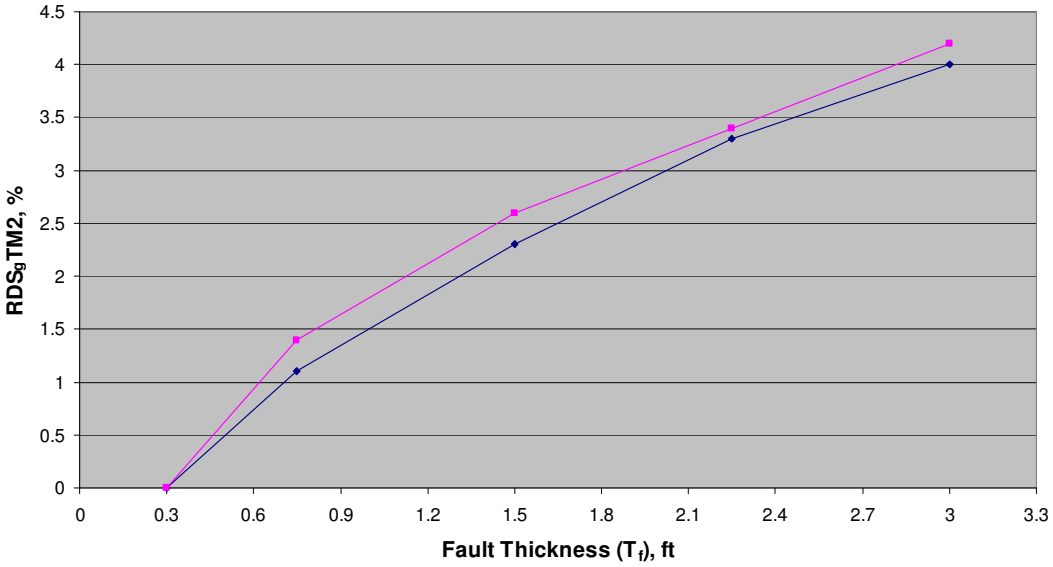

Figure 35. RDS$_g$TM2 vs. T$_f$ of TM2 at t=30 ky. The black and pink curves represent RDS$_g$TM2 for the left reservoir and the right reservoir, respectively. The RDS$_g$TM2 for both reservoirs increases with increasing fault thickness (T$_f$).

According to Ibanez's (2000) study, for the same throw, T_f varies less than one order of magnitude. TM2 indicates there is maximum 4.2 % change when T_f is increased by a factor of 10. However, relative to the large size of Pabst Field models, the faults occupy a very small portion of the total volume. Even though fault thickness varies greatly, the average permeability of the model does not change significantly. In addition, the variation of T_f for specific fault throw in Pabst Field may be not great as the variation of T_f in TM2. Thus, the change of T_f in the field model will be less a factor of 10. The assumption of constant T_f in the model does not have a significant effect on gas accumulation.

TEST MODEL 3 (CHARGE RATE)

The Eclipse® 100 modeling software has two options for gas input: constant differential pressure *dP* and constant input rate. Based on geological models of Pabst Field, gas input with constant differential pressure was chosen to model Pabst Field, as described in Chapter V. Gas charge time and charge rate are inversely related; the shorter the charge time, the greater the charge rate. Pabst Field has a short history with multiple charges (Sassen et al., 2001), so must have a high charge rate. Because I did not use the input rate directly, I constructed Test Model 3 (TM3) to examine the relationship between input rate and the differential pressure. TM3 has the same geometry, petrophysical properties, and fluid properties as TM1. The results of TM3 indicate a proportional relationship between *dP* and gas input rate (Figure 36).

Therefore, instead of testing the effect of input rate on S_g, I designed Test Model 4 (TM4s) as described in the following section to test the effect of dP on S_g.

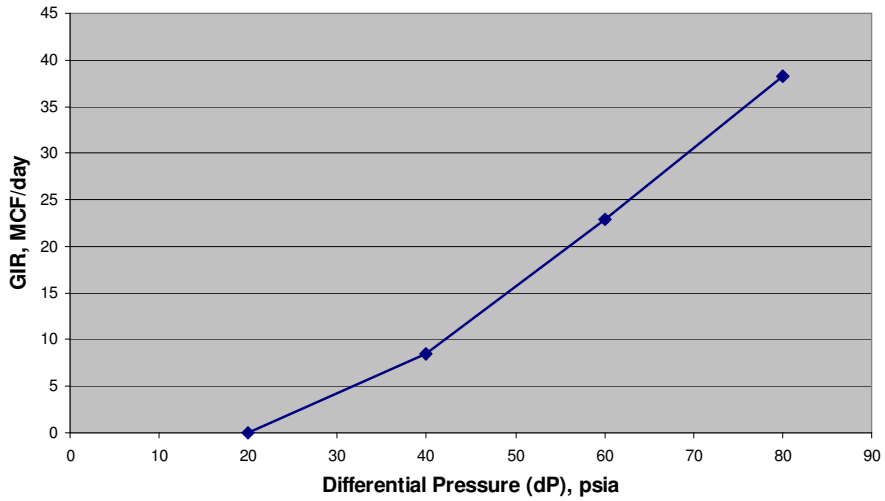

Figure 36. Gas input rate vs. differential pressure (dP), TM3 at t=30 ky. T_f=0.3 ft, constant. The variable of TM3 is dP. Gas input rate is directly proportional to dP. "GIR"= gas input rate.

TEST MODEL 4 (DIFFERENTIAL PRESSURE)

TM4 has the same geometry, petrophysical properties, and fluid properties as TM1. The variable is differential pressure dP. Based on S_g at dP=20 psia, the relative difference of S_g of TM4 (RDS_gTM4) is

$$RDS_gTM4=(S_g(dP) - S_g(c_2)) / S_g(c_2) \quad (25)$$

where, $S_g(dP)$ is average gas saturation in reservoirs, and dP has values of 40, 60, 80 psia. $S_g(c_2)$ is average gas saturation in reservoirs as $dP = c_2$, and c_2 = 20 psia.

RDS_gTM4 was calculated for the whole reservoir (the left reservoir plus the right reservoir). Correspondingly, the gas charge rate has a wide range from 0.003 CFPD (cubic feet per day) to 38.3 CFPD from TM3. The *RDS_gTM4* in the left reservoir varies from 6.5% to 13.7% (Figure 37). The greater the differential pressure, the higher the gas charge rate and gas saturation. This test indicates that the effect of the charge rate on S_g is significant; variations of *dP* may result in different migration pathways, or a different gas distribution in the field model.

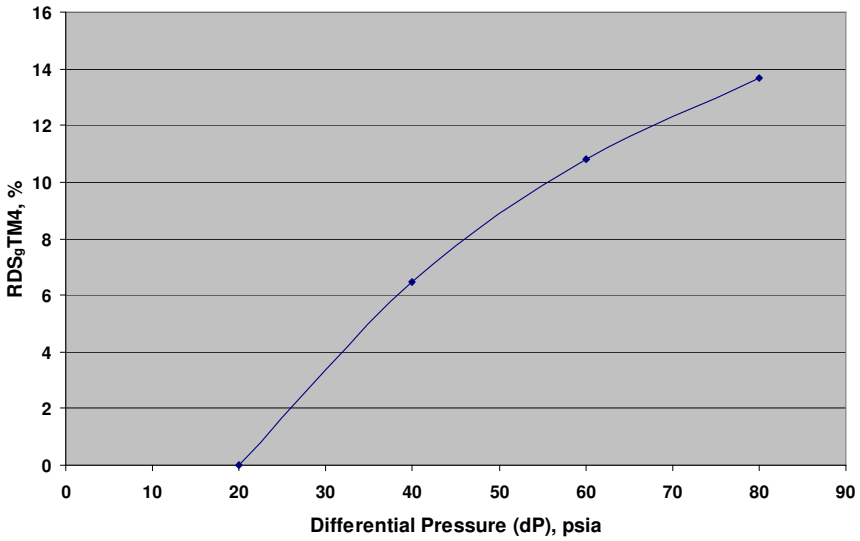

Figure 37. RDS_gTM4 vs. dP. The RDS_gTM4 for whole reservoir increases with increasing dP.

TEST MODEL 5 (GAS SUPPLY PATTERN)

Pabst Field has four large faults: F00, F01, F02 and F03 (their throw is over 250 ft, refer to Table 1). The three sands are confined by these faults that cut deeply into

Mesozoic source rock and transmit gas from the source rock into the reservoirs in the field. Fault F00 is a listric primary fault that has a lower dip angle at depth, while synthetic and antithetic faults F01, F02 and F03 have high dip angles. The effective normal stress across a surface determines permeability parallel to that surface. And the effective stress normal to the fault plane (NTFP) increases with decreasing dip angle for a specific pore pressure, assuming vertical principal stress is greater than horizontal principal stress. In general, higher NTFP effective stress reduces aperture of faults and pores, causing a decrease of permeability with depth along the listric fault (Watkins et al., 2001a). The permeability variation of the faults in Pabst Field should influence gas migration pathways.

To examine this hypothesis, I constructed Test Model 5 (TM5). Its geometry is a single horizontal layer of sand bounded by two vertical faults. In addition, two LTNVFs are located within the reservoir. The same differential pressures are set up at two charge faults. The permeability of the lower portion of the right fault is half (0.05 md) of the permeability of left fault (0.1 md) or the upper portion of the right fault (0.1 md). Gas with overpressure (1.8 times hydrostatic pressure) is injected at the bottom of each charge fault (Figure 38).

At the beginning of the test, gas are injected at INPT1 and INPT2, at an input rate of 1100 CFPD and 500 CFPD, respectively (Figure 39), and gas input stops at 24 ky because the pressure in the model increases so that the pressures in the inputs are equal to the pressures in the surrounding reservoirs (this occurs because the input rate is high). Only a small amount of water is produced from the model until 100 ky when the INPT1

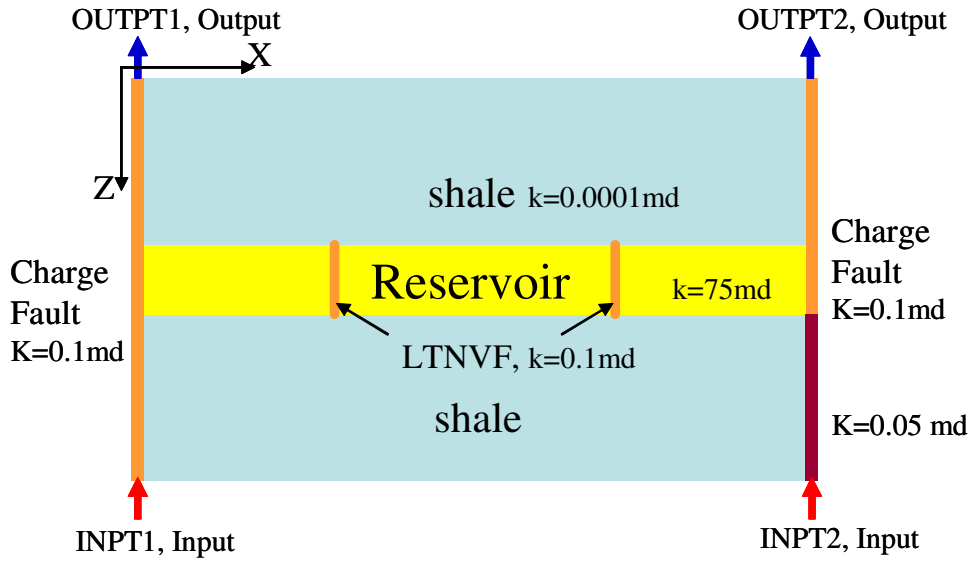

Figure 38. Basic geometry and petrophysical properties of TM5. The model consists of a reservoir interbedded within shale and bounded by two faults. Two Inputs (INPT1, 2) and two Outputs (OUTPT1, 2) are located at the tops and bottoms of the faults to simulate gas migration along the faults. The properties of the left fault are uniform to represent a high angle antithetic fault. The properties of the right fault vary to represent a primary fault. Two LTNVFs are located in the reservoir. (Not to scale.)

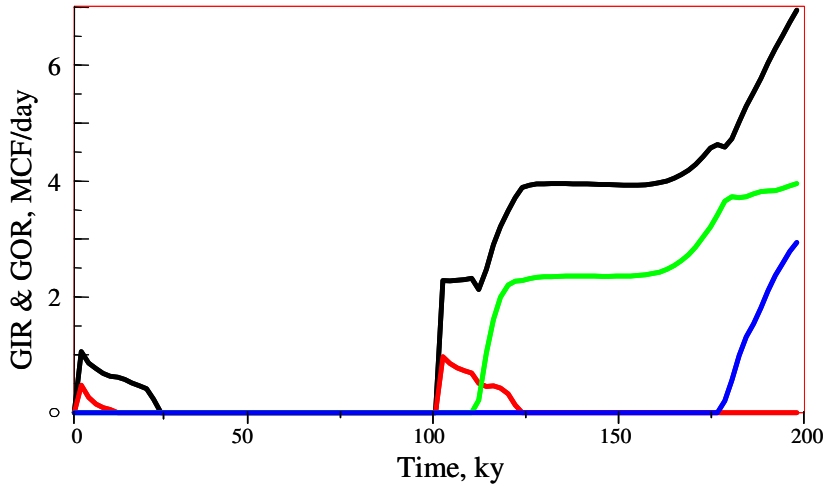

Figure 39. GIR & GOR vs. time of TM5. "GIR"=gas input rate. "GOR"=gas output rate. Black is GIR of INPT1. Red is GIR of INPT2. Green is GOR of OUTPT1, and Blue is GOR of OUTPT2.

and INPT2 begin to inject gas again. At 110 ky, OUTPT1 produces gas. Gas input at INPT2 stops again at 122 ky when the two end portions of the reservoir are charged with gas (Figures 40, 41). OUTPT 2 produces gas at 178 ky. At this point the reservoir is charged with gas only by INPT1, but both OUTPT1 and OUTPT2 produce gas. During this time the left fault acts as charge fault and the right fault acts an outlet for fluid flow.

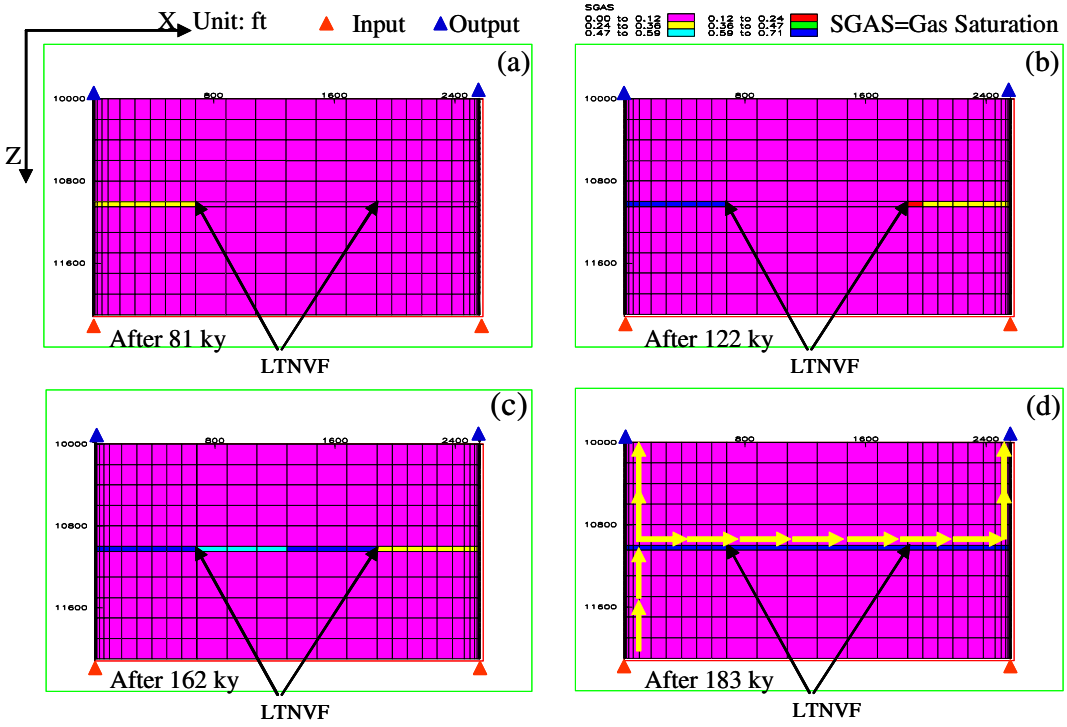

Figure 40. Gas saturation profiles of TM5. (a) After 81 ky of gas input along the charge faults, gas charges the reservoir (sixth row of the cells) from the left and is stopped by the left LTNVF (refer to Figure 38 for the positions of reservoir and the LTNVFs). (b) After 122 ky, gas continues to charge the reservoir from the left and gas also charges the reservoir from the right. (c) Gas migrates from left to right and is stopped by the right LTNVF. (d) Gas breaches the right LTNVF and migrates through the reservoir from left to right and finally escapes along the right charge fault. The yellow arrows illustrate gas flow in the faults and the reservoir.

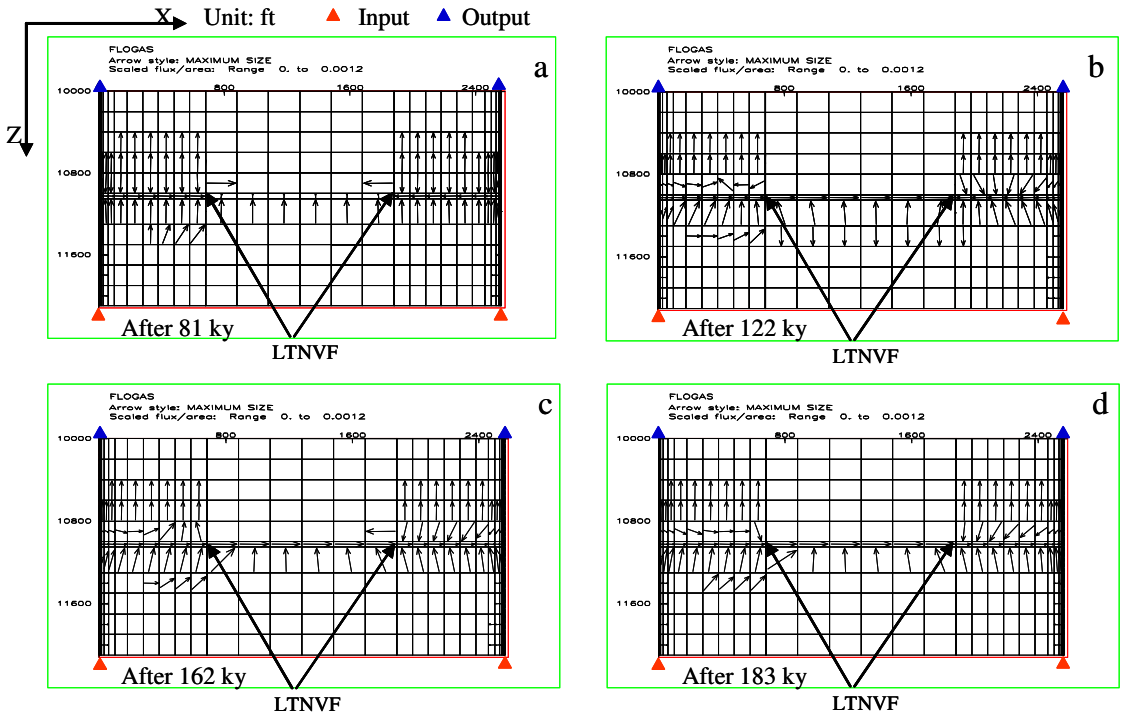

Figure 41. Gas flow profiles of TM5, showing the same process as shown in Figure 40. FLOGAS= gas flow. The arrows within cells represent the direction of gas flow. The sixth row of the grid is the reservoir. Refer to Figure 36 for the positions of reservoir and the LTNVFs. (a) gas flow into the reservoir from its two ends. (b) Gas flow is dominantly to the right. (c) Gas flow in the reservoir is to the right. (d) Gas flows through the reservoir from left to right and finally escapes along the right charge

TM5 demonstrates that a differential pressure of 36 psia is built up between the ends of the sand reservoir. The differential pressure drives gas through the sand reservoir from the left end to the right end through two interior LTNVFs, and the gas eventually escapes along the upper portion of the right fault (Figures 40, 41).

The processes of gas migration in TM5 are complex. The grid model of Pabst Field described in Chapter V includes the three sand reservoirs, interbedded shales, faults

within the field, and bounding faults, but does not include the strata that lie above and below the three sand reservoirs. Thus, the Pabst Field model is not able to simulate the processes that occur in TM5. Variations of pressure at different faults drive gas to migrate in various pathways; some faults will be inlets for fluid and some faults will be outlets. In TM5, the left fault with high permeability acts as the inlet for fluid, while the right fault with lower permeability at depth acts as an outlet.

CHAPTER V

PABST FIELD MODELING

As previously indicated, the purpose of this study is to develop an understanding of gas migration in Pabst Field. Taking into account the interaction of multiple reservoirs crossing variable permeability faults, Pabst Field may have a complex history of gas migration and accumulation at the reservoir scale. A principal model (PM) based on the previous models described in Chapter III and the Test Models (TMs) described in Chapter IV was constructed to simulate the gas charge process of Pabst Field. More complex geological processes were considered and added to the PM to develop an Advanced Model (AM) that more closely matches the gas accumulation in the real world (Table 7). Because this study is the first attempt to simulate a real field at a reservoir scale, it makes sense to simplify the models, for example, by treating the reservoir sands, shales and faults as homogeneous.

The initial geometrical model of fault location and reservoirs and shale bodies is nearly identical to the geometry of final model. Only minor changes of final model were made to provide better matches with reservoir data. Hundreds of trials were conducted by adjusting fault properties and changing boundary condition in term of the numbers and locations of inputs and outputs, input rates, and the sequence of inputs to match the distributions of gas obtained from the model to the gas distribution observed from the seismic data. The fault permeability for the trials ranges from 0.001 md to 10 md based on the data list in Table 3. The input rate is adjusted by changing input/output pressures,

which range from 2 % to 20 % higher/lower than hydrostatic pressure. The PM and AM described this Chapter are the most successful models of hundreds of trials.

Table 7. Pabst Field models and their roles.

Model name	Code	Test
Principal model	PM	Pabst Field models, modify fault properties and gas supply style and rate
Advanced model	AM	Add more sophisticated geological process in the field modeling to improve charge time and gas distribution

PRINCIPAL MODEL (PM) CONSTRUCTION

Pabst Field contains three sand reservoirs that are interbedded with two shales. The model resembles a version of a McDonald's Big Mac in which three layers of bread (reservoirs) are separated by two meats (shales). The grid was constructed using hexahedral cells whose shapes accommodate fault orientation (Figures 42, 43, 44). The cells are as small as possible for reasonable computer run time. For example, the size of a reservoir is typically 600'X500'X50' ($15X10^6$) cubic feet. While keeping the one-layer structure of the shale, each sand is divided into 3 cell layers. The total number of cells in the model is 28215 (57X45X11, including inactive cells). Fault cells are much smaller than those used for sand and shale layers. The thickness of faults ranges from 2 to 20 ft. Petrophysical parameters and fluid properties are defined for each cell. To save computer time, cells representing the shales are defined as inactive cells if the cells are not bounded by sand cells.

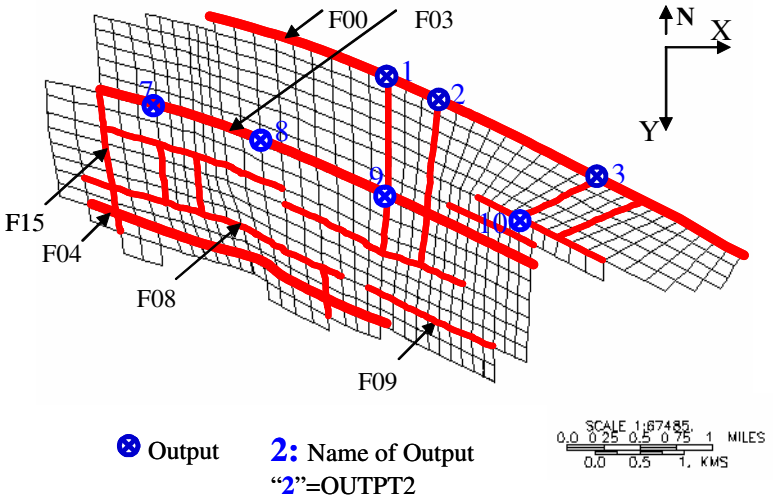

Figure 42. Grid of 10,000' sand and gas charge pattern. Grids and gas charge pattern for top of the sand and bottom of the sand are same. The numbers represent the names of the outputs. F# represents fault name. The bold red lines represent faults. However, the fault thickness is too thin (2-20ft) to be visible. Therefore the line width does not indicate the fault thickness in this and following figures.

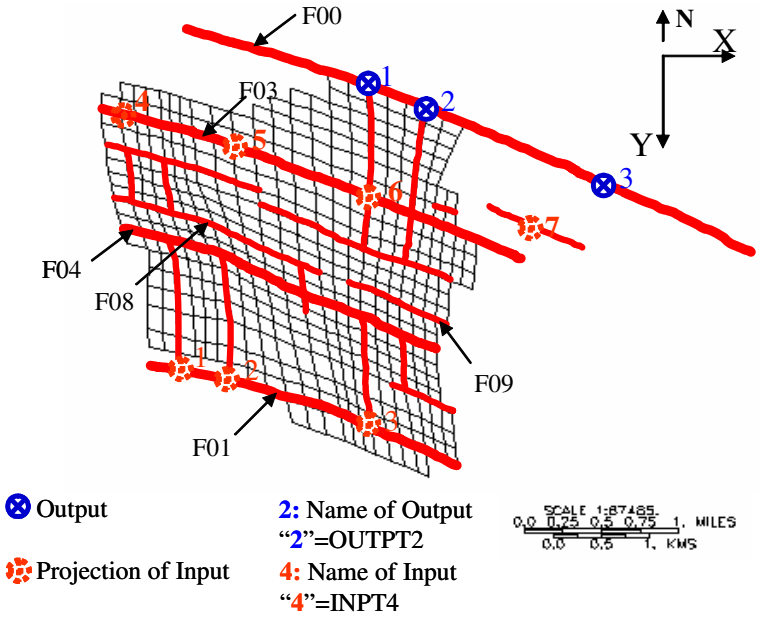

Figure 43. Grid of 10,150' sand and gas charge pattern. Grids and gas charge pattern for top of the sand and bottom of the sand are same. The bold red lines represent faults. The numbers represent the names of the outputs and inputs. F# represents fault name.

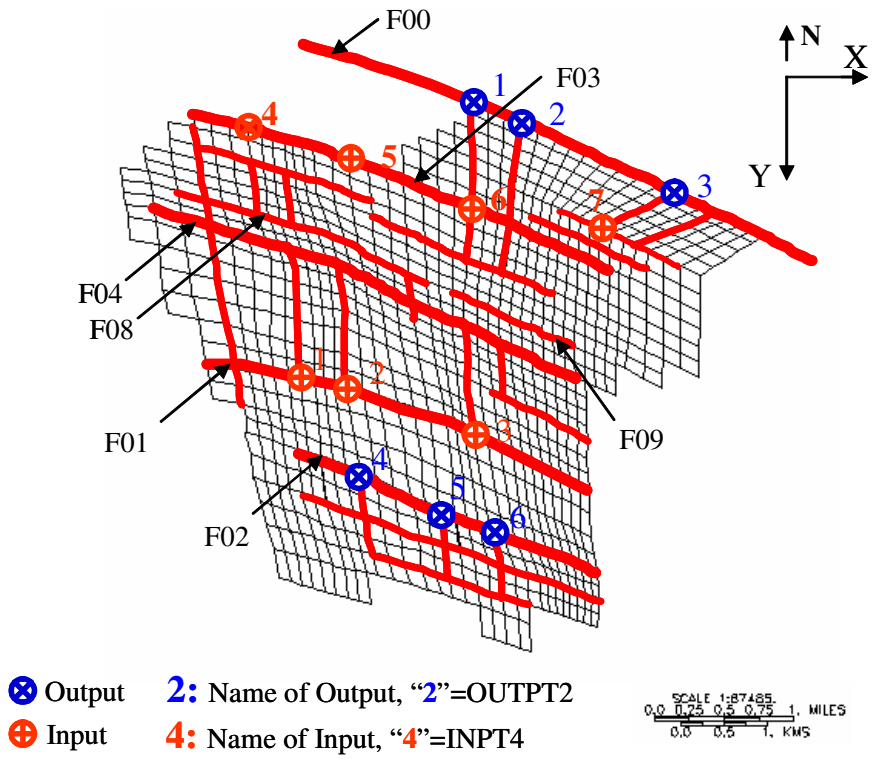

Figure 44. Grid of 10,300' sand and gas charge pattern. Grids and gas charge pattern for top of the sand and bottom of the sand are same. The bold red lines represent faults. The numbers represent the names of the outputs and inputs. F# represents fault name.

According to Test Model 5 (TM5), between the two fault-bounded ends of the sand reservoir, a pressure difference is built up and drives gas flow through the faulted sand reservoir if there is a permeability difference between the faults at depth. The principal model (PM) is constructed in this way: fault F01 and fault F03 are gas supply faults, and faults F00, F02 and F03 are fluid output faults in which pressure differences drive gas to charge the reservoirs. Movement of gas in the reservoirs has multiple pathways.

Vertical gas migration tends to be very fast (England et al., 1987). Gas rises along a fault until the fault cuts a thick shale horizon where the shear zone permeability become very low, which impedes continual upward flow of gas. In the PM, the lower portion of fault F03 is an inlet and the upper portion of fault F03 is an outlet. For gas supply fault F01, the upper portion of fault F01 is sealed and the lower portion is an inlet for gas input. The faults F00 and F02 are outlets for gas output. As a result, differential pressures build up directly in the reservoirs, instead of along the faults as in TM5. This simplifies the modeling process, and allows adjusting the gas charge pattern and charge rate easily. Moreover, it allows most gas to enter the reservoir rather than to escape directly from the upper ends of the faults.

The PM has 7 vertical injection wells (referred as inputs) and 10 vertical production wells (referred as outputs). It is important to point out that this is a multi-point gas supply style. Most of the inputs/outputs are put at the intersections of gas supply faults in fault Family 1 and cross faults in fault Family 2.

At the beginning of the simulation, Input 1 (INPT1), Input 2 (INPT2) and Input 3 (INPT3) inject gas at a pressure 5% higher than the hydrostatic pressure along fault F01. Meanwhile, Output 1 (OUTPT1), Output 2 (OUTPT2), and Output 3 (OUTPT3) produce liquid at a pressure 5% lower than the hydrostatic pressure along fault F00; Output 4 (OUTPT4), Output 5 (OUTPT5), and Output 6 (OUTPT6) produce liquid at a pressure 5% lower than the hydrostatic along fault F02. After 20 ky, Input 4 (INPT4), Input 5 (INPT5), and Input 6 (INPT6), start to inject gas at a pressure 10% higher than the hydrostatic along fault F03. Meanwhile, Output 7 (OUTPT7), Output 8 (OUTPT8), and

Output 9 (OUTPT9) produce liquid at a pressure 5% lower than the hydrostatic pressure along fault F03. After 60 ky, Input 7 (INPT7) begins to inject gas at a pressure 10% higher than hydrostatic pressure at the intersection of faults F06 and F29, and Output 10 (OUTPT10) is set at the intersection of faults F06 and F29 to produce liquid (Figures 42, 43, 44, 45).

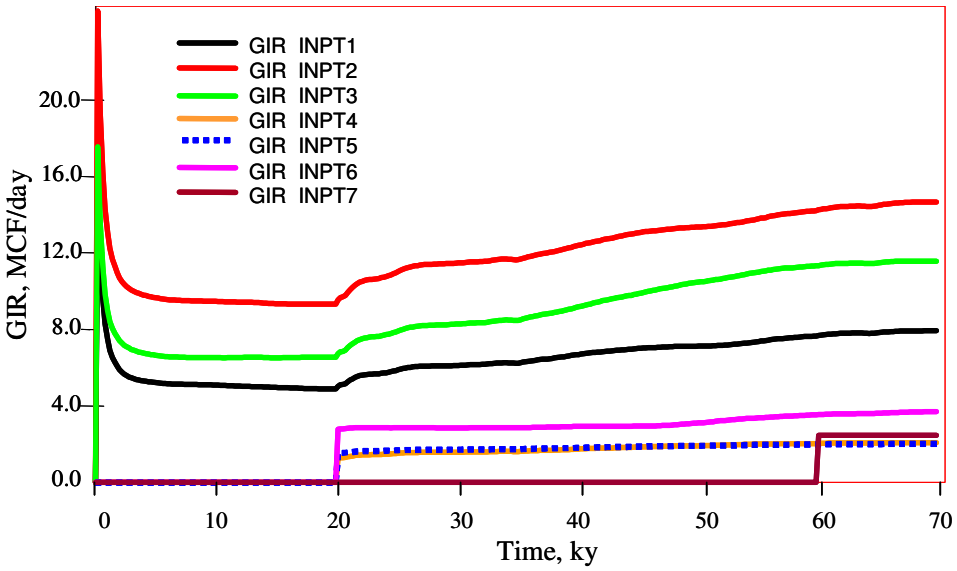

Figure 45. Gas input rate vs. time of PM. INPT1, 2, 3 charge the reservoirs first. After 20 ky, INPT4, 5, 6 start to charge. After 60 ky, INPT7 start to charge. INPT1-7 represents the inputs; "GIR" = "gas input rate" that is controlled by dP.

THE RESULTS OF PM

Outputs from the PM run are gas saturation, pressure, and gas flow (Figures 46-50). The geological duration of PM is 270 ky (1 ky =1,000 years). During the first 20 ky,

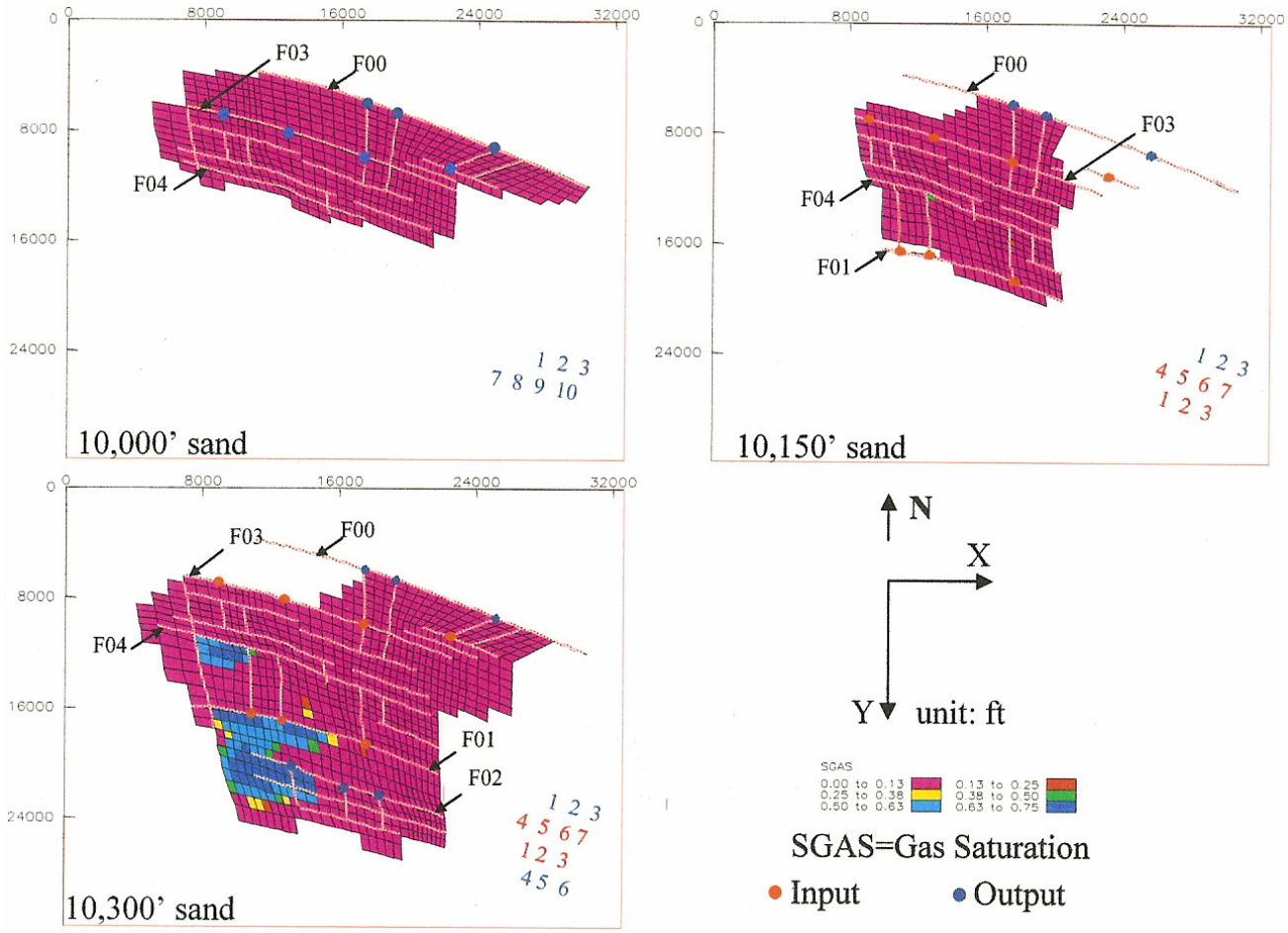

Figure 46. Gas charge of three sands after 10 ky. 10,300' sand: gas charges the reservoir sands in both hanging wall and foot wall of fault F02. Some gas is sealed by fault F04. 10,150' sand: a small amount of gas is stopped by fault F04. 10,000' sand: not charged yet. The numbers in the lower right corners represent the names of inputs (red) and outputs (blue).

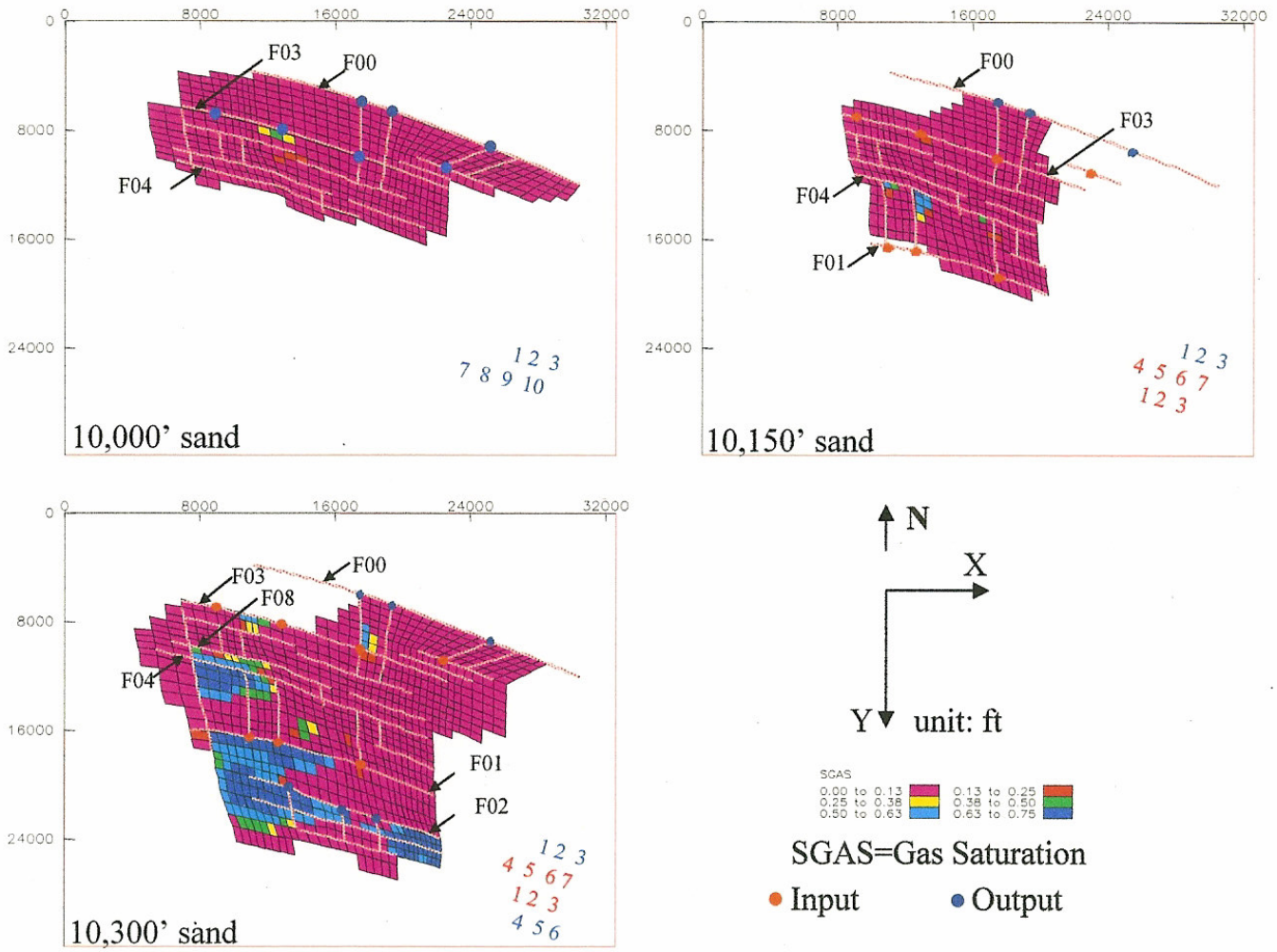

Figure 47. Gas charge of three sands after 22 ky. 10,300' sand: gas breaks fault F04 and charges northern part of the field. 10,150' and 10,000' sands: charged with some gas along fault F04 and fault F03. The numbers in the lower right corners represent the names of inputs (red) and outputs (blue).

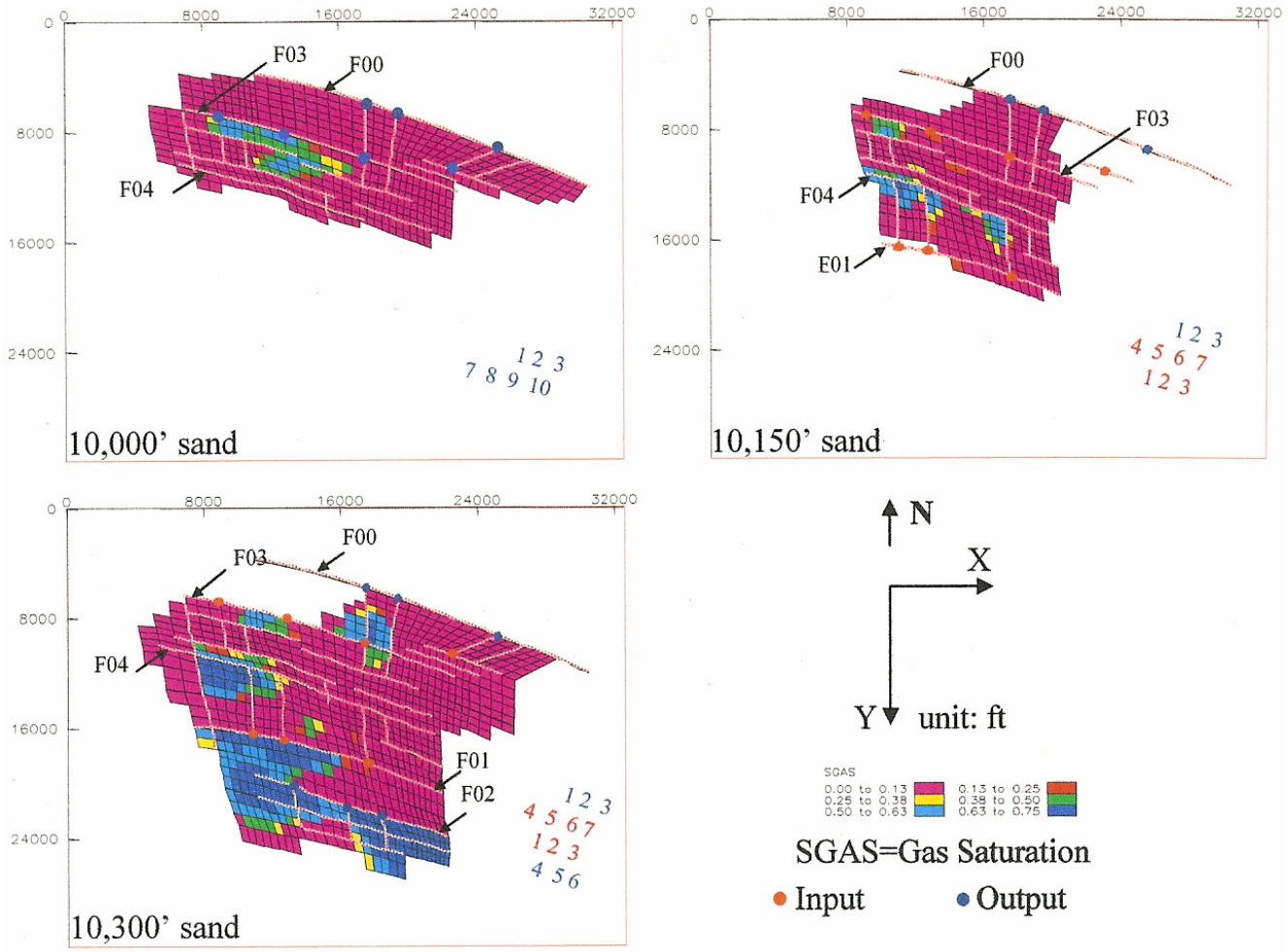

Figure 48. Gas charge of three sands after 34 ky. 10,300' sand: gas charges mainly north part of the field. 10,150' sand: large amount of gas charge along faults F03 and F04. 10,000' sand: fault F03 traps much gas. The numbers in the lower right corners represent the names of inputs (red) and outputs (blue).

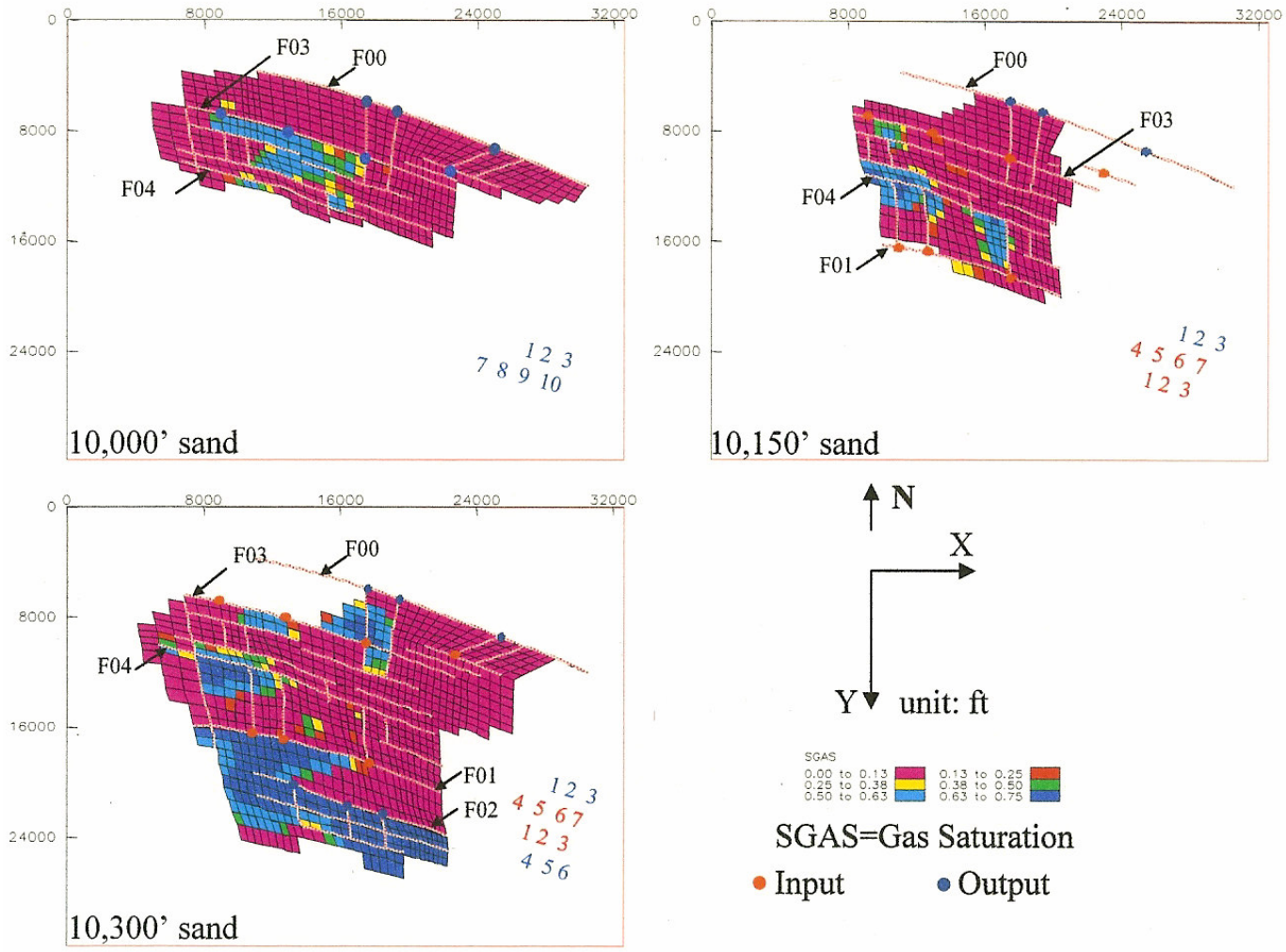

Figure 49. Gas charge of three sands after 46 ky. 10,300' sand: little gas is added. 10,150' sand: much gas is charged between fault F01 and fault F04. 10,000' sand: gas continues to charge the compartments to the south of fault F03. The numbers in the lower right corners represent the names of inputs (red) and outputs (blue).

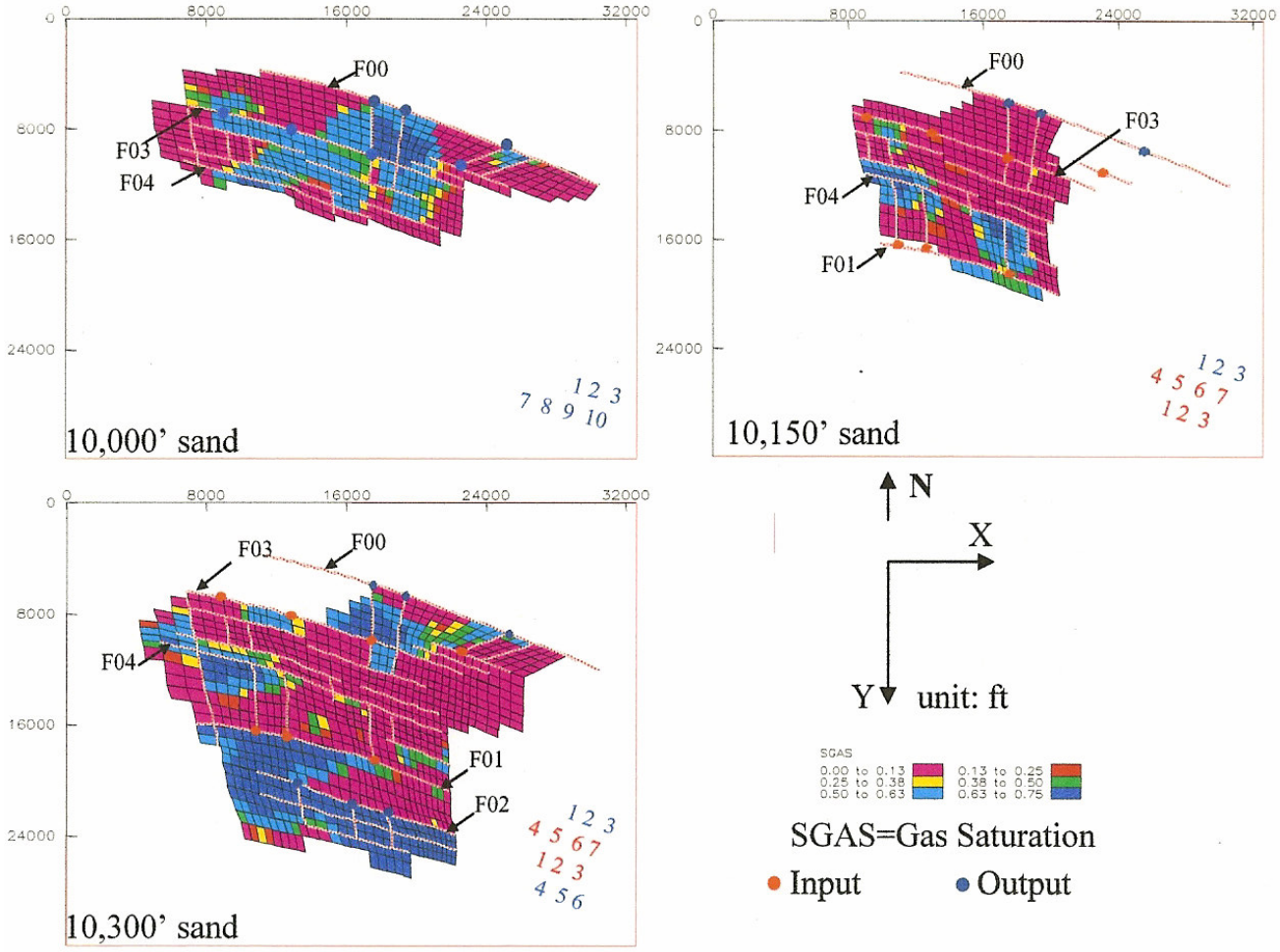

Figure 50. Gas charge of three sands after 70 ky. The 10, 000' sand is fully charged with gas after the 10,150' sand and the 10,300' sand are saturated with gas. The numbers in the lower right corners represent the names of inputs (red) and outputs (blue).

only fault F01 provides gas to reservoirs, then fault F03 supplies gas for 40 ky. Following that, INPT7 inputs gas for 10 ky. Finally, the fault permeability in the model is changed from 0.1 md to 0.001 md to keep the reservoirs at state of equilibrium for 200 ky. The average rate of gas supply to the reservoirs along fault F01 is 27.4 MCFPD (thousand cubic feet per day). Along fault F03, the average rate is 6.8 MCFPD, and the rate for INPT7 is 2.5 MCFPD. The total average gas charge rate for the whole field is 33 MCFPD. The total volume of injected gas is 834 BCF (1 BCF=10^9 cubic feet). The volume of gas that escaped along the faults is 235 BCF. Most of the gas escapes along fault F03. The field traps 598 BCF of gas, which is 72% of the total input gas. The 10,300' sand traps 392 BCF, the 10,150' sand traps 64 BCF, and the 10,000' sand traps 142 BCF.

Fault F00 and fault F02 act as migration pathways. Fault F01 and fault F03 act as both migration pathways and baffles. The cross faults act mainly as baffles. For best match of modeling and observed gas distribution, the permeability of faults is 0.1 md and porosity of faults is 10 % when the faults act as a migration pathway. In contrast, the permeability of faults is 0.001 md and porosity of faults is 6 % when the faults are not conduits and gas supply ends.

COMPARISON WITH FIELD DATA

To verify the PM, I compared the pressure and the gas distribution from the PM with that from seismic amplitude anomalies that have been verified by well data. Here I refer to the gas distribution from seismic amplitude anomalies as "seismic gas distribution"

that is used for the comparison, while the gas distribution from the model is the "model gas distribution". This comparison is qualitative. For example, the thicknesses of the gas layers are not compared, because the thicknesses of the gas layers determined by modeling could be over-estimated owing to the large grid size. The seismic model is constrained by well data, while the model gas distribution is defined by gas saturation greater than 0.4. The gas distribution based on the net pay map of the 10,300' sand in the southern area of the field approximately agrees with the model gas distribution.

Pressure

Formation pressures derived from the model (Figures 51) can be compared to primary formation pressures of the 10,300' gas layer estimated from well test data. For example, the primary formation pressure in well A4 is 4796 psia, whereas model pressure is 4837 psia. The pressure of the 10,300' gas layer in well 9 is 4992 psia, while the model pressure is 5015 psia. The relative errors are 0.9 % and 0.5%, respectively.

Gas distribution

There are 45 compartments in the three sands: 14 compartments in the 10,000' sand, 9 compartments in the 10,150' sand, and 22 in the 10,300' sand. There is good agreement between the seismic gas distribution and model gas distribution for 84% of the reservoir compartments. This result indicates that PM is adequate but needs improvement (Figures 52, 53, 54).

In the 10,300' sand, model gas distribution matches seismic gas distribution in all of

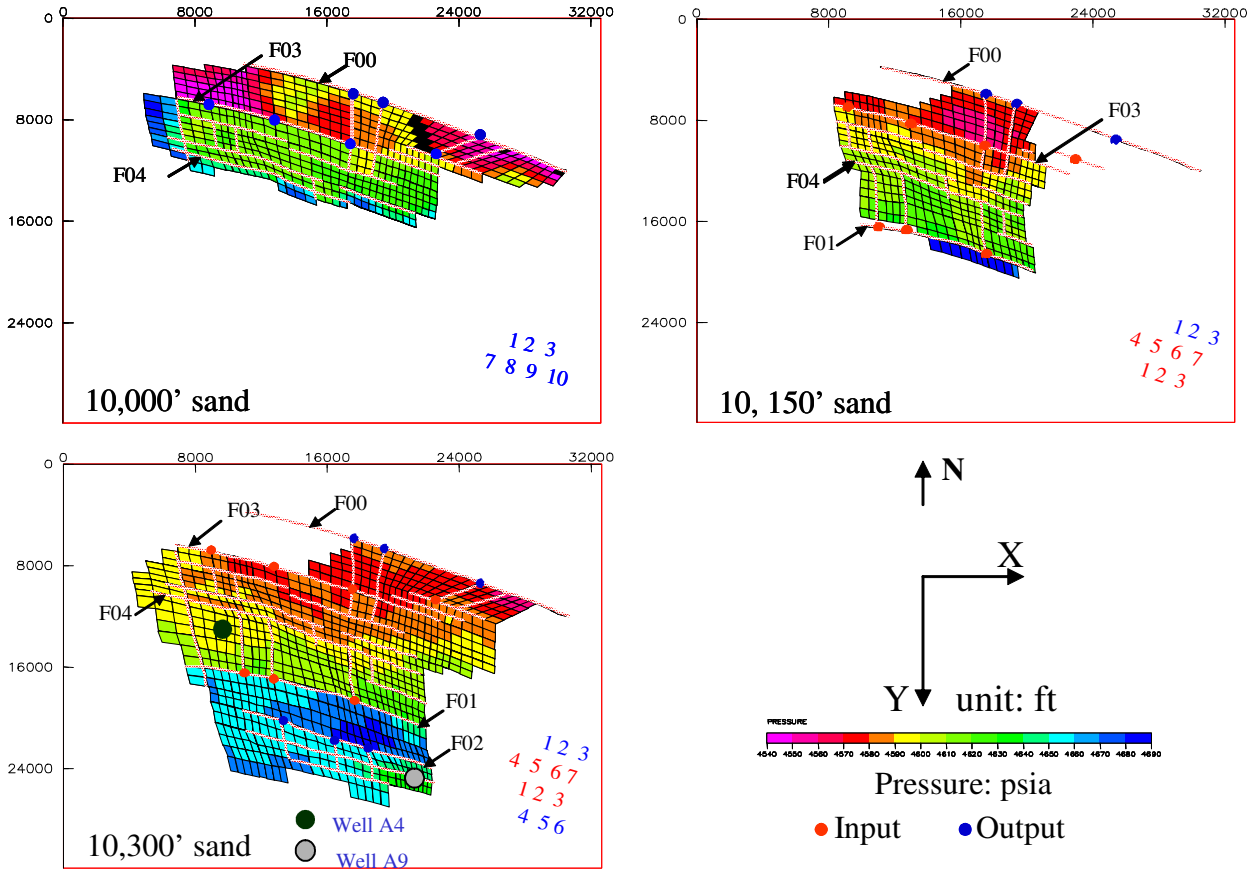

Figure 51. PM formation pressure of three sands after 270 ky. Formation pressure was adjusted by buoyancy and gravity separation and achieved equilibrium 200 ky after all faults were closed. The numbers in the lower right corners represent the names of inputs (red) and outputs (blue).

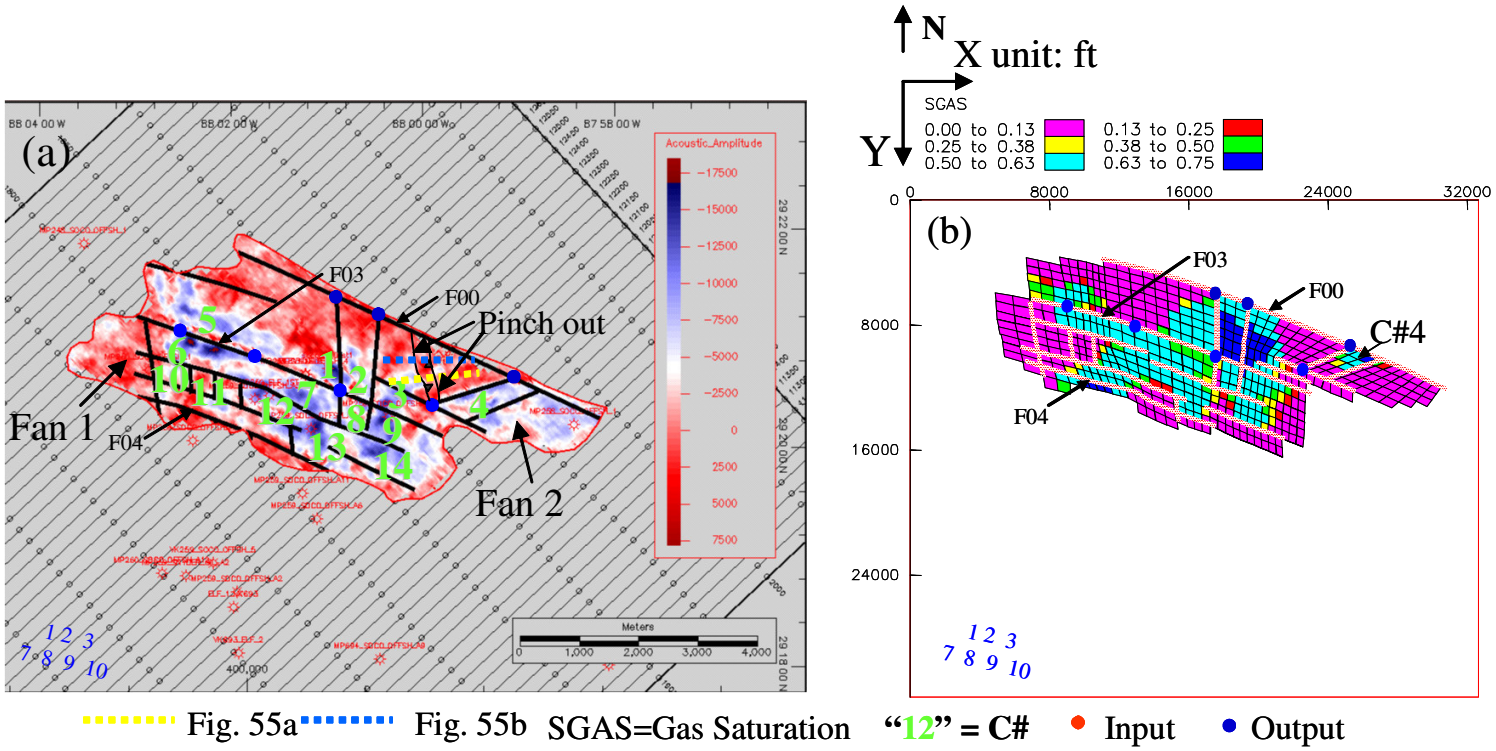

Figure 52. Comparison of seismic gas distribution of the 10,000' sand with PM. (a) Seismic amplitude anomaly (blue) represents gas distribution. An alternative interpretation for the 10,000' sand is that the sand consists of two fan bodies: fan 1and fan 2. The green numbers are compartment number. (b) Gas distribution is indicated by colors shown in color bars. The blue numbers in the lower left corner represent the names of outputs.

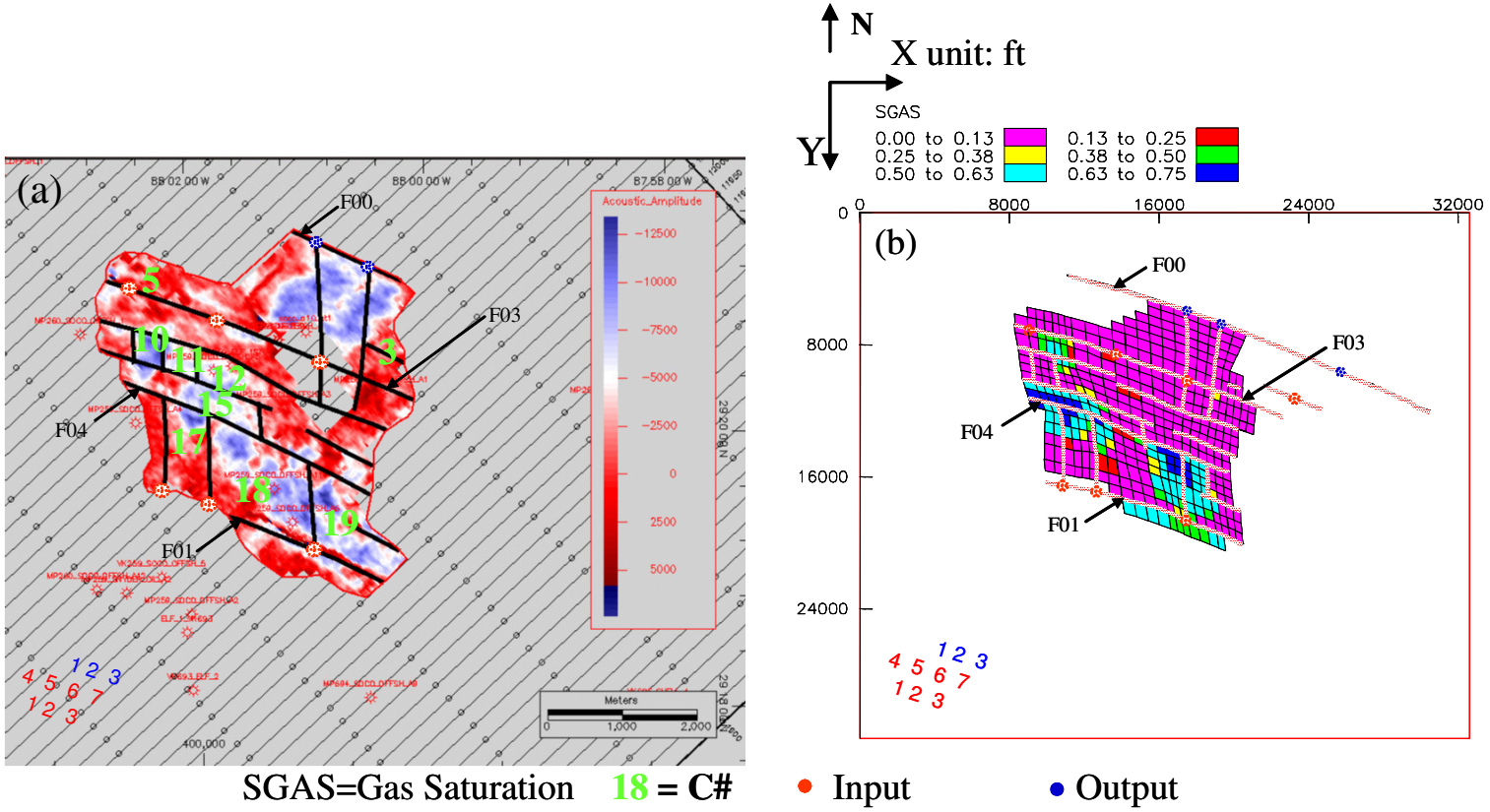

Figure 53. Comparison of seismic gas distribution of the 10,150' sand with PM. (a) Seismic amplitude anomaly (blue) represents gas distribution. The green numbers are compartment number. (b) Gas distribution is indicated by colors shown in color bars. The red numbers and blue numbers in the left right corners represent the names of inputs and outputs, respectively.

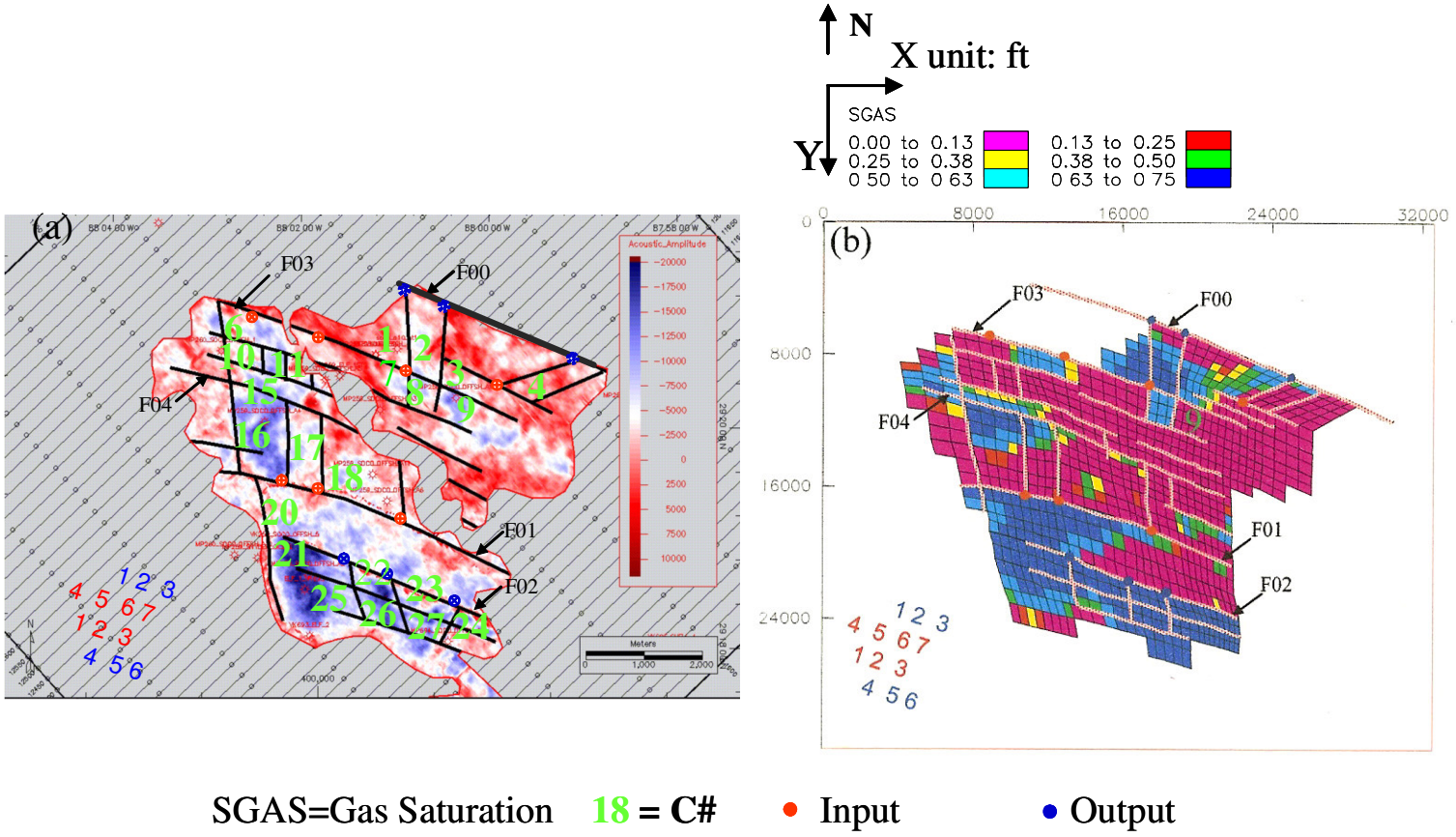

Figure 54. Comparison of seismic gas distribution of the 10,300' sand with PM. (a) Seismic amplitude anomaly (blue) represents gas distribution. The green numbers are compartment number. (b) Gas distribution is indicated by colors shown in color bars. The red numbers and blue numbers in the lower left corners represent the names of inputs and outputs, respectively.

the compartments except those located north of the "skylight window" (e.g. C#1, 2, 3, and C#7, 9). In the model, a large amount of gas is accumulated in C# 20 (the graben), where the area of gas accumulation is probably overestimated. In the 10,150' sand, all compartments match except C#10 and the compartments located north of the "skylight window" (e. g. C# 3). In the 10,000' sand, all 14 compartments match.

There are two ways in which the model does not match the seismic data. One is that seismic data indicate water but the model indicates gas (e. g. C# 1, 2 in 10,300' sand). Another is that seismic data indicate gas but the model indicates water (e. g. C#10 in 10,150' sand). The reason that the seismic anomaly indicates water but the model indicates gas is probably that the real reservoir is too thin or heterogeneous. The limitation in seismic resolution reduces the absolute value of the anomalies even though the sands contain some gas. Another problem is that, according to the seismic anomaly, gas distribution in some compartments is not uniform.

The reason may be that reservoirs are heterogeneous, while they are assumed homogeneous in the model. In some portions of the reservoir, thickness, porosity, and permeability are probably overestimated. Moreover, variations in reservoir geometry, such as pinch-outs, may cause the gas migration pathway to change. One example is C#4 in the 10,000' sand (Figure 52a). The strong seismic anomaly associated with C#4 indicates that it is a gas-charged compartment. Numerous trials, with different fault properties, fault locations, input locations and input rates, failed to result in a gas distribution in C#4 as that agrees with the seismic gas distribution. After reviewing the sand shape of 10,000' sand and seismic data, I suspect that there is a gap between C #3

and C # 4. Thus, the 10,000' sand likely consists of two sand bodies with fan shapes (Figure 52 (a)). Re-interpretation of seismic data agrees with possible pinch-outs in 10,000' sand at this location (Figure 55). Adding the pinch-outs to the 10,000' sand causes C#4 to be charged with gas (Figure 52b).

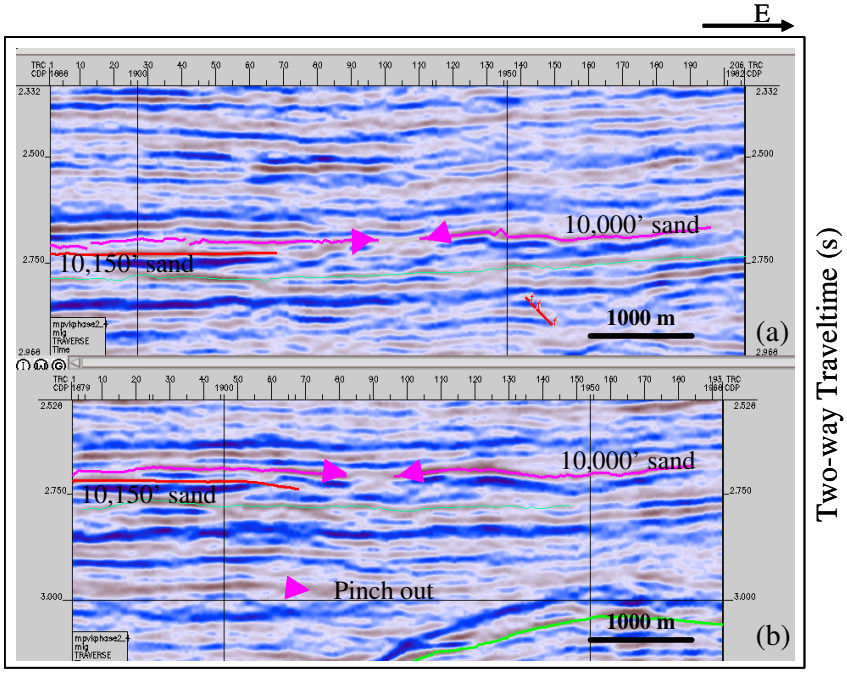

Figure 55. Seismic profiles, showing the pinch-outs of 10,000' sand. Locations are shown in Figure 52. The pinch-outs separate the 10,000' sand into two sand bodies.

GAS CHARGE PROCESS OF PABST FIELD

The PM simulates the basic processes through which Pabst Field was formed. At the beginning, gas migrated from source rocks or other sources along fault F01. As it met the 10,300' sand, it immediately flowed into the sand. The gas flow from fault F01 was

divided into two migration paths, one to the north-northeast, and the other to the south-southwest. On the north side of fault F01, the gas moved northward along two structural ridges and was stopped by fault F04 (Figure 56), resulting in gas accumulation in local structural highs. On the south side of fault F01, gas first accumulated in the western portion of the graben bounded by faults F01 and F02, then moved directly to the horst block on the south side of fault F02, where it gathered mainly in the compartments where production wells A2 and A9 are located. After 13.6 ky, the pressure of gas accumulated on the south of fault F04 exceeded the displacement pressure of fault F04; the fault became a conduit (Figure 57) and gas entered the northern compartments where it was trapped as it met sealing faults such as faults F08 and F03 (e.g. 10,300' sand in Figure 47).

Vertical migration of gas from underlying sand to overlaying sand through the faults , which tends to be very rapid. While gas entered the 10,300' sand, the gas flowed upward along fault F01 into the 10,150' sand and moved northward until it was blocked by fault F04 (e. g. the 10,150' sand in Figures 46, 47). As gas met local highs bounded by faults, it accumulated there. After 13.6 ky, pressure of gas in the 10,150' sand that accumulated on the south of fault F04 exceeded displacement pressure of fault F04. Gas then flowed along and across fault F04 into the northern compartments (Figure 58). This occurred at the same time that fault F04 in the 10,300' sand was breached through. After 16.6 ky, gas flowed into the 10,000' sand through a "skylight window," a strata erosion of the 10,150' sand made by the cutting down of the 10,000' sand channel. Almost at the same time, the gas charged the 10,000' sand along fault F04 (Figures 59, 60).

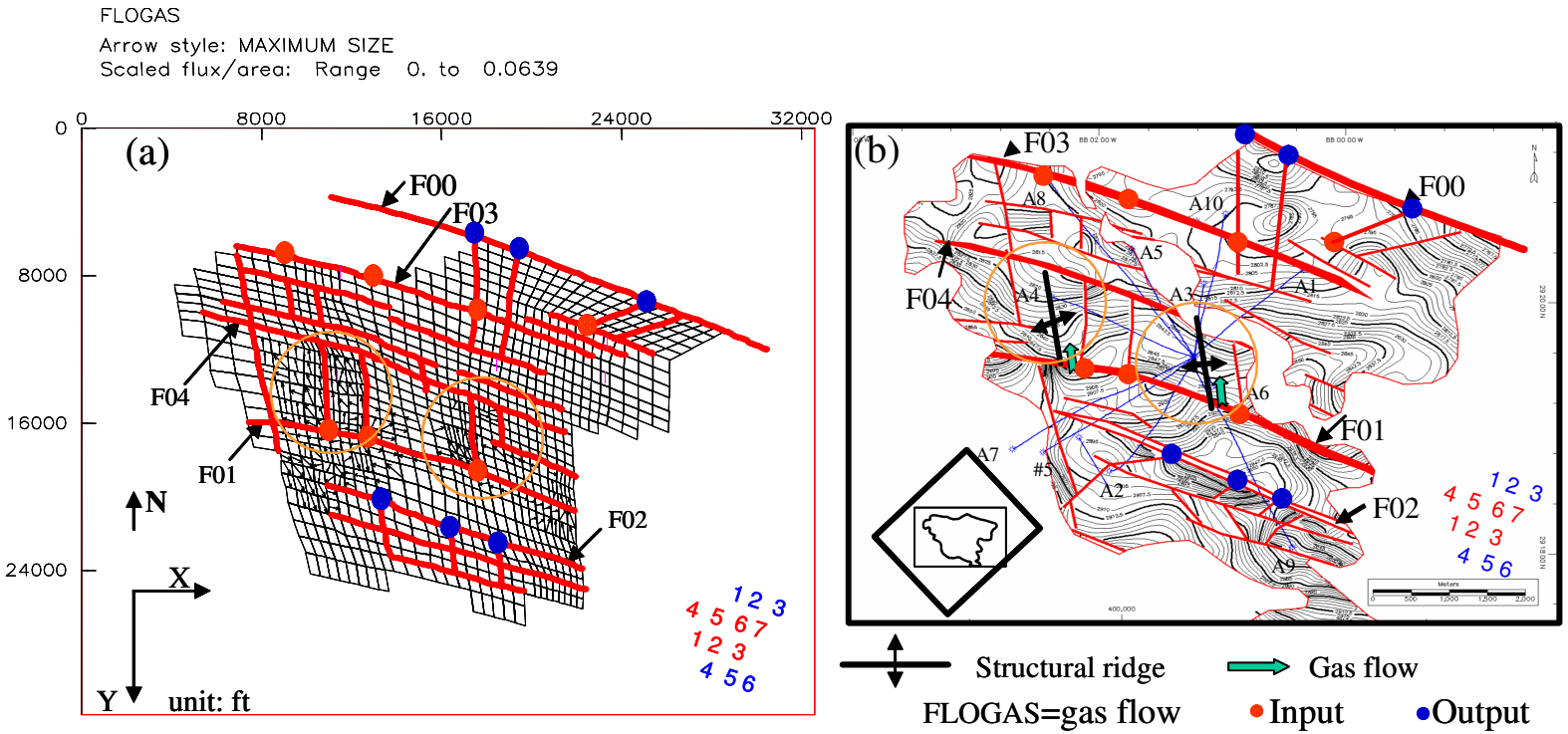

Figure 56. Gas migration in the 10,300' sand at initial charge after 0.2 ky. (a), Gas flow. (b), Time structure map. In (a) gas charges the reservoirs along fault F01. As it moves northward, gas is stopped by fault F04. Comparing (a) and (b), one can find gas migration northward along two structural ridges (see inside of orange circles). Gas flow is illustrated by arrows within cells. The numbers in the lower right corners represent the names of inputs (red) and outputs (blue).

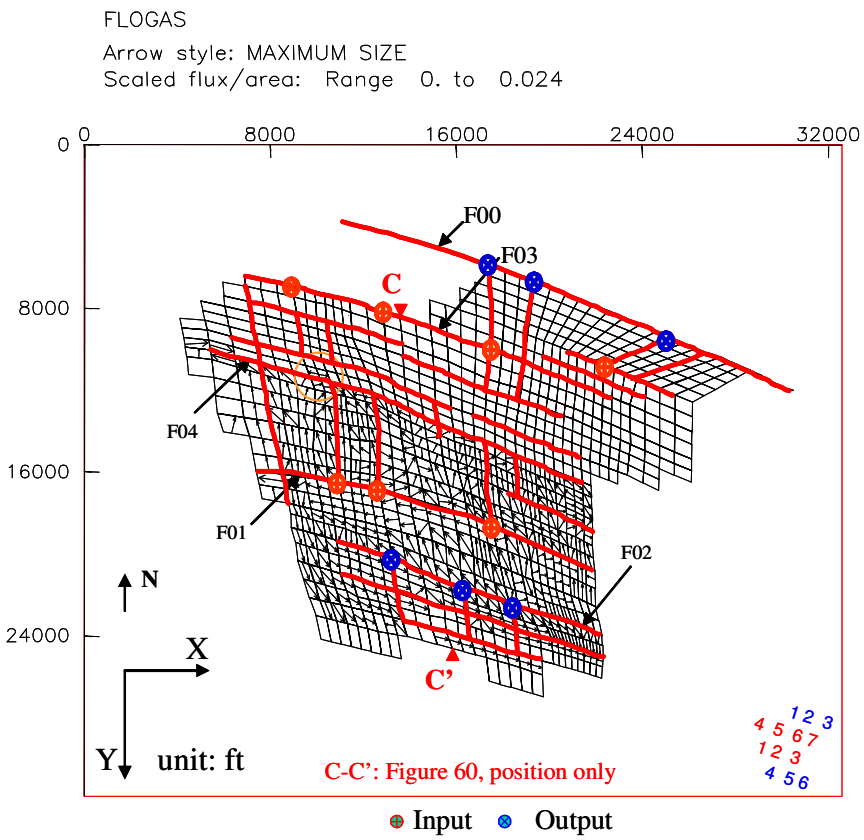

Figure 57. Gas flow in the 10,300' sand after 13.6 ky, showing that fault F04 is breached (see the orange circle). Gas flow is illustrated by arrows. The numbers in the lower right corner are the names of inputs (red) and outputs (blue).

After 20 ky, a new gas source started to charge the three sands along fault F03, which allowed the northern part of the 10,300' sand to be charged. There was also a "skylight window" from the 10,300' sand to the overlying 10,150' sand that allowed gas to escape from the 10,300' sand into the 10,150' sand, instead of migrating northward into 10,300' sand. The 10,150' sand was not influenced by the new gas supply, but for the 10,000' sand, the gas supply was important. After 60 ky, INPT7 started to supply gas. 0.8 ky

later, stable gas supply pathways for the three sands were formed, through which gas accumulated at local structural highs. After 70 ky, all faults shut down and gas supply ended to simulate fault property change. Gas accumulated in most compartments and gas saturation and pressure reached equilibrium for 200 ky (Figure 61).

The process of gas charge indicates that vertical migration of gas along the faults is very fast. The gas can enter any sand it meets. Structural ridges provide the main migration paths for gas flow within the reservoirs. Once the gas meets a sealing fault it

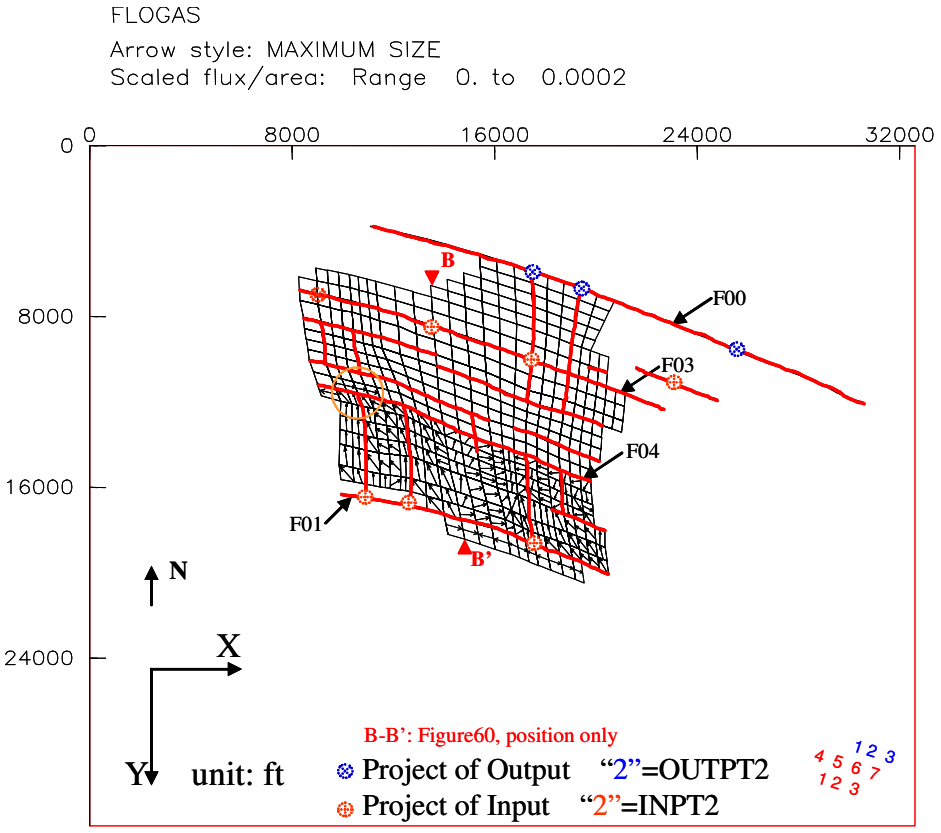

Figure 58. Gas flow in the 10,150' sand after 13.6 ky, showing that fault F04 is breached (see orange circle). Gas flow is illustrated by the arrows within cells. The numbers in the lower right corner are the names of inputs (red) and outputs (blue).

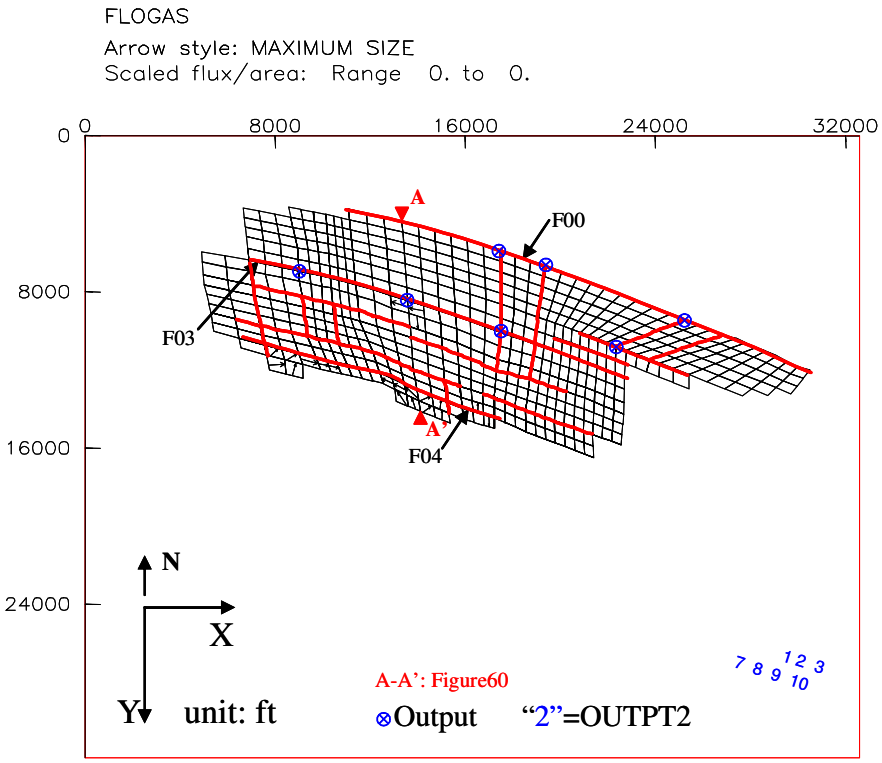

Figure 59. Gas flow in the 10,000' sand after 16.8 ky, showing initial charge of the sand from two faults (F03, F04). Gas flow is illustrated by arrows within cells. The numbers in the lower right corner are the names of outputs (blue).

is trapped. If the fault is breached, the compartments at farther distances have a chance to be charged. If the gas supply is not sufficient, the compartments that are far away from gas supply faults are not charged. The trapping capacity of a fault depends on its petrophysical properties. The existence of the "skylight windows" in the 10,300' sand and the 10,150' sand is an important feature of Pabst Field. Modeling indicates that "skylight windows" facilitate gas accumulation in upper reservoirs instead of lower reservoirs.

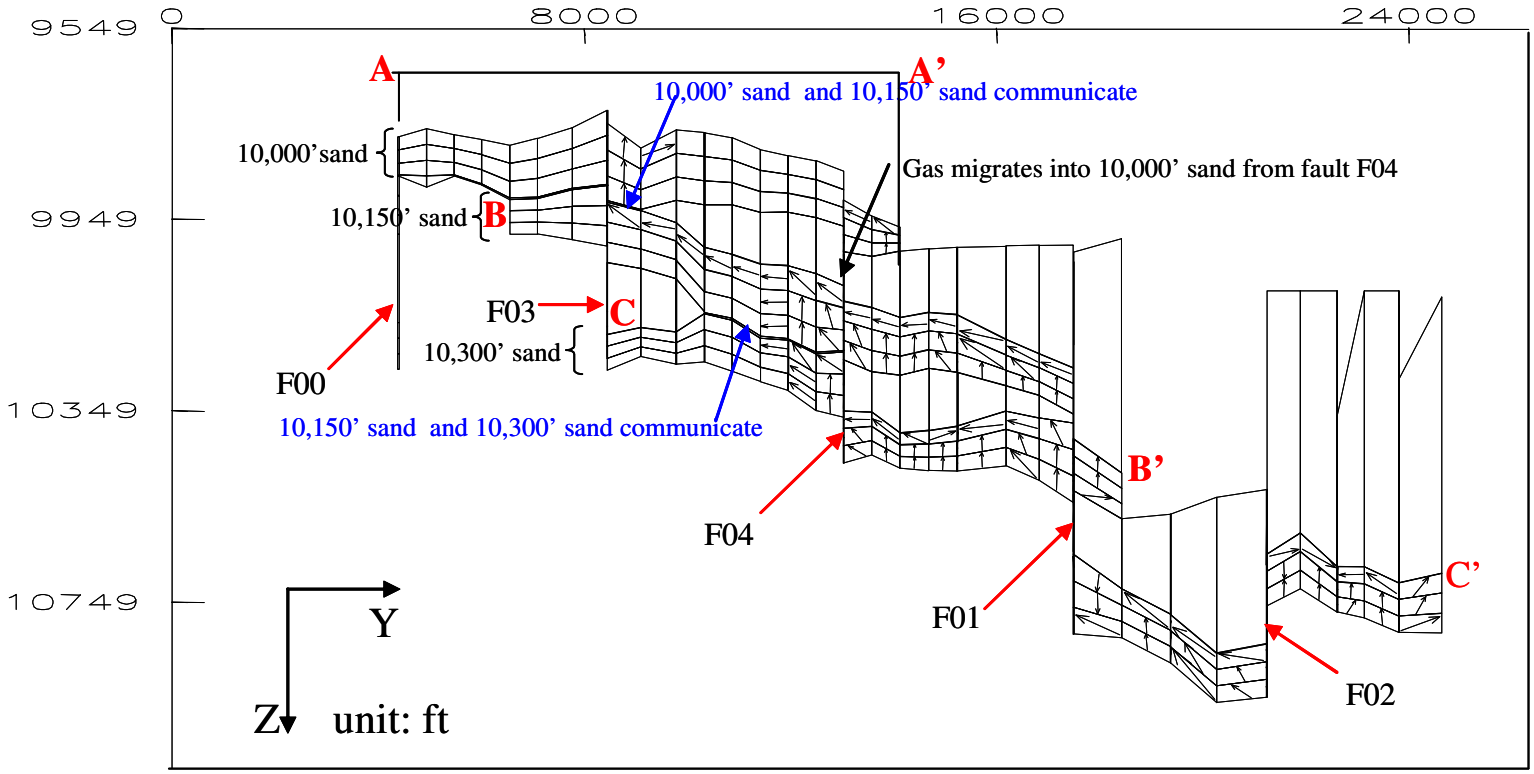

Figure 60. Profile of gas flow along A-A', B-B', and C-C' after 16.8 ky. It shows the initial gas charge of the 10,000' sand from the 10150'sand through "skylight windows" (blue arrows). The "skylight windows" cause 10,000' sand and 10,150' sand and/or 10,150' sand and 10,130' sand to communicate, which allows gas to migrate into 10,000' sand and/or 10,150'sand through "skylight window" of 10,150'/10,300' sand instead of migrating within the10,150'/10,300' sand. Location is in Figures 57, 58, 59. Gas flow is illustrated by arrows within cells.

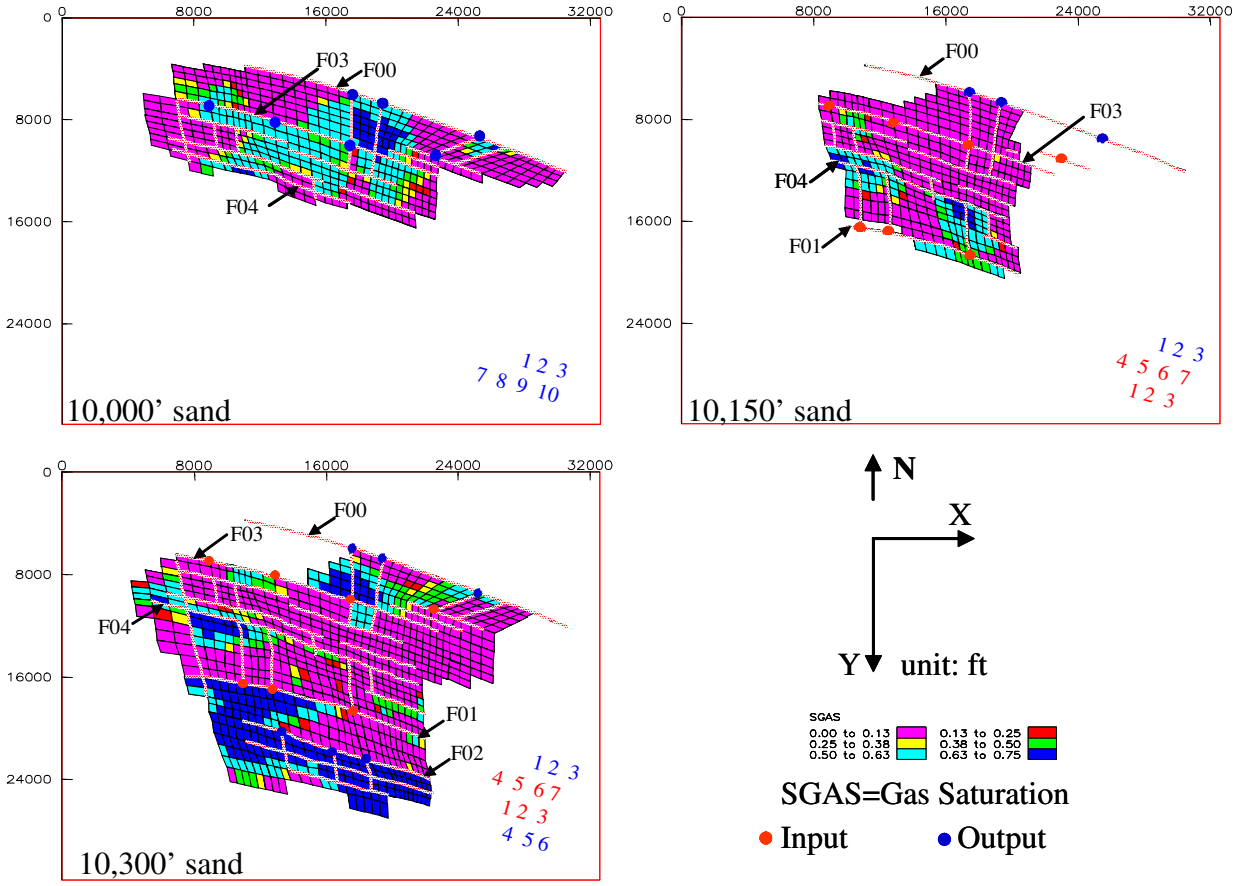

Figure 61. PM gas saturation in three sands after 270 ky. The gas saturation was adjusted by buoyancy and gravity separation and achieved equilibrium 200 ky after all faults were closed. The numbers in the lower right corners represent the names of inputs (red) and outputs (blue).

IMPROVEMENT OF PM

The PM results illustrate the basic process of gas migration and accumulation in Pabst Field. But in the real world the process is probably more complex than the PM. For that reason I constructed an Advanced Model (AM) to add more geological processes to improve gas distribution in the model, such as fault opening/closing, gas charge/stop charge/recharge, and replacement of gas by formation water. In AM, gas was supplied along fault F01 for 20 ky, and the gas supply stopped for 20 ky. Then gas was supplied along F01 again. After that episode, another episode of gas supply was initiated along fault F03 for 40 ky and the gas supply stopped for 40 ky. Then gas was supplied along F03. In a third episode, INPT7 was added to supply gas for 10 ky and then the gas supply stopped for 10 ky. Later on, formation water replaced gas for 22.4 ky. Finally gas supply ended, which allowed the reservoirs to reach equilibrium for 200 ky. The AM increases the time over which the field was formed from 270 ky to 362.4 ky. The gas distribution inferred from the AM is a better match to the seismic gas distribution than that inferred from PM. For example, in the AM, the areas of gas distribution in the graben of 10,300' sand and C#1 of 10,000' sand are much smaller than those in PM, resulting in improvement of gas distribution in PM (Figure 62). The AM indicates that Pabst Field had multiple gas charge processes, which agrees with the conclusion from the study conducted by Sassen et al. (2001).

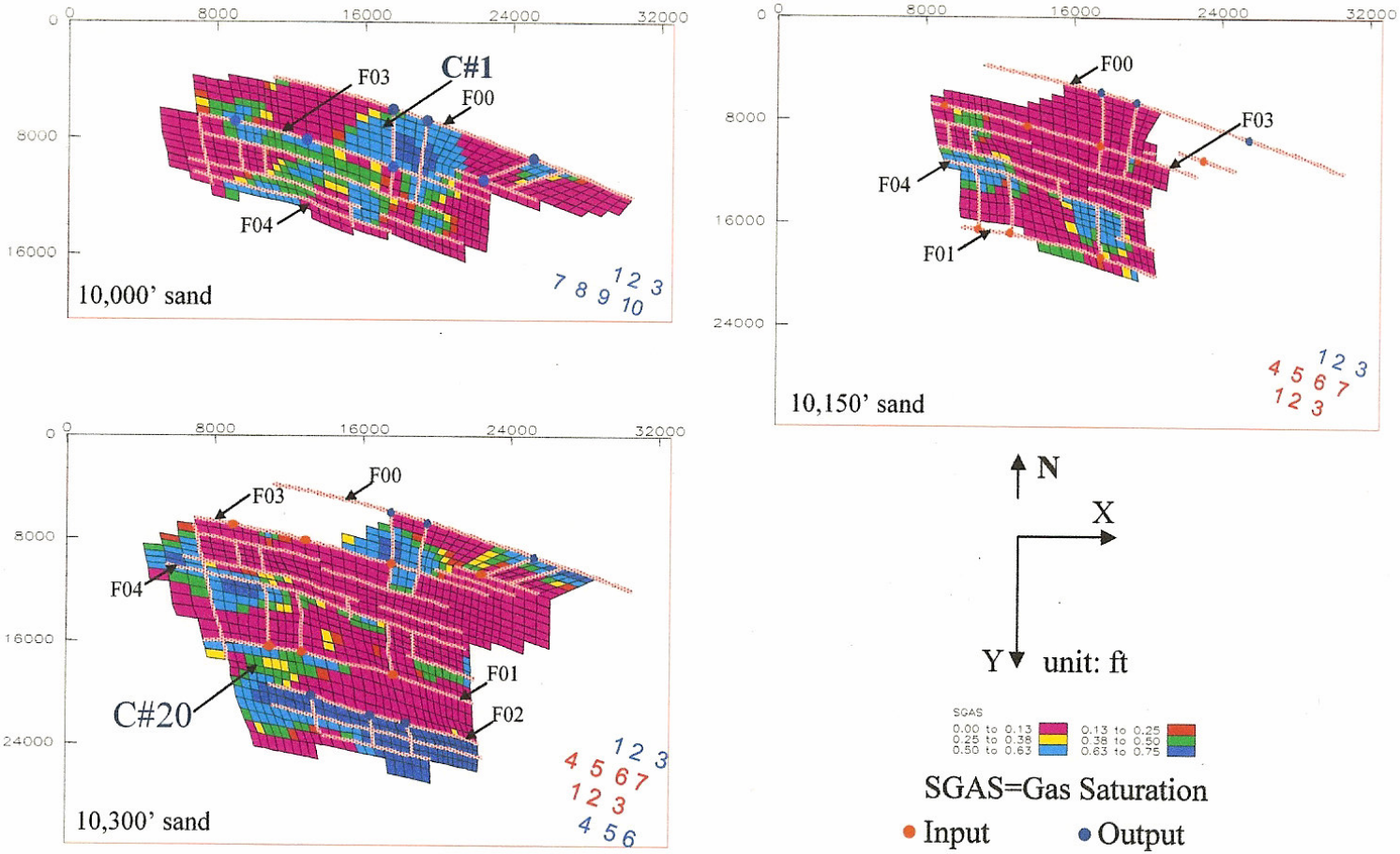

Figure 62. AM gas saturation of three sands, 200 ky after all faults were closed. The gas area in the graben, C#20, of 10,300' sand shrinks. Similar situation occurs in C#1 in 10,000' sand. The result of AM is closer to the field than PM. The numbers in the lower right corners are inputs (red) and outputs (blue).

CHAPTER VI

DISCUSSION AND CONCLUSIONS

A comparison of the results of the field model with the gas distribution in Pabst Field described in chapter V verifies the reasonableness of the modeling. The model represents a plausible geological history and fault properties of Pabst Field. Gas migrated to the field along the large faults and charged the field in multiple-pulse style with short efficient charge time and high charge rate. The field underwent a process that includes faults opening and closing (permeability change), gas charge and escape. In this chapter, I discuss the main controls of the factors on gas migration and accumulation that includes gas supply pattern, charge rate and time, fault properties change, and effect of faults on the gas column by means of the Low Rate Model (LRM), the More Well Model (MWM), and the Gas Column Model (GCM) (Table 8). Finally, I present conclusions and suggest further avenues of study.

Table 8. Discussion models and their roles.

Model name	Code	Test
Low rate model	LRM	Effect of gas charge rate on gas distribution in the field
More well model	MWM	Modify well location in PM to improve gas distribution in the northern part of 10,150' and 10,300' sands
Gas column model	GCM	Effect of fault on Gas column height

GAS CHARGE TIME AND FIELD EVOLUTION

The net charge time of Pabst Field deduced from PM is 70 ky. The total charge time of the field is 270 ky in the PM. If gas charge, escape, and recharge occur repeatedly, the total charge time of the field will be much longer. For example, the forming time indicated by AM is 362.4 ky, less than a half-million years. This time seems too short to be reasonable. In fact, the total charge time is constrained by the geological evolution of the field. According to Sassen (2000) and Sassen et al. (2001), Pabst Field is so young that it is probably still being formed, which agrees with the short forming time shown by the field modeling. Thus, it is reasonable that this modeling does not deal with issues that are related to the geological evolution of the field, such as the variation of reservoir depth with time and corresponding variations of porosity, permeability, geothermal gradient, and gas properties with time.

The charge time is associated with charge differential pressure *dP* from Test Model 4 (TM4), which indicates that *dP* greatly affects the gas saturation S_g. In other words, the variation of *dP* may result in different migration pathways, or different gas distribution in the field model. This is indicated by one of the iterations of PM, here called the Low Rate Model (LRM) in which the average gas charge rate is 16.3 MCFPD, while the charge rate in PM is 33 MCFPD. The gas charge rate is 14.3 MCFPD along fault F01 and 4.5 MCFPD along fault F03 (Figure 63). The result of the LRM indicates that there is no significant difference in gas distribution in the 10,300' sand and the 10,150' sand between PM and LRM. But for 10,000' sand, the gas charge process and gas distribution for the two models are noticeably different. In LRM, after 120 ky, C#5 has

been fully charged, and C#14 has not been charged at all. Whereas, in PM, after 60 ky (corresponding to 120 ky of LRM), C#5 has only been partially charged, and C#14 has been initially charged (Figure 64). After 140 ky, in LRM, C#5 of 10,000' sand has been overcharged, and C#14 is highly charged. Whereas, in PM, after 70 ky (corresponding to 140 ky of LRM), C#5 has been partially charged, and C#14 has been fully charged, which is close to the state of charge in the real field (Figure 65). This test indicates that Pabst Field has a high gas supply rate. In other words, gas with overpressure charges the field, and the net charge time is short, about 70 ky.

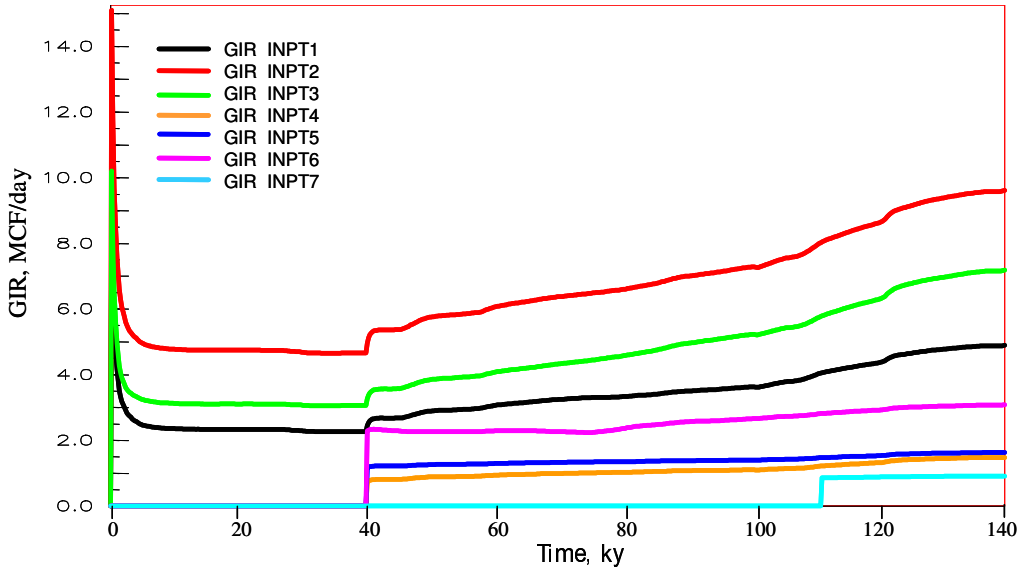

Figure 63. Gas charge rate vs. time, LRM. INPT1, 2, 3 inject gas first. After 40 ky, INPT4, 5, 6 start to inject gas. After 110 ky, INPT7 start to inject gas. INPT1-7 represents inputs, "GIR"=gas input rate. The charge rate of LRM is about half that of PM and its charge time is twice that of PM.

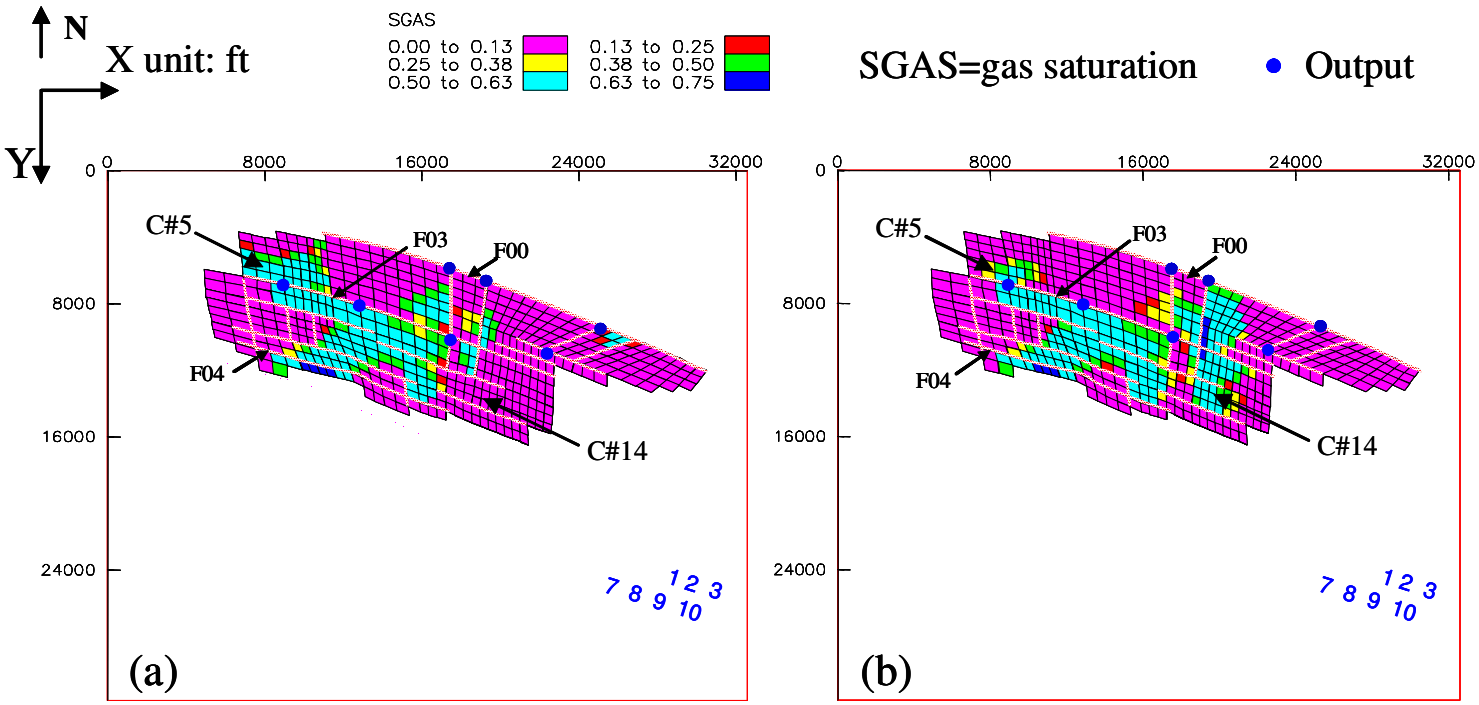

Figure 64. Comparison of gas saturation of the 10,000' sand of LRM after 120 ky with PM after 60 ky. (a), LRM: C#5 is fully charged and C#14 is not charged yet. (b), PM, equivalent to 120 ky of LRM. C#5 is properly charged and C#14 is fully charged. The blue numbers in the lower right corners represent the names of outputs.

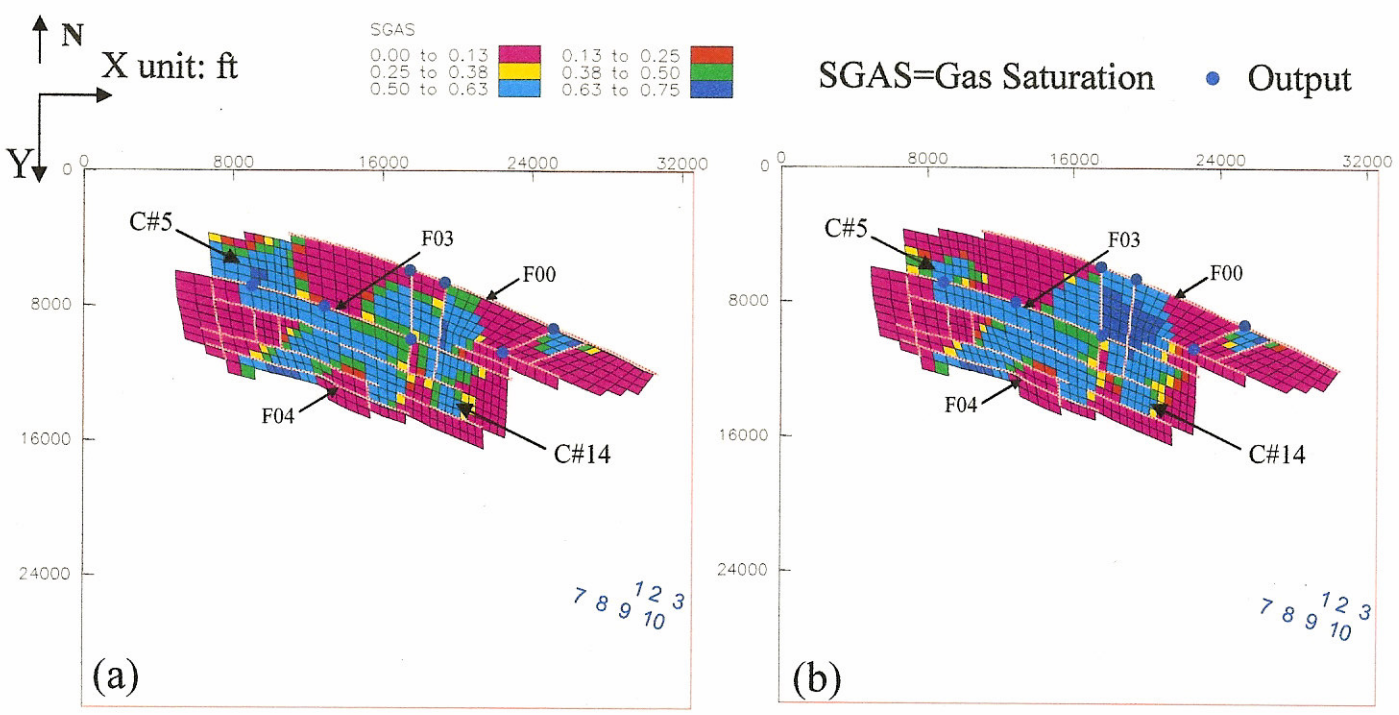

Figure 65. Comparison of gas saturation of the 10,000' sand of LRM after 140 ky with PM after 70 ky. (a), LRM: C#5 is overcharged and C#14 is under charged. (b), PM, equivalent to 140 ky of LRM. C#5 is properly charged and C#14 is fully charged. The blue numbers in the lower right corners represent the names of outputs.

POINT PATTERN OF GAS SUPPLY

The "point pattern of gas supply" is used in the model to simplify the model and to save time of computer runs. In other hand, it is reasonable to construct the gas supply pattern in this way. Studies of Enda Field and Pabst Field in the Gulf of Mexico basin indicate that most hydrocarbons accumulate in traps that are closely associated with the intersection between two fault families (Watkins et al., 1999a). Therefore, most wells (Inputs and Outputs) in the model are set up at the intersections of fault family 1 and fault family 2 to provide a more efficient gas supply to the reservoirs. It is obvious that the well location and number will affect greatly the gas migration and gas distribution. Because I used as few inputs and outputs as possible to save computer run time, it is probable that there are compartments that are not charged with gas owing to point gas supply pattern. For example, the point gas supply pattern along fault F03 may cause some compartments in the northern portion of the reservoir to be deprived of gas, such as C # 9 in the 10,300' sand. Therefore, I built a More Wells Model (MWM) to improve the PM by adding an input at the intersection between fault F07 and fault F20 to provide more gas supply along the faults. As a result, C#7 and C#9 are charged with gas (Figure 66). In the adjacent area of C#7 and C#9, the faults of the two fault families cut each other to allow a large amount of gas to supply the reservoirs, which need more Inputs and Outputs in the model. If some inputs and/or outputs are added in the area, C#7 and other compartments are charged with much more gas. But in the model it was difficult to add more inputs and/or outputs owing to limited time of computer run.

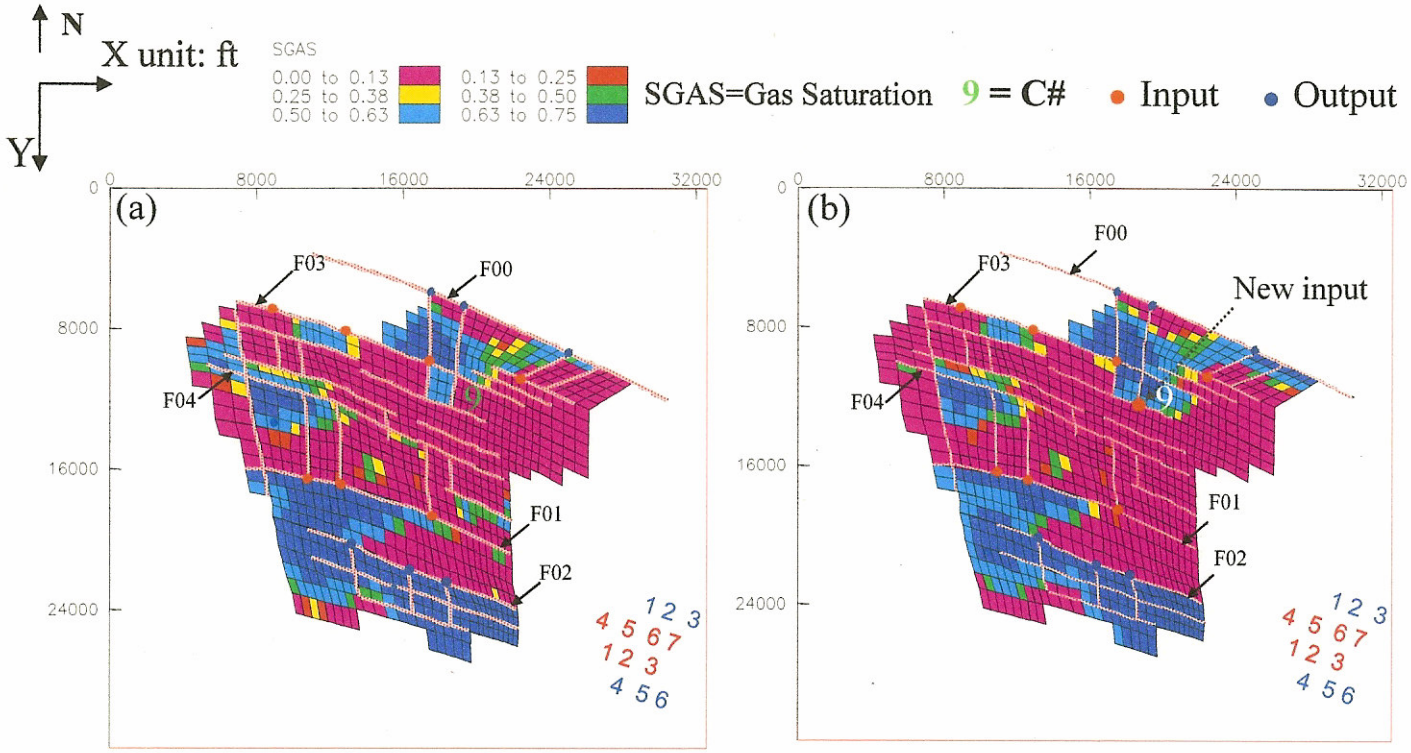

Figure 66. Comparison of gas saturation of the 10,300' sand of PM with MWM after 40 ky. (a), PM: no gas in C# 9. (b), MWM: gas charged C#9 as a new input is added. The numbers in the lower right corners are inputs (red) and outputs (blue).

THE EFFECT OF FAULTS ON GAS CHARGE

The capillary displacement pressure of a fault determines the sealing capacity (Berg and Avery, 1995), which represents the maximum gas column that a fault can hold before it leaks. The greater the displacement capillary pressure is, the higher the gas column. As gas flows and meets a fault, the gas will be baffled by the fault because of a difference in capillary pressure between reservoir and fault (refer to Figure 31). But the formation water still flows through the fault to enter the next reservoir. Once the gas flow pressure exceeds the fault's capillary displacement pressure, the fault is breached, and gas will go through the fault and enter the next reservoir. If the fluid is in a dynamic state (opposite of equilibrium state), the gas contained in the fault will improve the sealing capacity of the fault, because the gas column always keeps its static height, the difference between the gas column of the reservoir and that of the fault. Smith (1966) pointed out that if the differential pressure is high, the fault will be easily broken but will contain more gas and have higher gas saturation; this results in a high gas column in the sealed reservoir.

To analyze dynamic process of gas flow through a fault, I constructed a model with a tilted reservoir, referred to here as Gas Column Model (GCM). In Figure 67, the GCM shows that the dynamic process of the gas column is controlled by the fault properties and fluid pressures in both the reservoir and the fault. This process can not be observed clearly in PM because the grid of the PM is too large. The fluid break through across the fault occurs in the following manner: gas flows through the upper portion of the fault rather than the whole fault. A constant gas column is maintained and is

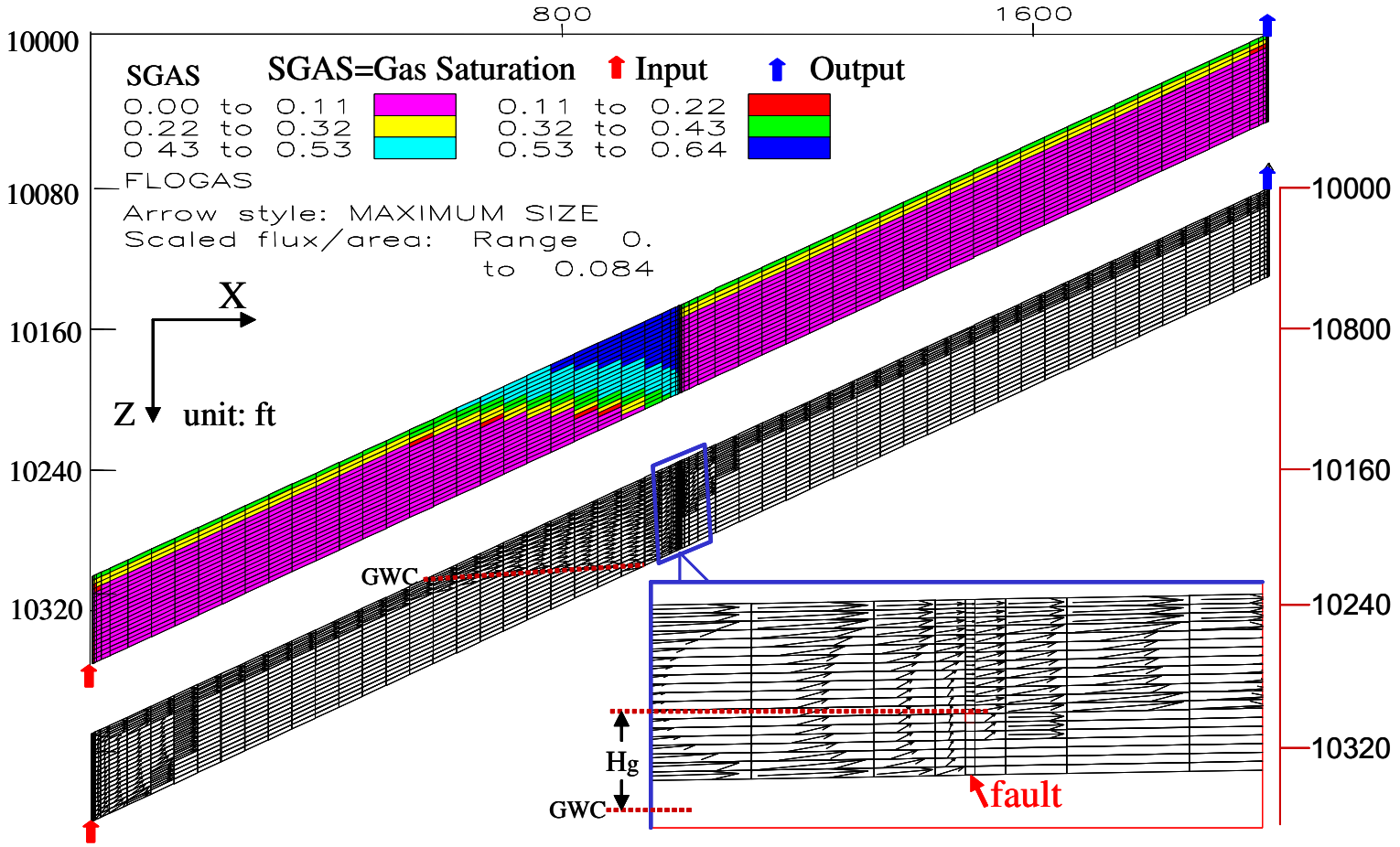

Figure 67. S_g and gas flow profiles of GCM. t=200 years, dP= 30 psia. In inset, only upper portion of the fault is breached. H_g is measured from the bottom of the gas column in the fault to the bottom of the gas column in the sealed reservoir. GWC=Gas Water Contact.

measured from the bottom of the gas column in the sealing fault to the bottom of the gas column in the sealed reservoir. As the right reservoir in the model contains gas, the gas in the fault is prevented from escaping laterally, resulting in a dynamic gas column that is larger than static gas column. This result is in coincidence with what was concluded by Smith (1966) instead of Watts (1987).

Once the capillary pressure of the sealing fault increases due to change of fault properties, the high gas column height will be maintained at a constant value. Modeling indicates that maintenance of this large gas column requires fault permeability to change from 0.1 md to 0.001 md. If the fault permeability was initially set at 0.001 md, gas did not flow across the faults or along the faults, hence the modeling gas distribution did not match the seismic gas distribution. Thus, I simulated the fault permeability change from 0.1md during gas charging of the reservoirs to 0.001md in PM and AMs during no gas charging. In other words, the current fault permeability is very low (0.001 md) but the fault permeability was high (0.1md) during gas charging into the reservoirs. Caine et al. (1996) observed that the core zone of Dixie valley fault zone acted as a short-lived fluid flow conduit during syn-deformation and then sealed to form a barrier to flow. They observed the same processes in other faults. If it is true, the faults tend to be leaky or sealed depending on the tectonic history.

Juxtaposition also affects fault fluid flow behavior. During growth of faults, leaking or sealing occurs when there is juxtaposition of the faults with highly permeable zones or low permeability zones, respectively. The change of fault fluid flow behavior from

conduits to barriers or from barriers to conduits should be common in the geological history of Pabst Field.

PREDICTION OF GAS POTENTIAL FOR UNDRILLED COMPARTMENTS

An advantage of this modeling is the prediction of hydrocarbon potential in undrilled compartments, which will help further exploration and development. For example, C#20 (the graben) of the 10,300' sand, C#16 of the 10,150' sand, and C#4 of the10,000' sand are characterized by middle-high to high amplitude anomalies. Modeling indicates that these compartments contain gas with saturation higher than 40%. C#4 of the 10,000' sand has an especially strong seismic amplitude anomaly. Stratigraphy is a critical factor in gas charging. Pinch-outs was interpreted to separate the 10,000' sand into fan 1 and fan 2 (Figures 52 (a), 55), in order for C#4 of the 10,000' sand to be charged with gas in PM.

CONCLUSIONS

1. The main reservoirs of Pabst Field consist of three sands that are interpreted as a slope fan deposited within the low-stand tract in the late Middle Miocene. Change of sea level and sediment supply cause the sands from old to young to shift landward against a growth fault. Overlying younger sands cut down into older sands due to slope erosion, forming partial communications for fluid flows among the three sands.

2. Three fault families structurally partition the three sands into numerous compartments. Most Low Throw near Vertical Faults (LTNVFs) do not have sufficient

throw to totally offset the sand bodies across the faults. Communication between compartments is controlled by fluid pressure, fault properties, and fault evolution. Stratigraphy, structure, and pressure determine gas migration paths in the field at the reservoir scale.

3. A primary fault and large synthetic and antithetic faults act as migration pathways. They have different roles due to variations in their properties. The synthetic and antithetic faults act as gas inlets, and the primary fault is an outlet for gas flow. LTNVFs act as barriers to lateral gas flow. The spatial variation of fault properties changes the vertical pressure gradient along faults even though overpressure in gas supply is uniform, resulting in a build-up of differential pressure laterally between two ends of sands bounded by the faults. This differential pressure is an important driving force that moves gas through reservoirs and across faults.

4. Capillary pressure of the faults affects gas columns. A constant gas column is determined by displacement capillary pressure of a sealing fault. The column is measured from the bottom of the gas column in the sealing fault to the bottom of the gas column in the sealed reservoir. As the up-dip reservoir is charged with gas, the gas will prevent gas from escaping off the fault laterally, resulting in a larger gas column in the down-dip reservoir. If permeability of the fault reduces or the fault capillary pressure increases, the larger gas column will be maintained.

5. The fault properties control gas saturation profiles. The best match of the model with seismic gas distribution requires the porosity and permeability of faults in Pabst Field to be 10 % and 0.1 md, respectively, during gas charging of the sand reservoirs.

But during no gas charging and maintenance of large gas columns, the porosity and permeability of the faults decrease to 6% and 0,001 md, respectively.

6. This modeling indicates Pabst Field has a short, impulsive gas charge history. Some geological processes, such as fault opening/closing, gas charge, gas charge stop, gas recharge, and replacement of gas by formation water, may have occurred. The effective charge time is 0.07 Ma, which reflects the fact that the gas charge rate is high.

7. The gas distribution in Pabst Field simulated by Eclipse® 100 is in accordance with that obtained from seismic amplitude anomalies and well log data and well testing data. This indicates that the Eclipse® simulator is capable of simulating gas migration and accumulation in a faulted reservoir at the reservoir scale, even though some simplification is assumed.

8. This simulation provides not only the dynamic process of gas flow in and through faulted sand reservoirs but also predictions of gas in undrilled compartments.

FURTHER STUDIES

1. The precision of this modeling is limited by grid model. If a new version of software were used, the cell number might not increase but cells adjacent to faults might be smaller. Also, the fault shape and size could be defined flexibly and in more detail.

2. It is true that the reservoirs and fault zone are heterogeneous. The variation of reservoirs and fault properties, particularly permeability, will affect migration pathways. Thus, the study of heterogeneity of reservoirs and faults, including thickness, porosity, and permeability will help to build more realistic models.

3. “Point gas supply pattern” is simple and timesaving for a computer run. However, it fails to charge some compartments that are far away from gas supply faults. Further studies may consider simulation of gas supply along entire faults.

The role played by faults in hydrocarbon migration has been receiving increased attention. With the development of 3-D seismic interpretation techniques, more and more faults will be found in reservoirs; this presents challenges to further exploration and production simulation. This study meets the demand of exploration and production, especially in cases where core and well log data are not insufficient. The primary study demonstrates that the field modeling is reasonable in results and workable in technique, so that it should be a useful tool for modification of fault interpretation and hydrocarbon prediction in faulted reservoirs. Utilizing present commercial software gives this approach universal significance.

REFERENCES CITED

Ahmed, U., S. F. Crary, and G. R. Coates, 1989, Permeability estimation: the various sources and their interrelationship: SPE Paper 19604, p. 649-662.

Allen, P. A. and J. R. Allen, 1990, Basin analysis: principles and applications: Boston, Blackwell Science Publications, 451p.

Antonellini, M. and A. Aydin, 1994, Effect of faulting on fluid flow in porous sandstones: petrophysical properties: AAPG Bulletin, v. 78, p. 355-377.

Bahorich, M. and S. Farmer, 1995, 3-D seismic discontinuity for faults and stratigraphic features: the coherence cube: The Leading Edge, v.14, p. 1053-1058.

Bai, J., 2003, Preliminary investigation of the nature of hydrocarbon migration and entrapment in fault structures: Ph.D. dissertation, Texas A&M University, 114p.

Berg, R. R., 1975, Capillary pressure in stratigraphic traps: AAPG Bulletin, v. 59, p. 939-956.

Berg R. R. and A. H. Avery, 1995, Sealing properties of tertiary growth faults, Texas Gulf Coast: AAPG Bulletin, v. 79, p. 375-393.

Berg, R. R. and A. F. Gangi, 1999, Primary migration by oil-generation microfracturing in low-permeability source rocks: application to the Austin chalk, Texas: AAPG Bulletin, v. 83, p. 727-756.

Bradshaw, B. E. and J. S. Watkins, 1996, Growth faults and growth-fault mechanisms observed in the Gulf of Mexico: AAPG Abstract, v. 80, p. 1496.

Brooks, R. H. and A. T. Corey, 1966, Properties of porous media affecting fluid flow: Irrigation and Drainage Division, v. 92, p. 61-88.

Caine J. S., J. P. Evans and C. B. Forster, 1996, Fault zone architecture and permeability structure: Geology, v. 24, p. 1025-1028.

England, W. A., A. S. Mackenzie, D. M. Mann and T. M. Quigley, 1987, The movement of entrapment of petroleum in the subsurface: Journal of the Geological Society (London), v. 144, p. 327-347.

England, W. A. and C. Townsend, 1998, The effects of faulting on production from a shallow marine reservoir - a study of the relative importance of fault parameters: SPE Paper 49023, p. 279-294.

Fisher, Q. J. and R. J. Knipe, 1998, Fault process in silisiclastic sediment *in* G. Jones, Q. J. Fisher and R. J. Knipe, eds., Faulting, fault sealing and fluid flow in hydrocarbon reservoirs: The Geological Society of London, p. 117-134.

Fingleton, W. G. and E. Zinni, 1999, 3-D impact on exploration success, main pass south and east area, Gulf of Mexico: The Leading Edge, Feb., p. 200-205.

Galloway, W. E., 1989, Genetic stratigraphic sequences in basin analysis II: application to northern Gulf of Mexico Cenozoic basin: AAPG Bulletin, v. 73, p. 143-154.

Galloway, W. E., P. E. Ganey-Curry, X. Li and R. T. Buffler, 2000, Cenozoic depositional history of the Gulf of Mexico Basin: AAPG Bulletin, v. 84, p. 1743–1774.

Gibson, R. G., 1998, Physical character and fluid-flow properties of sandstone-derived fault zones *in* M. Coward, T. Daltaban and H. Johnson, eds., Structural geology in

reservoir characterization: Geological Society of London Special Publications, 127, The Geological Society of London, p. 83-97.

Hall, H. N., 1953, Compressibility of reservoir rocks: Journal of Petroleum Technology, v. 5, p.17-19.

Harris, S. D., L. Elliott and R. J. Knipe, 1999, The pulsed migration of hydrocarbon across inactive faults: Hydrology and Earth System Sciences, v. 3, p. 151-176.

Hawkins, J. M., D. L. Luffel and T. G. Harris, 1993, Capillary pressure model predicts distance to gas/water, oil/water contact: Oil and Gas Journal, Jan., p. 39-43.

Hicks Jr., P. J., P. B. Flemings, J. P. Ashbaugh and M. H. Bennett, 1998, Numerical modeling of secondary migration in faults: Paper presented at the 1998 AAPG Hedberg Research Conference at Galveston, TX, p. 1-3.

Hindle, A. D., 1997, Petroleum migration pathways and charge concentration: a three-dimension model: AAPG Bulletin, v. 81, p. 1451-1481.

Hintz, J. C., 2001, Trapping capacity of fault zones, downdip Yegua formation, Texas Gulf Coast Basin: M. S. thesis, Texas A&M University, 190p.

Ibanez, W. D., 2000, Characterization of the structure and permeability of shear zones in a siliciclastic aquifer: Ph.D. dissertation, Texas A& M University, 240p.

Johnson, B., W. D. Ibanez, J. W. Wilson and F. M. Chester, 1999, Preliminary results of an integrated study to characterize and correlate the structure and permeability field of a fault in a siliciclastic aquifer *in* Fault and fault seal forum: Houston Geological Society, Houston, Texas, p. 6.

Kim, J., R. R. Berg, J. S. Watkins and T. T. Tieh, 2001, Trapping capacity of faults in the Eocene Yegua formation, East Sour Lake Field, Southeast Texas: AAPG, Bulletin, Abstract, v. 85.

Knai, T. A. and R. J. Knipe, 1998, The impact of fault on fluid flow in the Heidrum Field *in* G. Jones, Q. J. Fisher and R. J. Knipe, eds., Faulting, fault sealing and fluid flow in hydrocarbon reservoirs: The Geological Society of London, p. 269-282.

Knipe, R. J., G. Jones, and Q. J. Fisher, 1998, Faulting, fault sealing and fluid flow in hydrocarbon reservoirs: an introduction *in* G. Jones, Q. J. Fisher and R. J. Knipe, eds., Faulting, fault sealing and fluid flow in hydrocarbon reservoirs: The Geological Society of London, p. vii-xxi.

Kortekaas, T. F. M., 1985, Water/oil displacement characteristics in crossbedded reservoir zones: SPE Paper 12112, p. 917-926.

Kulander, C. S., 1999, Geological evolution and structural controls on hydrocarbon flow in the Ship Shoal Block 274/293 Field, offshore Louisiana, Gulf of Mexico: Ph.D. dissertation, Texas A&M University, 88 p.

Lerche, I., 1990, Basin analysis, quantitative methods, volume I: Academic Press, Inc., San Diego, CA, 562 p.

Matthai, S. K., A. Aydin, D. D. Pollard and S. G. Roberts, 1998, Numerical simulation of departures from radial drawdown in a faulted sandstone reservoir with joints and deformation bands *in* G. Jones, Q. J. Fisher and R. J. Knipe, eds., Faulting, fault

sealing and fluid flow in hydrocarbon reservoirs: The Geological Society of London, p. 157-191.

McCain Jr., W. D., 1973, The properties of petroleum fluids: Tulsa, Petroleum Pub. Co., 325 p.

McCain Jr., W. D., 1991, Reservoir-fluid property correlations - state of the art: SPE Paper 18571, p.266-272.

Mitchum Jr., R. M., J. B. Sangree, P. R. Vail and W. W. Wornardt, 1990, Sequence stratigraphy in late Cenozoic expanded sections, Gulf of Mexico *in* Sequence stratigraphy as an exploration tool: GCSSEPM Foundation Eleven Annual Research Conference Program and Abstract, p. 237-256.

Osborne, M. J. and R. E. Swarbrick, 1997, Mechanisms for generating overpressure in sedimentary basins: a reevaluation: AAPG Bulletin, v. 81, p. 1023-1041.

Ottesen, S. E., R. J. Knipe, T. S. Olsen, Q. J. Fisher and G. Jones, 1998, Fault controlled communication in the Sleipner Vest Field, Norwegian continental shelf; detailed, quantitative input for reservoir simulation and well planning *in* G. Jones, Q. J. Fisher and R. J. Knipe, eds., Faulting, fault sealing and fluid flow in hydrocarbon reservoirs: The Geological Society of London, p. 283-297.

Hawkins, J. M., D. L. Luffel and T. G. Harris, 1993, Capillary pressure model predicts distance to gas/water, oil/water contact: Oil and Gas Journal, Jan., p. 39-43.

Paleo-Date, Inc., 2003, Neogene biostratigraphic – chart Gulf of Mexico, http://www.paleodata.com.

Pittman, E. D., 1992, Relationship of porosity and permeability to various parameters derived from mercury injection – capillary pressure curves for sandstone: AAPG Bulletin, v. 76, p. 191-198.

Rowan, M. G., M. P. A. Jackson and B. D. Trudgill, 1999, Salt-related fault families and fault welds in the Northern Gulf of Mexico: AAPG Bulletin, v. 83, p. 1454-1484.

Sassen, R., 2000, Preliminary geochemical insight into Pabst oils and gases: IRIG Abstract, Personal Collection, Department of Geology and Geophysics, Texas A&M University.

Sassen, R., J. S. Watkins, C. L. Decker, S. T. Sweet, D. A. DeFreitas and S. Losh, 2001, High maturity gas in the Main Pass Area: comparison to the central Gulf of Mexico slope: Gulf Coast Association of Geological Societies Transactions, v. 51, p. 285-291.

Schowalter, T. T., 1979, Mechanics of secondary hydrocarbon migration and entrapment: AAPG Bulletin, v. 63, p. 723-760.

Schlumberger, 1998, Eclipse® manual: Houston, Texas.

Smith, D. A., 1966, Theoretical considerations of sealing and non-sealing faults: AAPG Bulletin, v. 50, p. 363-374.

Standing, M. B., 1978, Notes on relative permeability relationships: Course notes, University of Trondheim, Norway.

Sunwoo, D., 1999, Salt tectonics and seismic stratigraphy of the offshore Mississippi delta region, Gulf of Mexico: Ph.D. dissertation, Texas A&M University, 140p.

Thomeer, J. H. M., 1960, Introduction of a pore geometrical factor defined by the capillary pressure curve: Journal of Petroleum Technology, v. 12, p. 73-77.

Thomeer, J. H. M., 1983, Air permeability as a function of three pore-network parameters: Journal of Petroleum Technology, v.35, p. 809-814.

Watkins, J. S., R. R. Berg, J. Hintz, R. Sassen, R. Gan et al., 2000, Annual report: personal collection, Department of Geology and Geophysics, Texas A&M University.

Watkins, J. S., C. L. Decker, J. Bai, Y. Li, J. Kim et al., 1999a, Annual report: personal collection, Department of Geology and Geophysics, Texas A&M University.

Watkins, J. S., C. L. Decker, R. Sassen, T. A. Blasingame, Y. Li, J. Bai and R. Gan, 2001a, Low-throw near-vertical faults (LTNVF): their role in migration, entrapment and production: AAPG Bulletin, v. 85, AAPG Annual Meeting Abstract.

Watkins, J. S., C. Kulander, W. Lee, T. A. Blasingame, C. L. Decker and R. R. Berg, 1999b, Comparison of estimated fault-bound compartment area with calculated drainage area: a tool for predicting sealing capacity of faults: AAPG Bulletin, v. 83, AAPG Annual Meeting Abstract.

Watkins, J. S., Y. Li, R. Sassen, C. L. Decker, M. Fiorito et al., 2001b, Annual report: personal collection, Department of Geology and Geophysics, Texas A&M University.

Watts, N. L., 1987, Theoretical aspects of cap-rock and fault seal for single and two-phase hydrocarbon column: Marine and Petroleum Geology, v. 4, p. 274-307.

Yielding, G., J. J. Walsh and J. Watterson, 1992, The prediction of small-scale faulting in reservoirs: First Break, v. 10, p. 449-460.

VITA

NAME: Yuqian Li

ADDRESS: 9110 Memorial Trail Dr. Spring, TX 77379

EDUCATION: B.S. (Geology), Nanjing University, Feb. 1982

Ph.D. (Geophysics), Texas A&M University, May 2006

EXPERIENCE: Exploration Geologist – China National Offshore Oil Corporation, 1982-1998

Research Assistant – Department of Geology & Geophysics, Texas A&M University, Jan. 1999-Aug. 2001

Teaching Assistant – Department of Geology & Geophysics, Texas A&M University, Sept. 2001-May 2003